Sverre Skalleberg Gjerde

Analysis and Control of a Modular Series Connected Converter for a Transformerless Offshore Wind Turbine

Thesis for the degree of Philosophiae Doctor

Trondheim, October 2013

Norwegian University of Science and Technology
Faculty of Information Technology,
Mathematics and Electrical Engineering
Department of Electric Power Engineering

NTNU – Trondheim
Norwegian University of
Science and Technology

NTNU
Norwegian University of Science and Technology

Thesis for the degree of Philosophiae Doctor

Faculty of Information Technology, Mathematics and Electrical Engineering
Department of Electric Power Engineering

ISBN 978-82-471-4688-0 (printed ver.)
ISBN 978-82-471-4689-7 (electronic ver.)
ISSN 1503-8181

Doctoral theses at NTNU, 2013:279

Printed by NTNU-trykk

Acknowledgements

This thesis summarizes the work towards my PhD, which has been conducted at the Department of Electric Power Engineering, Norwegian University of Science and Technology (NTNU), from fall 2009 to summer 2013. The financial support for the work was given by the Research Council of Norway, and the project has been defined as part of the Norwegian Research Centre for Offshore Wind Technology (NOWITECH). During the four years, many people have assisted, supported and helped me in different ways. There are too many to mention here, but I will try to address the most central people.

I would first like to thank my two supervisors, Professor Tore M. Undeland, and Dr. Roy Nilsen. You have been of great importance. Tore with overview, insight, ideas and encouragement. That you also showed me trust, and let me figure out my own direction has been important for both my development and motivation. Roy, with in-depth discussions, ideas and detailed knowledge which has been very important for the theory developed in the thesis. I could not have asked for better supervisors.

The next on the list is Kjell Ljøkelsøy from SINTEF, who has taught me almost everything I know about FPGA and laboratory work. I hope that, in the end, I was also able to give something back.

The cooperation with Pål Keim Olsen (SmartMotor/NTNU) has been of great importance for my thesis. His enthusiasm for the project and knowledge on machine design and insulation is largely appreciated.

I have also received considerable support from SmartMotor, and especially my contacts Alexey, Sigurd and Rune. Not only did they let me borrow, and reconfigure the prototype of the ironless generator, which made it possible to achieve good, relevant experimental data. But they also contributed with valuable discussions, insight and optimism. Also, my colleagues Zhang and Robert, and Sverre and Jorun at SINTEF have contributed in this group.

The help from the service lab (Bård, Vladimir and Svein) and the workshop (Dominc, Erland and Oddvar) at the Department of Electric Power Engineering is greatly appreciated. Thank you for all your creativity, knowledge and positive attitude. There were several times I was sure that I had hit the wall when it came to constructing the laboratory prototype, but you always came up with a solution. The staff in the administration, Åshild, Inger, Halstein and of course Eva has been of great help. I also acknowledge Stewart Clark at NTNU for editing the thesis.

I will also thank all my fellow PhD students, in the (extended) energy conversion group, and NOWITECH. (I thank Fritz and Til Kristian for mutual help with proof reading). I have enjoyed this time with you, both at work and socially.

Finally, I would like to thank my family for their support, and Atsede, for her support, help with the final proof reading, and patience, which has been beyond limits during the last few months.

Trondheim, Summer 2013
Sverre

Abstract

A modular series connected converter consisting of N number of converter units, suitable for a high power, high voltage transformerless offshore wind turbine is analyzed in this thesis. The main objective is to verify the feasibility of the proposed converter system as a suitable interface between a modular axial flux ironless stator permanent magnet synchronous generator and a high voltage DC link.

The physical properties of the modular generator and the series connected converter are analyzed. A relation between variations in physical parameters of the generator/converter modules and deviating DC-bus voltages in the modules is identified, and described analytically. The series connection requires balanced voltages between the DC-buses of the modules in order to achieve the best total operation of the converter units, and stress them equally. Additionally, the high voltage insulation of the generator requires balanced module voltages for optimal insulation design. As a consequence, a DC-bus voltage control is introduced to mitigate the identified DC-bus voltage deviations. This control may result in a need to derate the turbine due to increased current loading of some modules. The derating depends on the combination of control strategy and module-parameter variations. The need for a DC-bus voltage controller is further supported by the small-signal-stability analysis of the modular converter system operated in current-control mode. This analysis demonstrates that the internal voltage distribution of the DC buses is only stable in the generator mode, and instable in the motor mode.

Based on the theoretical analysis, the synthesis of a modular control system is presented. The synthesis is built on a generator mathematical model which decouples the control of each stator segment and converter unit from the other modules. Hence, a 3-phase vector current control can be applied to each converter unit control. Given the need for compensating different bus voltages, a DC-bus voltage PI controller is added in each module. It is demonstrated that the control system can be designed to be sufficiently robust to function satisfactorily in all operating conditions.

The DC-bus voltage control reference is generated in the main turbine control unit. A torque-based DC-voltage droop is proposed to remove steady-state net turbine torque contributions from the DC-bus voltage balance control in normal operation. The cause of this problem is an overdetermined DC-voltage control system, with one degree of freedom less that the number of PI controllers. Frequency response analysis of the droop control is presented for the selection of control parameters. The inclusion of the droop is necessary to provide a fully modular control system.

The main turbine control also provides turbine power control, and its interface to the module controllers is the torque reference and DC-bus voltage reference.

The system fault tolerance with respect to converter unit failures is analyzed. Two scenarios are identified that are of special interest for the modular, series connected converter: The first is the response to a converter unit trip. For safe-operation of the converter chain, a redundant $(N-1)$ component voltage rating is required due to the overvoltages in the functioning modules caused by the converter trip. It is demonstrated that continued operation is possible, either by reconnecting the tripped module (in case of false trip) or bypassing the module. In the latter case, the modular converter continues operating with $N-1$ units, with the full DC-link voltage. The second fault scenario is the response to the overloading of a single module. An operation strategy for deloading single modules with minimum turbine power reduction is developed and the limits of this control mode are identified.

The concept of the modular, series connected converter is verified experimentally using a laboratory setup based on a 45 kW 270 V prototype of the special generator. The machine consists of three stator segments connected to three converter units. The experimental results are used to verify the feasibility of the control of the converter chain with a modular control approach. Additionally, the DC-droop control functionality is demonstrated. Finally, the fault-tolerant operation and control modes are verified.

Abbreviations, Acronyms and Nomenclature

Abbreviations and acronyms

AF-IL PMSG	axial flux ironless stator permanent magnet synchronous generator
BTB	back-to-back
CPL	constant power load
DFIG	doubly fed induction generator
EPC	external peripheral controller
FPGA	field programmable gate array
HVAC	high voltage AC
HVDC	high voltage DC
MPPT	Maximum power point tracking
IGBT	insulated-gate bipolar transistor
IO	input/output
ISC	indirect speed control
LVRT	low voltage ride through
MMC	modular multilevel converter
NPC	neutral point clamped
PLL	phase-locked loop
PMSG	permanent magnet synchronous generator
PWM	pulse width modulation
VSC	voltage source converter

General on nomenclature

The variable i is used for currents, and u for voltages. Upper case is used for SI values, and lower case for per unit. Subscript $_i$ indicates association with module i, $_f$ a faulty module and $_h$ a healthy module. The complete nomenclature is given in the back of the thesis.

Per unit is defined based on rated values for one single module.

The modules of the series connected converter are referred to as converter units or VSC units. The modules of the generator are referred to as (stator) segments. To distinguish between the DC voltage of a converter unit and the output DC voltage from the modular series connected converter, the term DC-bus voltage is assigned to the units, and DC-link to the entire converter string.

Contents

List of Figures

List of Tables

1 Introduction

1.1 Motivation

1.1.1 World energy demand

There is strong evidence that global warming is created by humanity's use of fossil fuels [1]. Additionally, even an optimistic forecast foresees a substantial increase in energy demand for the next few decades, Fig. 1.1[1]. This clearly demonstrates the necessity of developing new, renewable energy sources.

Throughout the last few decades, wind power has achieved considerable attention as perhaps the most promising new, renewable energy source for the next few decades. Onshore wind power technology can, to a certain extent, be regarded as mature: Given favorable conditions, it is proven to be competitive with traditional, fossil fuel sources [4, 5]. However, onshore wind power is facing increasing resistance in some regions of the world. As a consequence, attention has been directed to the possibilities found offshore. In addition to less political conflicts, the most appealing features are [6]:

- Stronger wind.
- More stable, less turbulent wind.
- Large available areas.
- Possibilities for larger turbines (less visibility, ease of logistics).
- Avoid difficult land transport.

Despite the better wind conditions, offshore wind power is still substantially more costly than onshore wind [4]. Marine foundation, grid connection, and operation

[1] "New policy" scenario as defined in [2] - "A scenario in the World Energy Outlook which takes account of broad policy commitments and plans that have been announced by countries, including national pledges to reduce greenhouse-gas emissions and plans to phase out fossil-energy subsidies, even if the measures to implement these commitments have yet to be identified or announced".

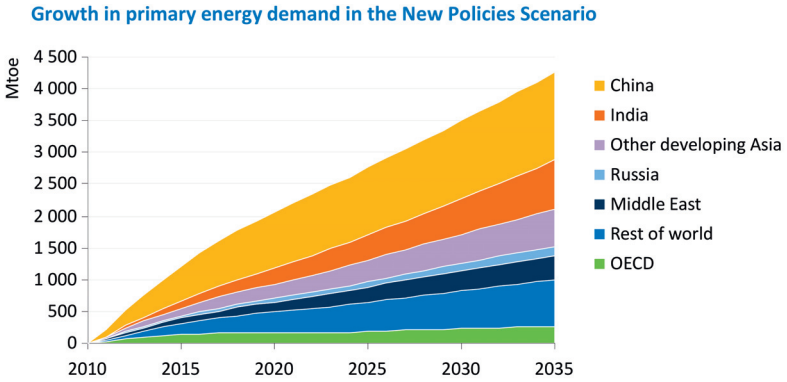

Figure 1.1: Growth in world energy demand from 2011, forecasted by the IEA, estimated for the "New Policy" scenario (The "New Policy" scenario assumes large reductions in energy consumption.) [3]. (In 2013, the total energy consumption was estimated to 12 000 Mega tonne oil equivalents (Mtoe).)

and maintenance ($O\,\&\,M$) are key cost drivers offshore, Fig. 1.2 [7]. The cost for the wind turbine itself is less than half of the investment costs, and only 34 % of the total energy cost[2]. Consequently, a better, but more expensive turbine design may be beneficial if the cost of other aspects is influenced positively.

1.1.2 Development in rated power of wind turbines

The power rating of wind turbines has increased almost exponentially from the 1980s, until the size development came to a halt around 2-4 MW in 2003-2004 [8]. This power limit was imposed by logistic limitations on land, but also visual pollution played a part. In recent years, renewed interest in larger wind turbines has been seen in both academia [9–11] and industry [12–14]. This interest is largely trigged by the offshore application. An example is the NOWITECH reference turbine, [9], which defines a basic design for a 10 MW, bottom fixed offshore turbine.

The main driver for larger turbines is the assumed energy cost decrease for offshore wind power associated with larger turbines [15]. This cost reduction is ascribed to difficult O&M-conditions and installation processes offshore: There are strict weather limitations for offshore operations, and fewer units will reduce the total number of operations. An up-scaling of today's turbine technology will, however, result in a substantial increase in drive train mass, since the mass of the generator increases more than linearly with power. For instance, the mass for a conventional,

[2]Total energy cost includes the investment costs, losses, operation, maintenance and decommissioning for the wind farm.

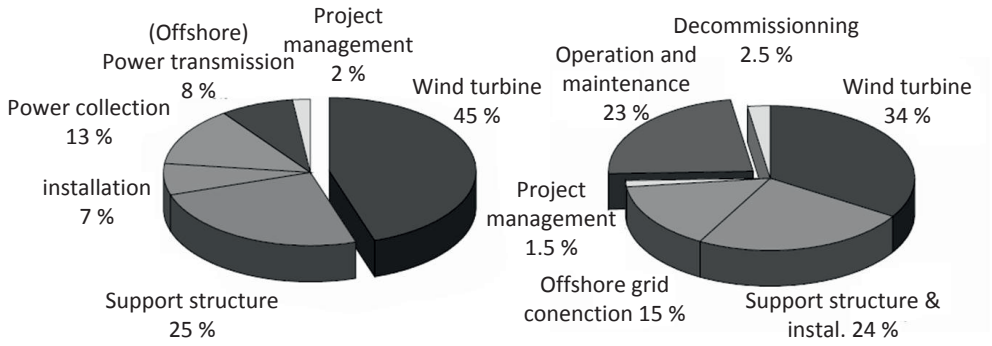

Figure 1.2: Breakdown of costs related to wind power [7]. Left: Investment cost. Right: Energy cost (investment-, operation-, maintenance- and decommissioning-cost).

3-phase 10 MW direct-drive permanent magnet synchronous generator (PMSG) is estimated to be approximately 300 tonnes [16].

An additional challenge is the standard rated voltage, 690 V(rms), used in existing wind power generator designs. For a 10 MW turbine, this results in a cable current of 8.4 kA. Hence, the cables from the nacelle down the tower, where the transformer is located in onshore turbines, will be heavy, and several parallel cables will be needed. Medium voltage level (2.3-6.9 kV(ll,rms)) outputs from the generator are under consideration [9, 17, 18], but the current is still considerable. The distribution transformer is therefore located in the top of the turbine. An additional reason to mount the transformer in the nacelle is that this will allow the completion of more of the installation process on land. However, this transformer adds weight to an already heavy nacelle, which is reflected on the tower construction. High weight will become an even more prominent issue for floating turbines. The transformer is also introducing a maintenance issue since it cannot be made modular, and an expensive offshore crane vessel is needed for the replacement in case of failure. Therefore, avoiding this transformer is assumed to be beneficial for the life cycle cost for offshore wind energy.

1.1.3 Offshore wind power and reliability

A major concern regarding offshore wind power is O&M [19]. The main reason is the decreased accessibility caused by the combination of harsh weather conditions and remote locations. According to [20], the main causes of downtime for onshore turbines have been problems with the gearbox and the generator. However, it is believed that faults in the electrical system will result in increased downtime for offshore turbines [21]. These electrical system faults occur more frequently, but are normally repaired in short time onshore. Offshore, the same fault will cause

lower average availability of the wind turbines due to the decreased access for maintenance operations [22].

As a consequence, research has started focusing on solutions which can reduce the overall downtime. Three main approaches are identified in [23]:

- Improvement of the component quality, leading to decreased failure rate.
- Improvement of the monitoring and recognition of component states which may lead to failures and break down. Based on such monitoring, stress-reducing operating strategies and preventive maintenance can be introduced. An additional benefit is the possibility to identify and clear false alarms[3].
- Introduction of fault-tolerant systems, such as a multi-phase generator with parallel, redundant converter units [24], or redundant power electronic switches in the converters [21].

1.1.4 Offshore grid connecting technologies

The grid solutions for offshore wind power are briefly reviewed here, in order to provide the necessary background for the analysis of a transformerless offshore wind turbine.

Main connection to shore

Onshore wind farms are normally connected to the grid using high voltage AC (HVAC). Offshore, the practical transmission distance limit of HVAC is quickly reached, and high voltage DC (HVDC) solutions are more beneficial. A transmission distance of 70-80 km is normally considered as the break-even point between HVAC and HVDC [25]. Of the two HVDC technologies available in the market, voltage source converter (VSC) based HVDC is considered the most suitable solution for offshore wind farm grid connection. The reasons are total footprint of the sub-station, black start capability and filter requirements. An offshore wind farm with an AC-distribution grid and HVDC connection is illustrated in Fig. 1.3

Internal wind farm distribution grid

The possibility to use a DC-distribution grid in future offshore wind farms has gained considerable attention the last decade. The motivation behind this interest

[3]False alarms occur when fault protection mechanisms are triggered based on wrong conditions.

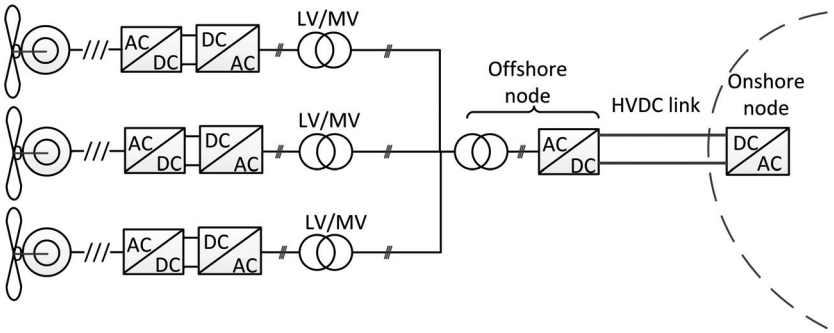

Figure 1.3: Connection scheme for an offshore wind farm with AC-distribution grid and HVDC connection to shore.

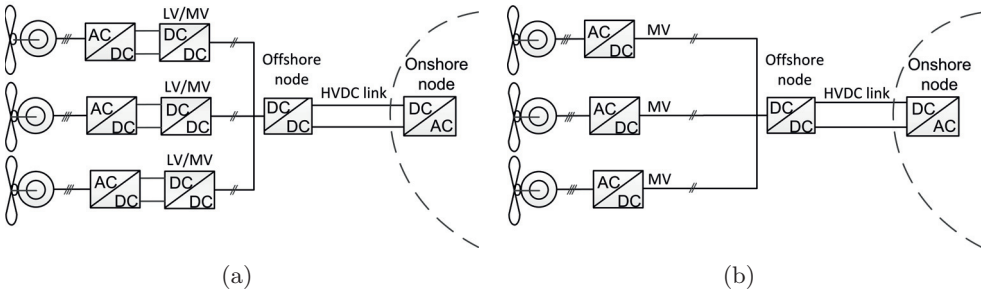

Figure 1.4: a) Offshore wind farm with medium voltage DC grid and HVDC connection to shore. b) DC wind farm with medium voltage output from the generator side converter.

is the possible reductions in investment costs and increased overall efficiency. DC-grid configurations for offshore wind farms are analyzed in [26, 27], and control aspects are addressed in [28, 29]. Given standard generator voltages, a step-up DC/DC solid-state transformer is required for each turbine to reach distribution level voltage, Fig. 1.4(a). A transformerless turbine technology may remove the need for this DC/DC converter, Fig. 1.4(b).

In place of the offshore AC/DC-converter in regular HVDC, the medium voltage DC-based wind farms will need DC/DC solid-state transformers [30–32] for the offshore node. These will boost the voltage from medium voltage DC to HVDC before transmission to shore. Another possibility to achieve transmission voltage level for DC grids is the series connection of turbines [33–35].

1.2 Research question and formulation of hypothesis

1.2.1 Development of research question

From the offshore wind power outlook presented in Sec. 1.1, the following trends regarding offshore wind power technology can be observed:

- The interest in offshore wind power is increasing, and will continue to grow in the future.
- New power-transmission solutions are being researched, due to long distances. DC grids are considered for both internal wind-farm grid and bulk transmission to shore.
- There is increasing interest and motivation for developing larger turbines. This development will force new turbine technologies as the limits of the existing concepts are being reached.
- The challenging O&M offshore favors robust solutions. Fault-tolerant and modular solutions for simplified maintenance will be beneficial.

As a consequence of these trends, the transformerless turbine concept is identified as a promising solution for large, offshore wind turbines. Since the interface between the generator and the grid is the power electronic converter, it is assumed that this converter will be a key component for the development of a transformerless technology. A main research question is formulated for this work:

How can the the power electronic converter be used to design a modular, lightweight transformerless wind turbine technology with medium- to high voltage DC output?

1.2.2 Main hypothesis

The literature review presented in Chapter 2 identified a direct-drive, lightweight generator technology with the possibility to include high voltage insulation as a suitable base technology. This insulation technology requires a special converter system for the integration into a high voltage grid (Concept 4, Table 2.1). With this background, it is possible to formulate a main working hypothesis for this thesis:

"By taking an integrated design approach to the power electronic converter and generator in the electric drive train of a very large wind turbine, it is possible to eliminate the need for a step-up, medium voltage transformer, but still achieve medium- to high voltage output from the turbine. Hence, weight can be saved, and possibly, maintenance can be facilitated compared to today's standard solution".

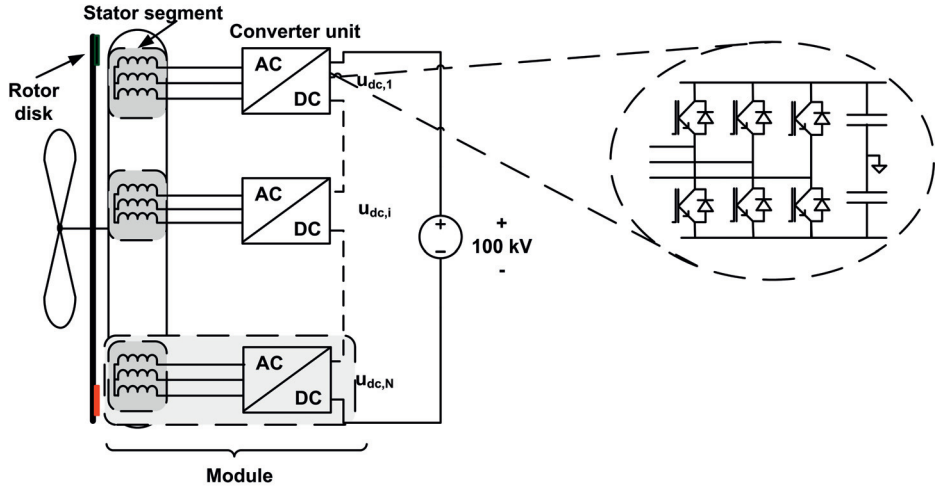

Figure 1.5: Principle of the modular, series connected voltage source converter configuration with N modules.

1.3 Contributions

1.3.1 Proposed system

In this thesis, a modular, series connected voltage source converter is proposed applied to a transformerless offshore wind turbine, Fig. 1.5. The system consists of a modular generator and the converter chain. The segments of the stator can be modeled as independent sub-generators (Sec. 3.1.3) which are parallel connected on the mechanical side. Each of the N 3-phase stator segment is connected to a unique unit of the modular series connected converter. The DC buses of the converter units are connected in series, in order to achieve a high, total output voltage. Thus, the internal voltage in each module is low, while the entire module floats on a high common mode DC voltage to ground. The detailed introduction to the system is given in Chapter 3. The analyses in this thesis are valid for any value of $N \geq 2$. For the numerical results, N=9 is used as base. The reason for this value, and the consequences, are discussed in Sec. 3.1.2 and Sec. 3.2.3 respectively.

1.3.2 Contributions

The contribution of this thesis is to analyze and investigate the suitability of the modular, series connected converter, with N units, for a large scale, transformerless offshore wind turbine, based on an axial flux ironless generator with a special machine-insulation solution. Emphasis is on identifying operational limitations, inherent advantages from the topology and possible draw backs which may make the solution unsuitable. The contribution is limited to the modular converter topology, and the understanding of how the special generator design impacts the converter design, operation and control.

The main contribution can be divided into the following points:

High voltage generator technology: Develop an understanding of how the modular power electronic converter should be designed to exploit the special generator insulation technology, to create a high voltage, transformerless offshore wind turbine.

Analyze fundamental properties of the series connected converter in relation with the segmented machine: The impact of the deviations of system module parameters from the ideal values is analyzed. An analytical model which relates module parameter variations to DC-bus voltages of the converter units is developed.

Stability of the series connection: The internal DC-voltage distribution for the converter units is found to be instable in current-control mode with the system operating in motor mode, based on a small-signal stability analysis. This instability cannot be improved by applying a stable, controlled output voltage for the series connected converter. Since motor mode can occur e.g. during acceleration of the turbine, this instability is relevant and a problem. For generator mode, the DC-voltage distribution is self-balancing and naturally stable.

Modular control structure: An earlier proposed control structure by Carmeli et al. [36] is analyzed further: The requirements for a modular, robust control strategy are identified, and the synthesis to obtain such a system is described. It is demonstrated that the synthesized module control system structure allows for change of converter-control strategy by adjusting the DC-bus voltage control references independently.

Torque-based DC-voltage droop control: For the modular control structure, a problem is identified which originates from an overdetermined DC-voltage-control system. A DC-voltage droop is proposed which solves this problem. The droop control is therefore a necessary part of the modular control. A frequency-response analysis is presented for the evaluation of the droop parameters.

Fault tolerance: Two possibilities to implement fault tolerance in the generator/converter solution are identified:

- It is shown that a converter unit trip results in a fail-to-safe transition with the system operating in the generator mode. Further, it is possible to reconnect the converter unit (in case of a detected false alarm) or bypass the module completely (redundant operation), while the turbine is operating. A quasi-steady-state analysis revealed that overrating of the semiconductor switches is necessary to ensure safe operation during this type of fault.
- A control strategy which allows for individual deloading if a single module experiences cooling problems is developed. The operation results in minimum output power reduction compared to the deloading of the module. The physical and operational limits for the fault-tolerant mode are identified.

Converter-control strategy impact: The impact of module parameter variations for different control strategies for the converter is identified. It is demonstrated that the preferred control strategy for the high voltage insulation, balanced converter unit DC-bus voltages, results in reduced power capacity for the turbine in the case of module parameter variations.

Experimental verification: The concept is verified experimentally using a 45 kW prototype of the generator, with 3 stator segments, and applying 3 converter units. The verification includes system modeling, modular control system and the fault-tolerant operational modes.

1.3.3 Limitation of the work

The work does not claim to solve the insulation problems related to high voltage generators. Additionally, the work does not address the issues related to the construction of a large diameter, ironless permanent magnet synchronous generator.

1.4 Publications

Included in thesis

1. **S. Gjerde** and T. Undeland, *Dynamic performance of the modular series connected converter in a 100 kV_{dc}- transformerless offshore wind turbine*, Oceans'13 MTS/IEEE Bergen, June 2013. *Conference*
2. **S. Gjerde**, K. Ljøkelsøy, R. Nilsen and T. Undeland, *A Modular Series Connected Converter Structure suitable for an HVDC transformerless Offshore Wind*

Turbine Submitted January 2013, accepted. Wind Energy, John Wiley & Sons, Ltd. *Journal*

3. **S. Gjerde**, P.K. Olsen, K. Ljøkelsøy and T. Undeland, *Control and Fault Handling in a Modular Series Connected Converter for a Transformerless 100 kV Low Weight Offshore Wind Turbine*, IEEE Transactions on Industry Applications, in review, July 2013, *Journal*.

4. **S. Gjerde**, K. Ljøkelsøy and T. Undeland, *Laboratory Verification of the Modular Converter for a 100 kV DC Transformerless Offshore Wind Turbine Solution*, Energy Procedia, Vol.35, (presented at Deepwind, Trondheim 2013). *e-journal*.

5. **S. Gjerde**, P.K. Olsen and T. Undeland, *A Transformerless Generator-Converter Concept making feasible a 100 kV Low Weight Offshore Wind Turbine Part II - The Converter*, IEEE Energy Conversion Congress & Expo, Raleigh,USA 2012. *Conference*

6. **S. Gjerde** and T. Undeland *Fault Tolerance of a 10 MW, 100 kV Transformerless Offshore Wind Turbine Concept with a Modular Converter System* EPE-PEMC, Serbia 2012. *Conference*.

7. **S. Gjerde** and T. Undeland, *A Modular Series Connected Converter for a 10 MW, 36 kV, Transformer-Less Offshore Wind Power Generator Drive*, Energy procedia, Vol.24, 2012, (presented at Deepwind, Trondheim, 2012). *e-journal*.

8. **S. Gjerde** and T. Undeland, *Power Conversion System for Transformer-Less Offshore Wind Turbine* Trondheim, EPE Joint Wind Energy and T&D Chapters Seminar, Trondheim 2011 *Conference*.

In agreement with the inventors of the generator insulation technology, the full 100 kV potential of the system was not communicated due to an ongoing patenting process in 7) and 8).

Relevant, not included

The following publications are relevant for the topic, but are not considered as part of the contributions in this thesis.

I T.M. Iversen, **S. Gjerde** and T. Undeland, *Multilevel Converters for a 10 MW, 100 kV Transformer-less Offshore Wind Generator system*, EPE Joint Wind Energy and T&D Chapters Seminar, Aalborg,2012. *Conference*.

II P.K. Olsen, **S. Gjerde**, R. Nilssen, J. Hølto and S. Hvidsten, *A Transformerless Generator-Converter Concept Making Feasible a 100 kV Light Weight Offshore Wind Turbine: Part I - The Generator* IEEE Energy Conversion Congress & Expo, Raleigh,USA 2012.*Conference*.

III **S. Gjerde**, B. Liu, R. Torres-Olguin, T. Haileselassie, T. Fuglseth and T. Undeland, *Offshore Vindkraft Modellering, Regulering Nettilkobling ved Kraftelek-*

tronikk NEF Møte, 2011, *Conference (in Norwegian).*

Other publications during the PhD work

A **S. Gjerde** and T. Undeland, *Control of Direct Driven Offshore Wind Turbines in a DC-Collection Grid within the Wind Farms*, PowerTech, Trondheim, June 2011, *Conference.*
B **S. Gjerde** and T. Undeland, *The Best Suitable Multilevel Converters for Offshore Wind Power Generators Without Transformers*, IPEC, Sapporo, June 2010, *Conference.*
C O. Anay-Lara, A. Endegnanew, J.O. Tande, H. Svendsen, K. Uhlen, **S. Gjerde**, K. Sætertrø, S. Gjølmesli, *Performance assessment of floating wind turbines during grid faults*, EWEA Amsterdam, 2011, *Conference.*
D O.G. Dalhaug, P. Berthelsen, T. Kvamsdal, L. Frøyd, **S. Gjerde**, Z. Zhang, K. Cox, E. Van Buren, and D. Zwick, *Specification of the NOWITECH 10 MW Reference Wind Turbine*, Norwegian Research Centre for Offshore Wind Technology (NOWITECH), 2012 *Technical report.*

1.5 Outline of thesis

The thesis is structured as follows:

In this chapter, *Chapter 1*, background, motivation, limitations and main contributions from the thesis are described.

In *Chapter 2*, state-of-the-art wind turbine technologies are presented. Generator solutions are discussed, before giving a review of existing research on transformerless solutions for large offshore wind turbines is presented.

In *Chapter 3*, the converter topology is presented, together with the high voltage generator technology. Steady-state relations between turbine operation and system parameters are derived. The converter unit fault handling is addressed, with emphasis on fail-to-safe and fault tolerance.

In *Chapter 4*, the control synthesis is presented with emphasis on achieving a robust, modular control system. The system is analyzed by frequency response and small-signal analysis.

Transient analyses based on simulations results are presented in *Chapter 5*, with focus on the dynamic performance of the DC-bus voltage controllers, and the operation of the converter chain in a turbine. Additionally, the fault scenario transients are simulated.

In *Chapter 6*, a proof-of-concept experimental verification is presented. The results are used to verify the modeling, operation and control of the modular series connected converter.

Chapter 7 contains the summary with concluding remarks, and proposed topics for further research.

2 Literature Review

This chapter present an overview of existing turbine technologies, and research on transformerless wind turbine generator/converter solutions. The emphasis is on power electronic converter solutions. A topology is identified for further analysis, and a brief discussion on generator technologies is included.

2.1 Existing variable speed offshore wind turbine technologies

Almost all offshore turbines are based on variable speed technologies. The reason is the enhanced power capture capability, and at the same time reduced mechanical stresses during rapid wind changes. However, there is still a large variety of drive train solutions for megawatt class offshore wind turbines: With- and without gearbox, full converter grid connection, partially rated converter, induction generator, synchronous generator and permanent magnet generator [37]. A technology overview sorted by the most common variations is presented in Fig. 2.1.

In recent years, the doubly fed induction generator and the different variations of the synchronous generator with fully rated converter have received most attention both from industry and academia. The two solutions are presented in detail in the following sections.

2.1.1 Doubly fed induction generator

The dominating technology for already installed offshore wind turbines is the doubly fed induction generator (DFIG), Fig. 2.2. According to [16], approximately 50 % of the turbines installed in 2011 were DFIG based.

The DFIG technology and the basic control system is described in [38, 39]. The concept consists of a multistage gearbox which couples the low-speed turbine shaft

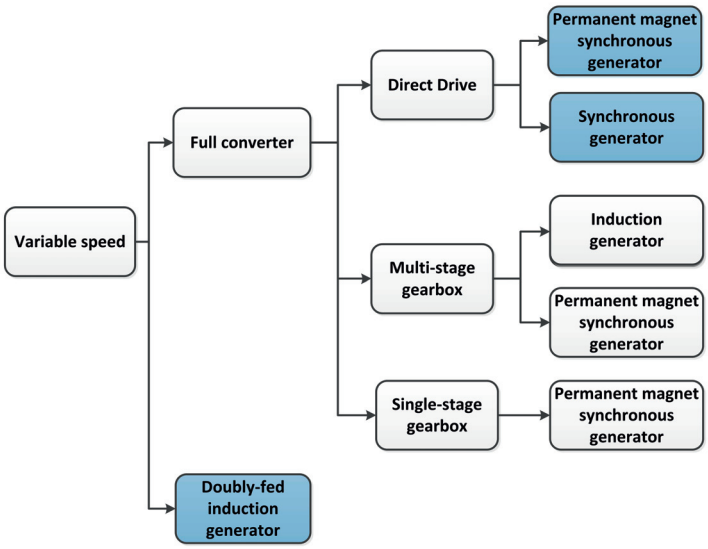

Figure 2.1: Overview of variable speed wind turbine technologies sorted by converter type, gear and generator type

to the high-speed generator shaft. The generator is an induction machine with wound rotor and slip rings. Traditionally, the output voltage is 690 V, connected to the grid via a step-up transformer. Variable speed operation is achieved with the back-to-back (BTB) VSC. The rated power of the converter is normally limited to around 25 % of the turbine nominal power, while the turbine speed range is ± 33 % [40].

The operation and control of a grid-connected DFIG wind turbine is proven through commercial experience, and well explored in the literature both with respect to grid faults [41–43] and reactive power capability [44].

The main concern for this technology is the multistage gearbox required to step up the shaft speed. Although this gearbox results in a smaller, lightweight generator, its drawbacks are significant: The reliability of large gearboxes is a major concern [20]. Gearbox failures are considered to be one of the most prominent causes for wind turbine downtime. Additionally, according to [45], approximately 1 % loss can be assumed per gearbox stage. This causes 70 % of the total losses in the system [46]. Even though the matter has been widely studied, the nature of the DFIG, with stator directly coupled to the net, makes it inherently vulnerable to grid faults. Finally, the slip rings of the DFIG introduce an additional reliability problem.

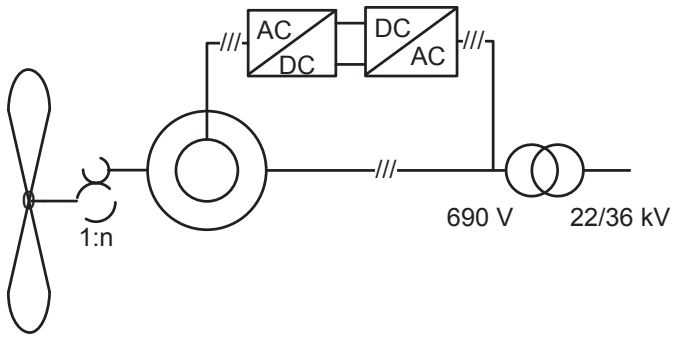

Figure 2.2: Doubly fed induction generator (DFIG) concept for a variable speed wind turbine, with multistage gearbox, induction generator, back-to-back converter and step-up grid transformer for grid connection.

2.1.2 Synchronous generator with fully rated converter

Full converter permanent magnet synchronous generator

There are both geared- and direct-drive full converter PMSG solutions for variable speed wind turbines, Fig. 2.3. The main motivation is the improved control and grid integration possibilities offered by the full converter solution. Due to the fixed excitation by the rotor magnets, the back-EMF of the machine is directly proportional to the turbine speed. Hence, an inverter is considered the preferred choice for the the AC/DC-converter on the generator side. However, it is also proposed to use a diode bridge and a DC/DC-boost converter, as a cheaper solution [47]. The diode bridge introduces higher harmonic content, and less controllability, and is mostly used for small, low-cost turbines. The standard PMSG-voltage is 690 V, but recent increases in turbine ratings have resulted in more interest for medium voltage solutions (i.e. 2.3-6.9 kV) [9, 17].

Grid compliance issues have been studied for the full-converter PMSGs [48–50], and the benefits of the full converter solution compared to partially rated converters have been demonstrated.

The direct-drive PMSG [51, 52] has received considerable attention as solution for large, offshore wind turbines. The technology is assumed to be robust, with low maintenance demand due to absence of gear and slip rings. The direct-drive turbine rotor is connected directly to the generator via a low speed shaft. A low rotational speed results in high torque, and hence, heavy machines.

The geared solutions have emerged as a response to the weight of large direct-drive generators, and the amount and cost of active material required for such generators. Recent developments in the price of rare earth magnetic-materials and the security of supply have added to the arguments against direct-drive PMSG. To

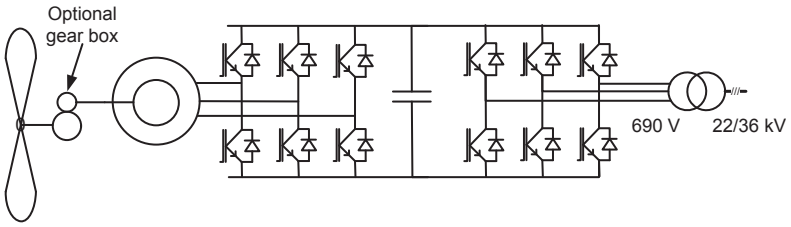

Figure 2.3: Schematic of a permanent magnet synchronous generator (PMSG) solution with optional gear, back-to-back (BTB) fully rated converter and step-up transformer for grid connection.

mitigate the issues associated with the multistage gearbox discussed in the DFIG paragraph, a single-stage gearbox is proposed [53, 54]. The single-stage gearbox yields benefits in terms of transmission losses and a simpler, more reliable gearbox. A reduced generator mass is obtained compared to direct-drive solutions [55].

The back-to-back converter can be split into several parallel converter modules for redundancy and loss optimization [56].

Electrically excited synchronous generator

The PMSG has received by far the most attention for turbines based on synchronous generator with fully rated converter during recent years. However, there are also examples on electrically excited direct-drive synchronous generator based wind turbines [57]. This concept is normally associated with the wind turbine manufacturer Enercon. Currently, the worlds largest turbine (July 2013), the 7.5 MW Enercon E-126, is based on this technology [14].

The advantage of the electrically excited synchronous generator over the PMSG is, that the excitation can be controlled. As a result, a diode rectifier can be used for the machine-side rectifier. However, this excitation circuit is normally regarded as a reliability issue. Additionally, the weight of the electrically excited machine is even higher than that of a PMSG.

2.2 Generator technologies for lightweight wind turbines

In the previous section, standard DFIG- and direct-drive-solutions are reviewed. The main limitations of the DFIG for turbines rated at 10 MW and more, is the need for a multistage gearbox. A gearbox replacement can cost up to 10% of original investment cost, and failure intervals have been reported to be approximately 5

years, which makes these problematic offshore [58]. Additional arguments against the standard, multistage gearbox are: Efficiency (1 % loss per stage) and weight due to scaling. Even the simpler single-stage gearboxes will be heavy at 10 MW (Appr. 180 tonnes, according to [55]). In the light of the demanding O&M found offshore, gearboxes in their present quality do appear a less beneficial solution than direct drive. The reliability issues and lack of modularity are evaluated to be more problematic than the benefit of economical optimization of machine cost at the present stage.

For the conventional, direct-drive synchronous generator technologies, the mass is the main concern. Therefore, the benefit of an ironless stator for direct-drive PMSGs has started to receive attention [59]. The shear stresses are significantly lower than for iron cores, and the support structure can be reduced compared to a regular machine. A medium voltage, 10 MW, axial flux ironless stator permanent magnet synchronous generator (AF-IL PMSG) is proposed used in the Sway Turbine design ST10 [18]. A total turbine weight saving of 20-30 % compared to standard PMSG solutions is claimed. An additional benefit of the AF-IL PMSG is that a modular design can be implemented [60].

A special insulation system for compact, high voltage machine designs, proposed by [61], is based on an ironless stator with modular structure. Additionally, this system requires a converter which can provide a DC voltage divided into multiple levels.

The machine technology identified as the basis for this thesis is, as discussed in the previous paragraphs, a modular direct-drive axial flux permanent magnet synchronous generator with ironless stator and special insulation technology. In the following section, different converter topologies for transformerless solutions are reviewed with this technology in mind. The generator technology details are presented in Sec. 3.1.

2.3 Review of existing research on transformerless generator/converter concepts suitable for offshore wind power

In Sec. 1.1.2, the arguments for why a transformerless solution is beneficial for large, offshore wind turbines are presented. Several generator/converter concepts suitable for such large, transformerless turbines have been proposed during recent years. The following paragraph presents a brief overview of the research in this field with the aim to identify a suitable converter solution for further research.

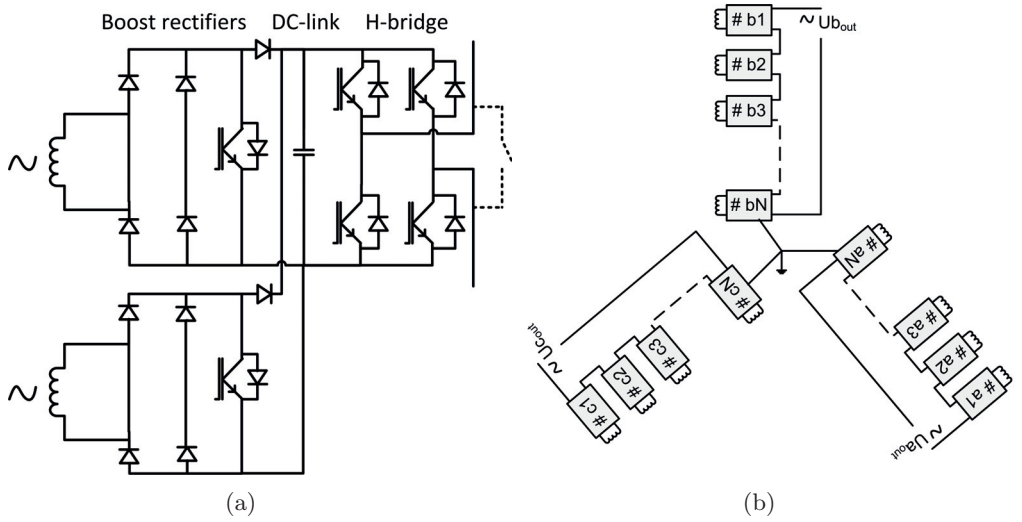

Figure 2.4: Single-phase converter solutions for transformerless wind turbine converter Concepts 1 and 2, CHB a) Single module b) System configuration. Figures recreated from [62] and [63] respectively.

2.3.1 Converters based on single-phase modules

Concept 1 (Table 2.1) is based on a special generator with multiple, concentrated coils [63–65]. Each of these coils is connected to a single-phase diode bridge which is controlled by a boost stage DC/DC converter. Two and two coils are paralleled, with a phase shift of 90°, Fig. 2.4(a). The output of the DC/DC-conversion stage is inverted by a single-phase H-bridge unit. An 11 kV AC output is achieved by cascading the H-bridge units' AC output, with one string for each phase. The high number of output modules results in a low grid-voltage harmonic distortion. In [62, 66], module fault-tolerant control and the distributed control of the system is analyzed. This distributed control introduces a challenge due to the synchronization with the grid AC-voltage frequency and phase.

A similar converter concept is proposed by [67–69](Concept 2).

In Concept 3, Fig. 2.5, a system with N parallel, 6-phase PMSGs mounted on the same shaft is proposed [70]. Each of the 6-phase stator windings is split into two sets of 3-phase windings. The set of 3-phase windings in a machine are phase shifted by 30° for harmonic cancellation. This multi-machine approach allows for multiple stator outputs without special stator core design, but results in a complex drive train. The output from each phase is rectified by a converter unit similar to those in Concepts 1 and 2 consisting of a diode rectifier, DC/DC-boost stage and an H-bridge. A distribution-output-voltage level is achieved by cascading the AC side of the H-bridge units.

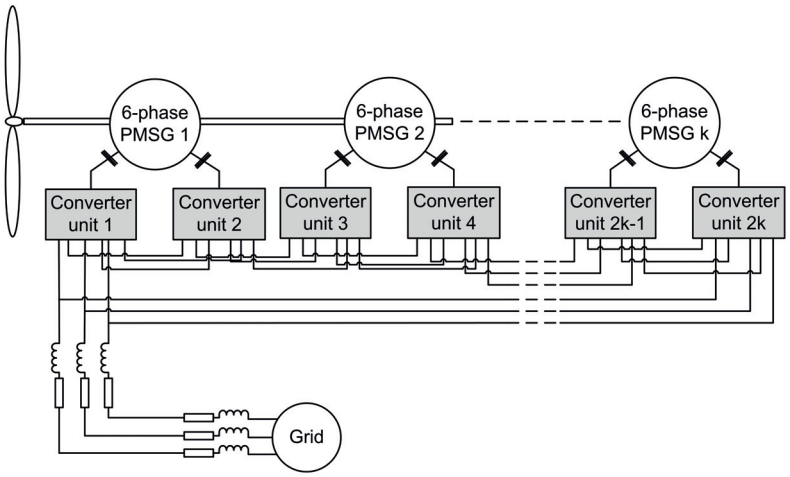

Figure 2.5: Multi-generator converter solution for transformerless wind turbine, Concept 3. Figure recreated from [70].

2.3.2 Converters based on 3-phase modules

A concept built around 3-phase voltage source converter units is introduced in [36] (Concept 4). The system is based on a PMSG with four electrically isolated 3-phase stator windings. Each 3-phase winding is connected to a three-level neutral point clamped (NPC) AC/DC-converter unit. The 3-phase units result in constant power in the modules, and hence less challenging control. A distribution voltage level, 23.6 kV DC, is achieved by series connection of the DC buses of the converter units. The module controllers are proposed to be implemented based on standard, 3-phase control theory, with minor additions for coordinated operation. Concept 4 is covered by a patent [71].

The series connection on the DC-bus side of the modules is beneficial when it comes to control coordination requirements. Since the DC-bus capacitors introduce a small buffer capacity, minor transient differences for the different modules may be mitigated. An issue with this topology may be the direct exposure of the capacitor bank to the DC-collection grid.

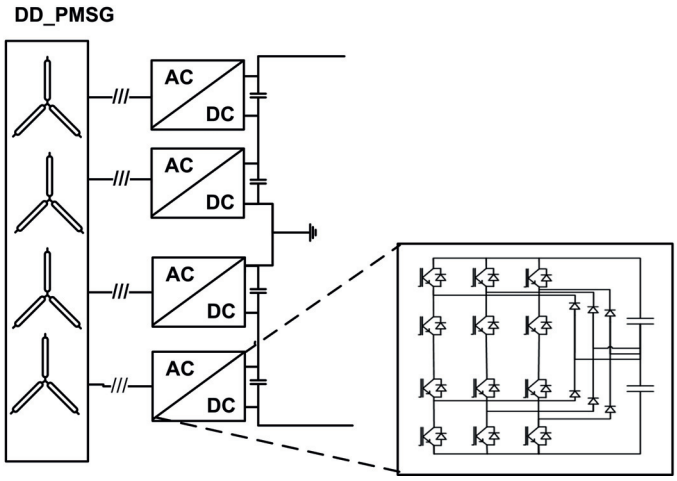

Figure 2.6: Converter solution for multiple, electrically isolated 3-phase stator winding groups, Concept 4. Figure reproduced from [36].

2.3.3 Series connection of wind turbines

Concept 5 is a solution where each turbine provides a medium voltage output, and the turbines are connected in series to achieve transmission level voltage [34, 35]. The concept employs a standard PMSG with a matrix converter, Fig. 2.7. The matrix converter output is a high-frequency AC voltage, which is stepped up in a high-frequency transformer. On the grid side of the transformer, the AC voltage is rectified. The conversion units are controlled as current source converters. This allows the DC-output voltage of each turbine to vary, while the DC current is kept constant. The concept is not truly transformerless. However, the high-frequency transformer is both lightweight and compact compared to its 50 Hz counterpart. Hence, the weight reduction goal for the transformerless technology is still fulfilled.

Series connection of turbines introduces a challenging control issue, due to power differences within a wind farm. Additionally, the insulation to ground is difficult.

2.3.4 Non-converter based concepts

The Concepts 1-5 all depend on a special converter topology to achieve distribution-voltage output. There are also other approaches for transformerless wind turbines. One such solution is to make use of cables for the stator windings, and thus include the insulation of the system directly in the generator. This makes it possible to obtain high voltage directly from the 3-phase output of the generator [72] (Concept 6, PowerFormer^{TM}). For such a system, the converter would be a 3-phase high voltage topology, similar to that used in VSC-HVDC stations. This machine

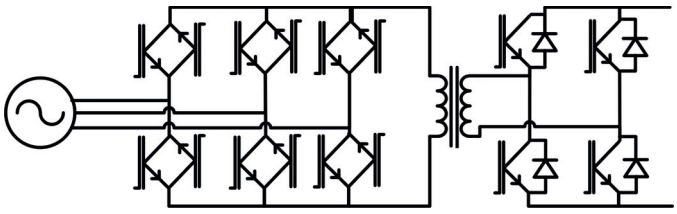

Figure 2.7: Topology of PMSG and matrix converter for series connection of offshore wind turbines, Concept 5. From [34].

technology is the only one of the reviewed transformerless concepts in commercial operation today [73]. However, this technology has gained reputation as a heavy machine, with a low fill factor. Its use is therefore restricted to applications where the total footprint limitations are more important than the weight.

A complete different approach is introduced in [74]: An electrostatic, variable-capacitance generator is proposed, with a claimed potential of 100-300 kV DC (Concept 7).

2.3.5 Summary of the concepts for transformerless wind turbines

The review of the existing research on transformerless solutions for wind power reveals that there is no consensus about how to approach the problem. The single-phase solutions (Concept 1-3) have received most attention so far. These fit well with the cascaded H-bridge inverter solutions and result in high-quality AC voltage at distribution level. On the downside, these require a complex control, and several conversion-stages. The 3-phase converters (Concept 4) has lower component count for a given voltage and power rating and the series connection may be simplified. The output is suitable for a DC-collection grid, without additional conversion stages. Finally, the DC-voltage output is split into multiple levels, with stable DC voltages, which are required for maximum utilization of the generator-insulation technology [61]. However, series connection of 3-phase voltage source converter units for a wind power application is scarcely explored in the literature.

A series connection of turbines (Concept 5) possess its own issues. Most dominant are the challenging coordinated control of turbines and insulation from turbine to ground. Concept 6 provides a proven solution for the high voltage insulation. This is, on the other hand, considered as too heavy for the wind power application.

Based on the discussion above Concept 4 is identified as most suitable for further research on converters for transformerless offshore wind turbines in this thesis.

Table 2.1: Summary, transformerless turbine concepts

System	Generator	Converter	Output voltage	Gen.weight
Concept 1	Spoked, ironless radial flux PMSG	CHB	11 kV(rms)	Lightweight
Concept 2	PMSG Multi coil	CHB	6-35 kV(rms)	N/A
Concept 3	Multi 6-phase PMSG	CHB	11 kV(rms)	N/A
Concept 4	**Multistar-PMSG**	**Modular VSC**	**23.6 kV(DC)**	**N/A**
Concept 5	PMSG	Matrix	N/A	Standard
Concept 6	Cable -PMSG	Diode and VSC	$\geq$ 20 $kV(rms)$	High
Concept 7	Electrostatic DC	N/A	100-300 kV(DC)	Standard

2.4 Summary of state of the art

2.4.1 Overview of the chapter

Existing and prospective wind turbine technologies are reviewed in this chapter. The emphasis is on converter solutions, output voltage and suitability for a large, offshore wind turbine. The industry standard DFIG solution for 2-4 MW class is presented first, followed by the synchronous generators with full converter. Based on this review it is concluded that for very large offshore turbines, i.e. 10 MW and more, the limitations in these conventional technologies will most likely be too severe.

Then, there is a brief discussion on generator technologies. A lightweight, ironless PMSG with a special high voltage insulation design is identified as the base technology for a transformerless offshore wind turbine. With this in mind, different transformerless converter concepts are evaluated. Concept 4 [36] is identified as the best suitable starting point of the reviewed solutions. This converter topology can exploit the benefits of the machine insulation system to the full. At the same time, it is expected to provide a robust series connection of converter units. Except for the proof of concept presented in [36], and application in [75], little research has been presented on this converter topology.

In the next chapter, the AF-IL PMSG and converter Concept 4 are presented in more detail, identifying the system properties, and analyzing the fundamental properties.

3 Proposed Converter Concept - Physical Properties

This chapter presents the generator/converter solution that is suitable for a high voltage DC transformerless wind turbine. The generator is described, with emphasis on its impact on the power electronic converter topology and control. The modular, series connected converter topology is presented. An analysis of the system steady-state characteristics is presented, and fault scenarios are identified and analyzed.

3.1 The generator technology

3.1.1 General description of the axial flux ironless stator permanent magnet synchronous generator

The generator base technology for the transformerless offshore wind turbine is an axial-flux permanent magnet synchronous generator with ironless stator [60, 76, 77]. The benefits of the ironless stator technology regarding machine weight are discussed in Sec. 2.2. For a given rated speed and power, the axial flux design results in a comparatively larger diameter than a conventional radial flux machine. For a 10 MW, slow-rotating axial flux machine, the diameter is in the range of 15-25 m. This results in a challenging mechanical support structure design which will require special attention.

Originally, the AF-IL PMSG was designed for a 3-phase medium-voltage winding layout [60]. The stator is assembled from several, identical stator segments, each consisting of a sufficient amount of coils to create a complete 3-phase winding. The segment windings are connected in series with the neighboring segments through external connection points, as illustrated in the left part of Fig. 3.1. In the figure, the windings within a stator segment are represented as a 3-phase inductor, and

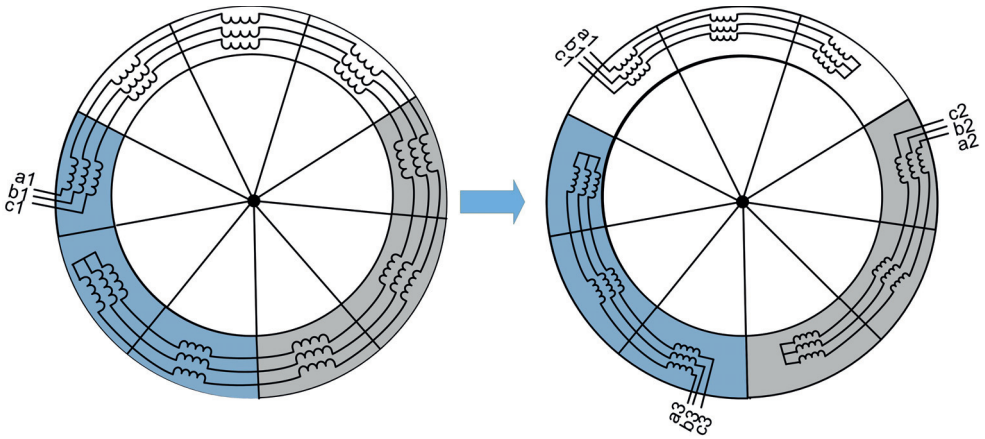

Figure 3.1: Simplified schematic for the stator winding lay out, seen in the axial direction of the machine with rotor disks removed. Left: The original 3-phase winding connection. (For the generator prototype used in the laboratory experiments, with nine stator segments). Right: Reconfiguration into three 3-phase isolated windings (with three stator segments in one winding set).

the machine is seen in the axial direction without the rotor disks. The external connections results in a modular generator which simplifies production, assembly and maintenance work. The use of external connections between the stator segments makes it straightforward to reconfigure the 3-phase stator winding into N electrically isolated 3-phase groups, right part of Fig. 3.1. These groups are distributed along the stator frame. As demonstrated in the figure, it is possible to connect several neighboring segments into one larger segment, depending on the desired amount of system modules.

The ironless, geometrically separated stator segments result in a weak magnetic coupling between the different parts of the machine. Thus, the magnetic field in one stator segment will not be affected of that in another stator segment.

The machine is isotropic. Hence, the direct- and quadrature axis reactances are equal: $x_d = x_q$.

3.1.2 High voltage machine insulation technology

Traditional electric-machine insulation techniques are not well suited for the construction of high voltage machines. There is a solution for handling high voltages in machines [72] (Concept 6, Sec. 2.3.5), but the low fill factor and resulting high weight makes it best suited for special applications.

An insulation solution which overcomes the problem of low fill factor in high voltage machines is presented in [61, 78]. Consequently, the high voltage version

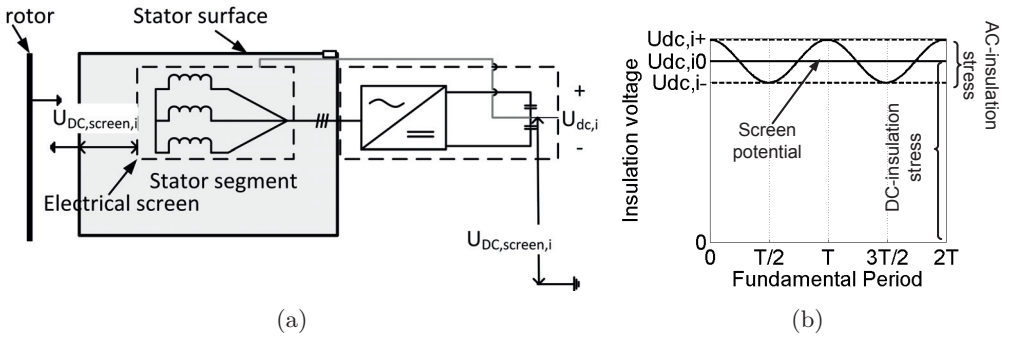

Figure 3.2: a) Principle of the electric screen technology connected to a converter unit on floating potential. b) Principle of the division of the insulation-voltage stress into an AC field and DC field.

of a machine can in theory be constructed with a power-to-weight ratio that is approximately equal to its low voltage counterpart. Within the boundaries of the existing, base generator design, a total voltage of 100 kV is achievable.

The principle of the solution is to divide the stator into N segments and connect each segment to a defined voltage level, Fig. 3.2(a). The voltage level imposed on the stator segment windings is a fraction of the total DC-output voltage, and the entire module floats on high voltage DC. Electric screens encapsulate each stator winding. These screens are clamped onto the corresponding DC-voltage level of the converter, $U_{dc,screen,i}$. This ensures that the common mode voltage of the stator segment equals the voltage level of the corresponding converter unit and decouples the total voltage into an AC- and a DC-field, Fig. 3.2(b). The converter AC-output voltage imposed on the stator winding equals the module DC-voltage, i.e. the DC-link voltage divided by N. The DC insulation outside the screen (epoxy in the ironless machine) can withstand higher field stress than AC insulation. As a result, the insulation around each stator segment can be reduced compared to AC- and hybrid-fields.

The two main benefits of the technology can be summarized as follows:

- Modularization reduces the line voltages in the windings substantially, to $1/N^{th}$, and hence the insulation requirement between coils in the same segment.
- The larger part of the voltage stress is moved from the AC field to the DC field, which requires thinner insulation.

The combination of these two points are exploited to design a high voltage, compact generator with a high fill factor: The turn insulation thickness is reduced to comply with the module AC voltage only. Hence, regular machine insulation can be used. Additionally, since the common mode voltage between segment and

ground is DC, this insulation can be optimized. Consequently, it is beneficial for the machine construction to consist of a high number of stator segments and voltage levels for a given total output voltage. All developments, results and conclusions throughout the thesis are general, and valid for any value of N. N=9 is used for numerical examples, since an estimate presented in [61] indicated that nine segments may yield an acceptable trade-off between machine size and system complexity for a 10 MW wind turbine with 100 kV DC output.

The strong link between stator segment insulation thickness and the module voltage levels (both common mode DC voltage, and phase-to-phase AC) indicates that knowledge of the maximum voltage-variations will allow for an insulation thickness optimization.

3.1.3 Model of the modular generator

In this section, the model for the AF-IL PMSG is developed. It is demonstrated how the absence of magnetic coupling leads to simplified generator model and control system synthesis. The generalized, dynamic model for an electric machine, in SI units, can be expressed by Eq. 3.1, defined for a generator.

$$\vec{U_s} = -\mathbf{R}\vec{I_s} + \frac{d}{dt}\vec{\Psi}_s^s \tag{3.1}$$

In Eq. 3.1, $\vec{U_S}$ is the stator voltage vector, $\boldsymbol{R}$ the stator resistance matrix, $\vec{I_s}$ the stator current vector and $\vec{\Psi}_s^s$ the stator flux vector.

The stator flux, $\vec{\Psi}_s^s$, is given by:

$$\vec{\Psi}_s^s = -\boldsymbol{L(\theta)}\vec{I_s} + \vec{\Psi}_r^s \tag{3.2}$$

where $\boldsymbol{L}$ is the stator inductance matrix, θ is the rotor position, and Ψ_r^s the remanence flux vector, produced by the permanent magnets. For an isotropic rotor, $\boldsymbol{L}$ is independent of θ.

Inserting Eq. 3.2 into Eq. 3.1 yields Eq. 3.3.

$$\vec{U_s} = -\mathbf{R}\vec{I_s} - \mathbf{L}\frac{d}{dt}\vec{I_s} + \frac{d}{dt}\vec{\Psi}_r^s \tag{3.3}$$

The last term in Eq. 3.3 is the induced voltage, $\vec{E_a}$:

$$\frac{d}{dt}\vec{\Psi}_r^s = j\Omega\Psi_r^s = \vec{E_a} \tag{3.4}$$

For a PMSG with N multiple, electrically isolated 3-phase connections, Eq. 3.1 can be expanded to Eq. 3.5:

$$
\begin{pmatrix} U_{a,1} \\ U_{b,1} \\ .. \\ U_{b,N} \\ U_{c,N} \end{pmatrix} =
$$

$$
- \begin{pmatrix} R_s & 0 & ... & 0 & 0 \\ 0 & R_s & ... & 0 & 0 \\ .. & .. & ... & .. & .. \\ 0 & 0 & ... & R_s & 0 \\ 0 & 0 & ... & 0 & R_s \end{pmatrix} \cdot \begin{pmatrix} I_{a,1} \\ I_{b,1} \\ .. \\ I_{b,N} \\ I_{c,N} \end{pmatrix}
$$

$$
- \begin{pmatrix} L & M_{a1,b1} & ... & M_{a1,bN} & M_{a1,cN} \\ M_{b1,a1} & L & ... & M_{b1,bN} & M_{b1,cN} \\ .. & .. & ... & .. & .. \\ M_{bN,a1} & M_{bN,b1} & ... & L & M_{bN,cN} \\ M_{cN,a1} & M_{cN,b1} & ... & M_{cN,bN} & L \end{pmatrix} \cdot \begin{pmatrix} \frac{dI_{a,1}}{dt} \\ \frac{dI_{b,1}}{dt} \\ .. \\ \frac{dI_{b,N}}{dt} \\ \frac{dI_{c,N}}{dt} \end{pmatrix}
$$

$$
+ j\Omega \begin{pmatrix} \Psi_{ra,1} \\ \Psi_{rb,1} \\ .. \\ \Psi_{rb,N} \\ \Psi_{rc,N} \end{pmatrix} \tag{3.5}
$$

In Eq. 3.5, $U_{x,i}$ is stator segment i phase voltage x, R_s the winding resistance, $I_{x,i}$ stator segment i phase current x. L the stator self-inductance, $M_{i,j}$ is the mutual inductance between two phases. Ω is the mechanical speed.

A weak magnetic coupling between the stator segments makes it possible to assume that $M_{i,j}$ between two segments is zero. By inserting zero for the mutual terms, Eq. 3.5 is reduced to a set of standard, 3-phase electric machines with common speed. Additionally, if the rotor position, θ_i, is tracked for each subsystem, an independent synchronous reference frame transformation can be applied to each stator segment. A standard 3-phase space vector description [79] can be adapted for each of the subsystems since the segments are reduced to independent machine models.

The resulting machine model is greatly simplified. It is completely separated into a set of N independent dq-models, Eq. 3.6. The d-axis is oriented with the rotor

flux in accordance with the definition in [80]. The model is given per unit, based on the rated values as defined in Table 3.1.

$$\begin{aligned} u_{d,1} &= -(r_{s,1} + p \cdot l_{s,1})i_{d,1} + n_{mech}x_{s,1}i_{q,1} \\ u_{q,1} &= -(r_{s,1} + p \cdot l_{s,1})i_{q,1} - n_{mech}x_{s,1}i_{d,1} + n_{mech}\psi_1 \\ &..... \\ u_{d,N} &= -(r_{s,N} + p \cdot l_{s,N})i_{d,N} + n_{mech}x_{s,N}i_{q,N} \\ u_{q,N} &= -(r_{s,N} + p \cdot l_{s,N})i_{q,N} - n_{mech}x_{s,N}i_{d,N} + n_{mech}\psi_N \end{aligned} \tag{3.6}$$

In Eq. 3.6, p is the derivative operator, n_{mech} is turbine speed and ψ_i is the stator flux linkage in stator segment i. $x_{s,i}$ is the synchronous reactance of a stator segment. The o-components are neglected in Eq. 3.6.

The rotor speed couples the different segments in Eq. 3.6, and the shaft dynamical model is described by Eq. 3.7:

$$\tau_m \frac{n_{mech}}{dt} = m_{turbine} - \frac{1}{N}\sum_{k=1}^{N} m_{em,i} \tag{3.7}$$

τ_m is the mechanical time constant, $m_{turbine}$ mechanical torque provided by the turbine rotor and $m_{em,i}$ the electromagnetic torque in one stator segment.

Eq. 3.6 and Eq. 3.7 are important for the synthesis of the modular control system presented in Chapter 4.

3.2 Power electronic converter topology

3.2.1 General description of the modular, series connected converter topology

In Sec. 2.3.5, Concept 4 is identified as the most suitable modular power electronic converter system for a transformerless offshore wind turbine based on the modular AF-IL PMSG. The series connection of N voltage source converter units allows for splitting the DC-output voltage into N levels, and connecting each level to a stator segment, Fig. 3.3. The DC-bus capacitors of the VSC units are split for mid-point access, onto which the electric screens in the stator are clamped. This ensures that the common mode voltage of the stator segment, $U_{dc,screen,i}$, is clamped to the level of the corresponding converter unit.

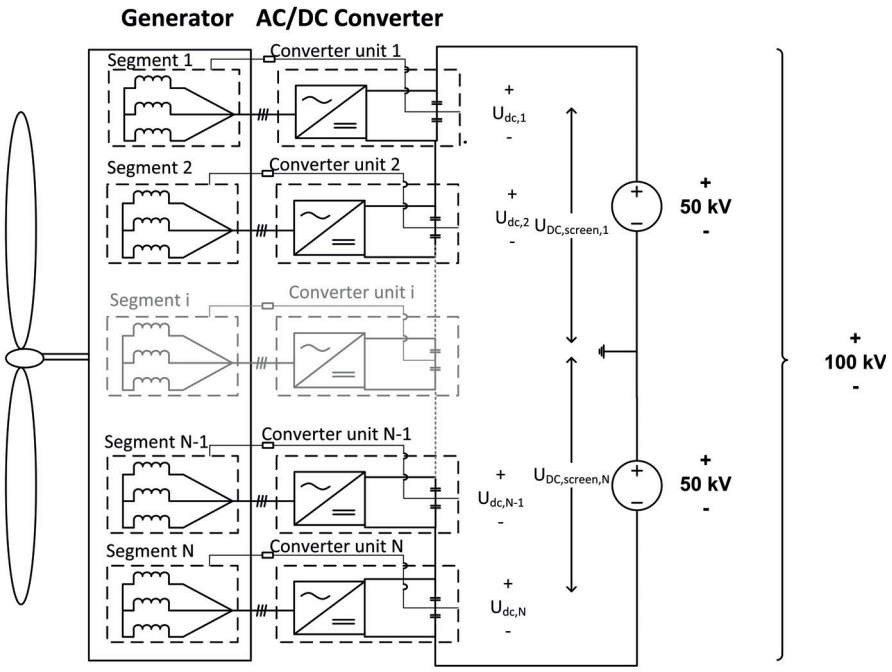

Figure 3.3: The proposed generator/converter system with stator segment windings, converter units and DC link, with N modules.

The series connection requires that the DC-side currents of the converter units are equal for steady state. Different DC currents in the converter units result in charging/discharging currents in the capacitors, since the main DC current is identical for the entire converter chain. The control system must be designed to take this into account. A benefit of making a series connection on the DC side is that there is no need to synchronize the output from the converter units. The reason is that small, transient differences in power between the modules will be absorbed by the capacitors, i.e. the DC-bus capacitors will function as buffers, contributing to a robust series connection. The DC-side series connection decouples the AC voltages between the segments.

Each of the converter units in the series connection floats on a high potential, equivalent to that of the stator segments. This requires high voltage insulation levels around each converter unit. A converter insulation solution is proposed in [81]. The working principle is similar to the machine insulation.

The combination of the special generator and the converter system discussed here makes it possible to achieve HVDC directly from the turbine without a transformer. Estimates in [61] have shown that 100 kV is feasible without compromis-

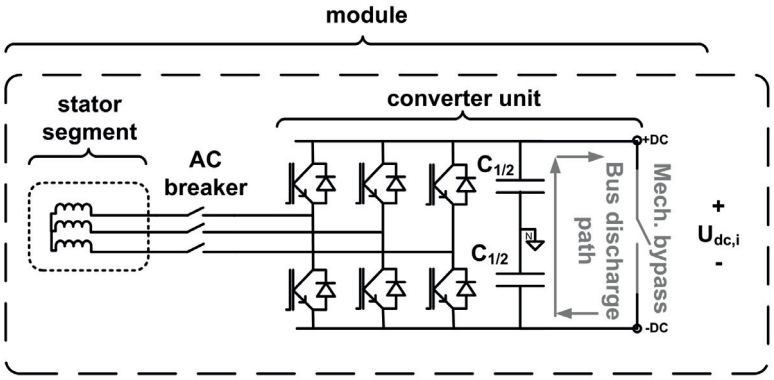

Figure 3.4: One submodule of the system with naming convention for the main parts. *Stator segment* is the generator part, *converter unit* refers to the 3-phase converter and *module* to the entire subsystem.

ing the weight of the PMSG.

3.2.2 Converter unit details

The converter unit of each module in this thesis is assumed to be a standard, 3-phase 2-level voltage source converter with insulated-gate bipolar transistor (IGBT)-based switches[1], Fig. 3.4. The bus capacitor is split for clamping of the stator segment screen to the DC-voltage level. A bypass breaker is included on the DC side of the converter unit, for bypassing a module in case of failure (see Sec. 3.5.2). The AC breakers between stator segment and converter unit are necessary for decoupling the segment in the case of a bypass.

The combination of 100 kV DC-bus voltage and N=9 modules results in a DC-bus voltage of 11.11 kV for each converter unit during normal operation. According to [82], the recommended peak-repetitive-voltage rating, U_{DR}, for a switch is given as:

$$U_{DR} = U_{DC,i} \cdot \left(1 + \frac{y}{100}\right) \tag{3.8}$$

Where y is a safety factor which depends on the converter design.

y is normally recommend to be in the range between 50 and 60. For 2-level VSC-modules, the DC-bus voltage, $U_{dc,i}$ = 11.1 kV and y=60, the minimum, peak repetitive voltage for one switch becomes 17.8 kV. This is above the blocking

[1] A switch is made from one or more semiconductor elements connected in series.

voltage for conventional IGBTs. Hence, a series connection of devices is required for each switch to obtain sufficient blocking voltage.

The series connection of semiconductors required to achieve sufficiently high blocking voltage suggests that a multilevel converter unit topology may be a preferred alternative over the 2-level VSC. A study of different multilevel VSC converters for the units is presented in [83]. The analysis is qualitative, and considers the following factors: voltage output quality, semiconductor voltage levels, controllability, possibility for redundancy and performance in a series connected converter topology. The most suitable topology was found to be the modular multilevel converter (MMC) [84], with five levels. An MMC can achieve high apparent switching frequencies in addition to high efficiency in high voltage applications [85].

With the MMC units, the converter chain ends up as a modular converter with modularity within each unit. From a control/complexity point of view, this is challenging. But at the same time, it is appealing for implementation of redundancy.

In the same study, the behavior of the modular, series connected converters with 5-level MMC and 2-level VSC units are compared. The main difference is found to be the harmonic content, while input/output performance is equivalent. Hence, studying the system with 2-level converter units does not compromise the generality of the results.

An alternative to the VSC is a diode bridge and DC/DC converter. This is normally considered to be less costly. However, this sacrifices some controllability compared to a full converter. Additionally, the diode bridge generates 5^{th} and 7^{th}-harmonics in the stator current [86]. This will result in substantial 6^{th}-harmonic ripple in the electromagnetic torque, which may cause problems for the mechanical system.

3.2.3 Discussion on the realism of 100 kV output voltage, and number of modules

The system voltage level, 100 kV, which is considered in this thesis is chosen to show what is considered feasible with the presented technology. It should be seen as an academic study, demonstrating the potential of the technology. Based on this analysis, it is an engineering job and economic optimization to choose the final voltage levels and number of modules. 100 kV may prove to be too high in distribution grids, since this requires HVDC-protection solutions for each turbine. In this context, 10 MW is a very low rating, for which the high voltages are not normally considered. Hence, the equipment in this power- and voltage-range may

be very specialized. At the same time, the voltage may be too low for long distance transmissions, and a central step-up converter on the offshore node is not omitted.

Another issue which occurs with N=9 modules is the ratio between the converter unit voltage- and power-rating. 11 kV DC bus is in the upper range of medium voltage drives segment (line voltage of 2.3-6.9 kV). In the previous section, an MMC topology is proposed for the converter units. This alone suggests that the resulting blocking voltage is too high for a modular system, and that N=9 modules should be reconsidered. A benefit of modular systems is the possibility to simplify each module and make use of mass produced units. To really benefit from such mass production, standard converter units will be beneficial. In the next paragraph, the additional challenges related to medium voltage converters compared to low voltage converters are discussed. It is demonstrated that care should be taken when choosing both system- and module-voltage levels.

Challenges related to medium-voltage converters

The low-voltage range of converters (690 V(rms)) is generally considered to provide mature products, based on IGBTs in the 1200-1700 V segment, and are available from many manufacturers [87]. These devices are considered to be highly reliable. Switching frequencies are in the range of 4-8 kHz, resulting in compact passive components, and low machine noise. Mostly, the low-voltage converters are 2-level VSCs, although [88] demonstrated some benefits of a 3-level NPC topology.

Converters in the medium-voltage range face more challenges than their low-voltage counterparts, and are considered for applications where the power level results in very high currents, and hence large amounts of copper and conduction losses at low voltage. One of the main challenges is losses associated with switching of high voltage semiconductors. Both heat-sink size reduction and thermal constrains demand a reduction of switching losses, and hence reduced switching frequency [89]. Consequently, the size of passive components increases, or higher harmonic content of current and voltage must be tolerated. Higher harmonics will cause additional losses in the machine, and introduce stress in the mechanical system. Some of these harmonic issues may be overcome by introducing multilevel converter topologies [90]. However, the added components results in decreased reliability. As a final remark, the machine insulation is subject to higher stress due to the switching in medium voltage compared to low voltage applications [91]. Also, the creep distances, clearance and auxiliary equipment design become more challenging.

Even within the medium-voltage range, there are significant differences in perfor-

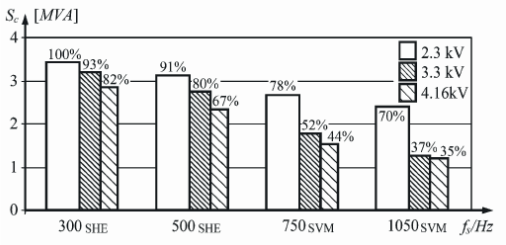

Figure 3.5: Maximum output power as function of switching frequency and voltage level. SHE is selective harmonic canceling, and SVM is space vector modulation [92].

mance between voltage levels. In [92], the consequences of increasing from the low- to high-end of medium voltage are analyzed for a three-level NPC-VSC for different switching frequencies. The evaluated converters are based on one IGBT per switch, i.e. increased converter voltage rating equals higher semiconductor voltage rating. The reduction of maximum output power relative to converter rating is especially prominent for the highest output voltage (i.e. 4.16 kV).

Some of the disadvantages associated with medium-voltage converters may be mitigated by the introduction of Silicon Carbide (SiC), i.e. higher switching frequency at elevated voltage ratings [93, 94]. However, SiC technology is still under development.

The optimization of voltage levels and number of modules is not considered further in this thesis.

3.3 System rated parameters

The most important system parameters, used for numerical examples in the analysis, and simulations, are listed in Table 3.1. The parameters are given for a 10 MW wind turbine, with N=9 modules and 100 kV DC output.

Table 3.1: System rated parameters

Parameter	*Value [unit]*
Turbine rated power	10 MW
Total, output DC voltage, $U_{dc,tot}$	100 kV
Number modules, N	9
Generator segment nominal power	1.11 MVA
Stator segment nominal voltage U_n	6.46 kV_{rms}
Generator nominal current $I_{s,n}$	99.2 A_{rms}
Generator electrical frequency f_n	29.6 Hz
Synchronous reactance $x_d = x_q$	0.33 pu
Stator resistance r_s	0.02 pu
DC-bus rated voltage $U_{dc,n}$	11.11 kV
Nominal depth of modulation, $u_{cmd,n}$	0.95
DC-bus capacitor C_i	340 μF
Modulation carrier frequency f_{sw}	1 kHz

It is assumed that the DC-link voltage is a fixed voltage controlled by a central converter unit.

3.4 System steady-state characteristics

3.4.1 Generalized input/output-model

The ironless axial flux generator design results in a large diameter electric machine for a 10 MW wind turbine, in the range of 15-25 m. As a result, small tolerances may lead to differences in the stator segment parameters (as is observed in the experimental results, Sec. 6.2). The stator segment flux linkage, ψ_i, stator resistances ($r_{s,i}$), converter efficiency (η_i), bus capacitance (c_i) and stator reactances ($x_{s,i}$) may vary between the modules. The impact of such variations on the overall system-performance is analyzed in the following sections.

The parameter variations will impact the DC-power output from the different modules. Hence, also the distribution of the total DC-link voltage between the converter units will be influenced. The steady-state relation between the voltage of an arbitrary converter unit, $u_{dc,i}$, the DC power of that module, $p_{dc,i}$, and the total DC-link voltage, $u_{dc,tot}$ is expressed by Eq. 3.9. Steady state demands that the DC-link current $i_{dc,link}$, is equal to the DC-bus currents of all converter units, $i_{dc,i}$, i.e., the average bus-capacitor current, $i_{c,avg}$, is zero.

$$\begin{aligned} u_{dc,i} \cdot i_{dc,i} &= p_{dc,i} \\ \Rightarrow u_{dc,i} &= \frac{p_{dc,i}}{i_{dc,link}} \\ \Rightarrow u_{dc,i} &= \frac{p_{dc,i}}{p_{tot}} \cdot u_{dc,tot} \end{aligned} \tag{3.9}$$

p_{tot} *is the total turbine output power.*

Eq. 3.9 describes a basic, important feature of the series connection: The bus voltage of a module is directly proportional to its contribution to the total output power. This means that if all N converter unit DC-bus voltages are to be balanced, all modules are required to contribute with the same DC power.

In Eq. 3.10, Eq. 3.9 is expanded to take into account differences in the electromagnetic torque between the modules (the system losses are neglected at this stage). The output power from each converter unit, $p_{dc,i}$, equals the electromagnetic torque, $m_{em,i}$ multiplied by the shaft speed n_{mech}. $m_{em,i}$ is the product of the stator segment flux linkage, ψ_i, and module q-axis current, $i_{q,i}$.

$$\begin{aligned} p_{tot} &= p_{dc,1} + p_{dc,2} + ... + p_{dc,N} \\ p_{dc,i} &= m_{em,i} n_{mech} = \psi_i \cdot n_{mech} \cdot i_{q,i} \\ \Rightarrow p_{tot} &= n_{mech} \cdot (\psi_1 i_{q,1} + ... + \psi_N i_{q,N}) \end{aligned} \tag{3.10}$$

Combining Eq. 3.9 and Eq. 3.10 yields Eq. 3.11.

$$u_{dc,i} = \frac{\psi_i \cdot i_{q,i}}{(\psi_1 i_{q,1} + ... + \psi_N i_{q,N})} \cdot u_{dc,tot} \tag{3.11}$$

The DC-bus voltage in module i depends on the stator segment flux linkage and the current $i_{q,i}$, Eq. 3.11. This relation is valid within the operating range of the voltage source converter units. In certain situations, the AC current in a single module may be restricted by the protection system due to special operating

conditions. This results, according to Eq. 3.11, in a decreased DC-bus voltage in the affected module. The reduction is limited by the condition at which the diodes of the VSC unit starts to conduct independent of the IGBT operation. When this occurs, control of the converter is lost. For normal loading, standard 120° conduction, Eq. 3.12 represents the minimum DC voltage, expressed in per unit. (For the equations given in SI units, see Appendix A.3).

$$u_{dc,i} = n_{mech}\left(\frac{3\sqrt{3}}{2\pi}u_n - \frac{9}{8\pi}x_s i_{dc,link}\right) \tag{3.12}$$

For Eq. 3.12, it is assumed that the line voltage for a given turbine speed, $u_{ll,rms}$ can be approximated by Eq. 3.13 in per unit.

$$u_{ll,rms} \simeq n_{mech}u_n \tag{3.13}$$

where u_n is the nominal voltage.

The last term in Eq. 3.12 is the voltage drop due to commutations as a function of segment synchronous reactance and the DC current. Eq. 3.12 is valid for passive rectifier with constant DC current. The reason why it may be applied here is that, seen from one single converter unit, the N-1 remaining converter units appears as an approximate current source.

At heavy loading of the machine, the limit may be approximated with square wave (six step)-operation of the converter unit, Eq. 3.14.

$$u_{dc,i} = \frac{\pi}{4}n_{mech}u_n \tag{3.14}$$

The transition from 120° to continuous conduction occurs around 183 A (Appendix E.5). Since 183 A is 83 % higher than the module rated current, this operation is not considered further[2].

[2]The per unit reactance is in this thesis chosen to be equal to that of the laboratory prototype. Given the low nominal current, this value may be low compared to what it will be for the full scale machine. Hence, continuous conduction mode may seem realistic at rated conditions for this full scale machine.

Eq. 3.15 is a valid approximation for $u_{dc,min}$ if the converter operating in no load/lightly loaded, and the phase current goes to zero for each commutation:

$$u_{dc,i} = \frac{\sqrt{3}}{2} n_{mech} u_n \tag{3.15}$$

The impact of this voltage limit is further discussed in Sec. 3.5.3.

3.4.2 Detailed steady-state model for the DC voltage of one module

In the following paragraphs, Eq. 3.11 is extended to include the module parameter variations. For the development, it is assumed that the module currents are controlled and identical. The q-axis currents, $i_{q,i}$, are associated with torque, and d-axis current, $i_{d,i}$, with stator flux control. Under normal operation, $i_{d,i} = 0$.

The AC- and DC-power in module i are according to Eq. 3.16:

$$\begin{aligned} p_{ac,i} = Re\left\{\vec{u}_{dq,i} \cdot \vec{i}^{*}_{dq,i}\right\} \Rightarrow p_{ac,i} &= u_{q,i} \cdot i_{q,i} \\ p_{dc,i} &= u_{dc,i} \cdot i_{dc,i} \end{aligned} \tag{3.16}$$

$\vec{u}_{dq,i}$ is the dq-voltage vector, $\vec{i}_{dq,i}$ the dq-current vector of module i.

Steady state requires that $i_{dc,link}$ is equal for all series connected converter units. By setting the AC- and DC-power in a module equal (Eq. 3.16) and including the converter efficiency, η_i, the resulting DC-bus voltage for the converter unit is given by Eq. 3.17:

$$p_{dc,i} = \eta_i \cdot p_{ac,i} \Rightarrow u_{dc,i} = \frac{\eta_i \cdot u_{q,i} i_{q,i}}{i_{dc,link}} \tag{3.17}$$

According to Eq. 3.6, one stator segment, with $i_{d,i}$ set to zero and transient terms eliminated, results in Eq. 3.18.

$$\begin{aligned} u_{d,i} &= n_{mech} x_{s,i} i_{q,i} \\ u_{q,i} &= -r_{s,i} i_{q,i} + n_{mech} \psi_i \end{aligned} \tag{3.18}$$

Inserting Eq. 3.18 into Eq. 3.17 results in Eq. 3.19. This expression relates the DC-bus voltage to the stator segment parameters and the DC-link current, $i_{dc,link}$:

$$u_{dc,i} = \frac{\eta_i \cdot (-r_{s,i} i_{q,i} + n_{mech} \psi_i) \cdot i_{q,i}}{i_{dc,link}} \tag{3.19}$$

An expression for $i_{dc,link}$ is developed, based on describing the the turbine output power for AC- and DC-quantities $p_{dc,tot}$, Eq. 3.20 and Eq. 3.21:

$$p_{dc,tot} = \sum_{i=1}^{N} (\eta_i \cdot u_{q,i} i_{q,i}) \tag{3.20}$$

$$p_{dc,tot} = \sum_{i=1}^{N} u_{dc,i} \cdot i_{dc,link} \tag{3.21}$$

For an ideal current control system, $i_{q,1} = ... = i_{q,N} = i_q$.

By combining Eq. 3.21 and Eq. 3.20, an expression for $i_{dc,link}$ is obtained as a function of the turbine operating point, Eq. 3.22:

$$\begin{aligned} i_{dc,link} \cdot \sum_{i=1}^{N} u_{dc,i} &= i_q \cdot \sum_{i=1}^{N} (\eta_i u_{q,i}) \\ \Rightarrow i_{dc,link} &= \frac{i_q \cdot \sum_{i=1}^{N} (\eta_i u_{q,i})}{\sum_{i=1}^{N} u_{dc,i}} \end{aligned} \tag{3.22}$$

Eq. 3.22 combined with Eq. 3.18 results in Eq. 3.23.

$$i_{dc,link} = i_q \cdot \frac{\sum_{i=1}^{N} (-r_{s,i} i_{q,i} + n_{mech} \psi_i)}{u_{dc,tot}} \tag{3.23}$$

Finally, by combining Eq. 3.19 with Eq. 3.23, an expression for the steady-state DC-bus voltage in converter unit i is obtained, Eq. 3.24. The voltage is given as function of the turbine operating point, module parameters and control settings.

$$u_{dc,i} = \frac{\eta_i \cdot (-r_{s,i} i_q + n_{mech} \psi_i)}{\sum_{j=1}^{N} \eta_j \cdot (-r_{s,j} i_{q,j} + n_{mech} \psi_j))} \cdot u_{dc,tot} \tag{3.24}$$

The physical interpretation of Eq. 3.24 is that the DC-bus voltage of a converter unit is a function its parameter deviation from the average of the parameters for

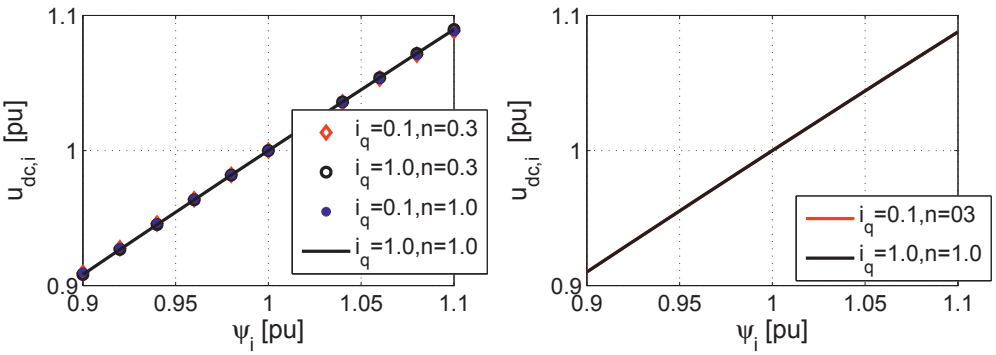

(a) (b)

Figure 3.6: The DC-bus voltage in one module as function of variations in stator segment flux linkage and converter unit efficiency for different system loading. N=9 modules. a) Variable stator segment flux linkage. b) Converter unit efficiency.

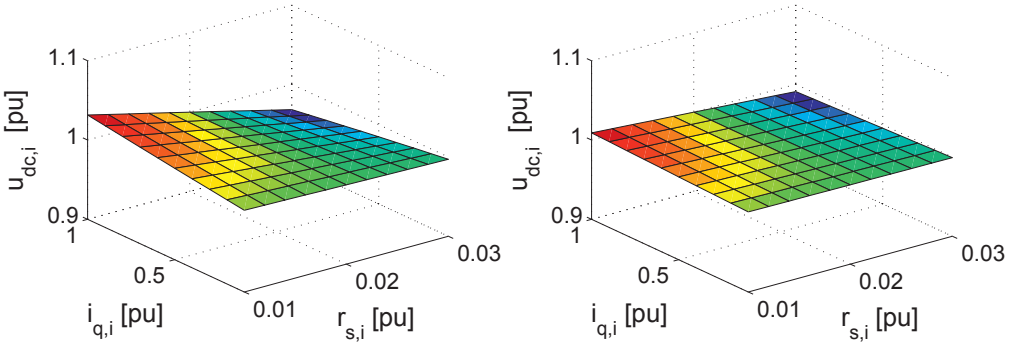

(a) (b)

Figure 3.7: The DC-bus voltage in one module as function of its variations in stator resistance, N=9 modules. a) 0.3 pu speed. b) Nominal speed.

all modules. Additionally, the DC-voltage distribution is independent of stator reactances and converter-bus capacitances in steady state.

Steady-state module DC-voltage estimates

The DC-bus converter unit voltage as a function of module parameter variations from the nominal is assessed based on Eq. 3.24 combined with Table 3.2. Two turbine speeds are considered: Start-up speed (0.3 pu) and nominal speed (1.0 pu). $u_{dc,i}$ is analyzed for deviations in the converter unit efficiency, stator-segment flux linkage and winding resistance, for a q-axis current ranging from 0.1 to 1.0 pu. The results are presented in Fig. 3.6(a) to Fig. 3.7(b).

Table 3.2: Nominal parameters for DC-bus voltage estimation

Parameter	*Value*
Rated stator resistance, $r_{s,n}$	0.02 pu
Rated efficiency, η_n	98 %
Rated stator flux linkage, ψ_n	1.0 pu
Number of modules, N	9

At cut-in speed (0.3 pu), the parameter which has the largest impact is the converter efficiency, Fig. 3.6(b), which is independent of the turbine speed. Variable stator segment resistance, $r_{s,i}$, introduces a small, but notable difference in the voltage at start-up, Fig. 3.7(a). For a variable resistance, the DC-bus voltage is also notably depending on the module current loading. The effect of variable resistance is negligible at nominal speed, Fig. 3.7(b). Stator-segment flux linkage variations are generally causing the same deviations from the DC-bus voltage independent of speed, Fig. 3.6(a). However, at low speed, the ohmic losses will result in a relatively larger impact of the variations due to lower active power. Around nominal speed, the effect of the parameter variations can be approximated by Eq. 3.25:

$$u_{dc,i} = \frac{\eta_i \cdot \psi_i}{\sum_{j=1}^{N} \eta_j \cdot \psi_j} \cdot u_{dc,tot} \tag{3.25}$$

Since it is beneficial for the machine insulation and the operation of converter units to have balanced DC-bus voltages, Fig. 3.6(a)-Fig. 3.7(b) demonstrates the necessity of a DC-bus voltage balance control.

3.4.3 Turbine derating due to parameter deviations

In Sec. 3.1, it was emphasized that the DC-bus voltages of the modules should be kept equal for optimal distribution of insulation stress. This requires that the power differences between modules due to parameter variations, Eq. 3.24, are compensated. Such a compensation must be obtained through different current loading of the stator segments since the speed is common. Hence, the current limit will be reached in some modules before others. A derating of the turbine will be required, to ensure continuous safe-operation of all modules[3]. In the following, an expression for this derating is derived, as function of module parameter deviations.

[3]This derating is not design derating, but operational derating to maintain a control reserve.

The q-axis current in a module is expressed by Eq. 3.26 and Eq. 3.27, based on the power balance across a converter unit, including the efficiency of the converter.

$$i_{q,i} = \eta_i \frac{u_{dc,i} \cdot i_{dc,i}}{u_{q,i}} = \eta_i \frac{p_{dc,i}}{u_{q,i}} \tag{3.26}$$

$$i_{q,i} = \eta_i \frac{p_{dc,i}}{(-r_{s,i} i_{q,i} + n_{mech} \psi_i)} \tag{3.27}$$

Further, the average q-axis current in the modules can be expressed as (Eq. 3.28):

$$i_q = \frac{1}{N} \sum_{i=1}^{N} i_{q,i} \tag{3.28}$$

By combining Eq. 3.28 with Eq. 3.26, a relation between module i DC power and the average q-axis current is obtained, Eq. 3.29.

$$i_q = \frac{1}{N} \sum_{i=1}^{N} \left(\eta_i \frac{p_{dc,i}}{u_{q,i}} \right) \tag{3.29}$$

If the maximum current, i_{max}, is reached for module j, i.e. $i_{q,j} = i_{max,j}$, balanced DC-bus module voltages in the series connection imposes:

$$p_{dc,i} = p_{dc,1} = p_{dc,2} \cdots = p_{dc,avg} = p_{dc,j} = \eta_j u_{q,max,j} i_{q,max,j} \tag{3.30}$$

Hence, the maximum average current which still allows for balanced DC-bus voltages is a function of the system parameter variations and turbine operating point. Eq. 3.31 is obtained by introducing Eq. 3.30 into Eq. 3.29.

$$i_{q,max} = \frac{1}{N} \left(\sum_{i=1}^{N} \frac{\eta_i \eta_j \left(-r_{s,j} i_{max,j} + n_{mech} \psi_j\right)}{(-r_{s,i} i_{q,i} + n_{mech} \psi_i)} \cdot i_{max,j} \right) \tag{3.31}$$

Where $i_{q,i}$ relates to $i_{max,j}$ according to Eq. 3.32, which is obtained by equating $p_{dc,i}$=$p_{dc,j}$).

$$i_{q,i} = \frac{n_{mech}\psi_i - \sqrt{(n_{mech}\psi_i)^2 - 4 r_{s,i} \eta_i (\eta_j (-r_{s,j} i_{max,j} + n_{mech} \psi_j) i_{max,j})}}{2 r_{s,i} \eta_i} \tag{3.32}$$

Finally, Eq. 3.31 can be simplified to Eq. 3.33, assuming negligible losses. This expression gives an estimate of the maximum, main current reference, and hence the required turbine torque derating.

$$i_{q,ref} = \frac{1}{N} \cdot \left(\sum_{i \neq j}^{N} \left(\frac{\psi_j i_{max,j}}{\psi_i} \right) + i_{max,j} \right) \tag{3.33}$$

3.5 Modular converter fault analysis

3.5.1 Overview of faults affecting a modular converter in a wind turbine

The most important fault scenarios for a modular converter in a wind turbine can be divided into three groups based on where in the system the fault occurs, Fig. 3.8:

1. Component fault within a module.
2. Grid fault.
3. Failure of a converter unit.

In this section, the faults are assessed, and those identified as special for the modular, series connected converter are analyzed in detail.

Component faults within a module

The internal component faults in converters have been extensively studied [95–99]. The handling of such component faults should result in protective actions by the VSC-hardware protection circuits, leading to a trip of the affected converter unit. Consequently, these faults are not special for the series connected converter, and are assumed to result in converter unit failures. One exception is the short circuit of a stator segment coil which cannot be mitigated in the series connection (see Appendix C.2).

Grid faults

With the increasing amount of wind power in the power system, grid codes (e.g. [100]) have been introduced to ensure safe operation of the grid. AC grid low voltage ride through (LVRT) is often considered to be the most important

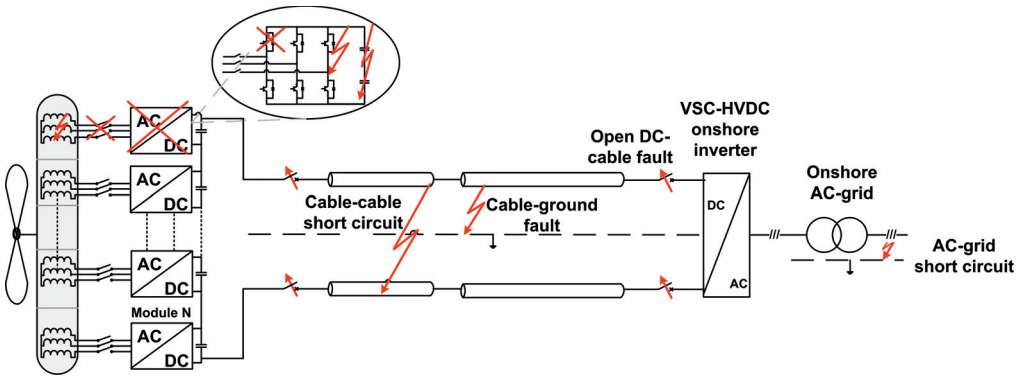

Figure 3.8: Illustration of electric faults which will affect the modular, series connected converter.

requirement in the grid codes. Naturally, LVRT has therefore been studied extensively, both for single turbines [49, 50], and wind farms connected to the grid via VSC-HVDC [101]. For a wind turbine connected to a DC-distribution grid, the LVRT will be comparable to that of a VSC-HVDC.

DC-grid short circuit results in a high fault current which builds up much faster than an AC-short circuit current [102, 103]. A fast circuit breaker is required for protection of the components. Additionally, the breaker must be able to interrupt the current without zero voltage/current crossing. Different circuit breaker solutions have been proposed during recent years, such as the solid-state circuit breaker [104, 105], emitter turn-off thyristor-based circuit breaker [106, 107] and hybrid circuit breakers [108]. None are commercially available at the present stage. Inductive chokes/filters are often proposed to limit the fault current rise time [109], as an addition to the fast acting DC-circuit breaker.

The grid faults are external faults, which are not assumed to affect the internal states of the modular converter, and are therefore not pursued further.

Converter unit faults

The converter unit faults can be divided into two groups.

1. Faults which lead to loss of the entire module, for instance overcurrent trip or component faults.
2. Partial faults, which require a derating of the module, e.g. cooling problems in one module.

Both types of faults require special attention in the case of series connected modules. The analyses are presented in Sec. 3.5.2 and Sec. 3.5.3 respectively.

3.5.2 Converter unit trip with redundant operation

Redundancy is crucial in a modular system to enhance the system availability. Without redundancy, the increased component count will result in decreased overall system reliability. Additionally, there must be a reliable fail-to-safe transition to be able to exploit the redundancy. For the series connected converter, the fail-to-safe transition for a converter unit trip is obtained by utilizing the capacitor bank to provide a current path, and the freewheeling diodes to clamp the capacitor voltage to zero, Fig. 3.4. The mechanism allows for the complete elimination of the faulty module from the converter without stopping the turbine.

The response to a converter unit fault is qualitatively described by four phases:

1. *The converter unit trips, fail mode:* The freewheeling diodes are reverse biased and stator segment current blocked. The DC-link current flows in the bus capacitor. The DC voltage increases for the functioning modules.

2. *Passive rectifier, safe mode:* The DC current discharges the bus capacitor until the diodes become forward biased, and power is fed the to the bus, via the freewheeling diodes. The remaining N-1 healthy modules continue normal operation.

3. *Fault elimination: redundant mode/reconnection:* Based on fault monitoring, it may be possible to decide if the converter trip was falsely triggered, or it was an actual fault. In the first case, the module is reconnected. In the latter, the module is eliminated. This bypass is achieved by opening the AC breaker between the stator segment and the converter unit, Fig. 3.4. The DC-link current discharges the capacitor bank to 0 V, and the diodes clamp the bus voltage preventing a negative overvoltage.

4. *Completion of bypass:* In the case of a bypass, the mechanical connector on the DC side of the bus is closed, eliminating the faulty module from the series connection.

The different phases (1-3) are analyzed in the following sections, including the principles and requirements for reconnecting a falsely tripped module. It is assumed that the fault detection and necessary changes in the control strategy for the N-1 healthy modules are solved by the turbine control.

Control system additions for redundancy are addressed in Sec. 4.4.1 and transient analysis in Sec. 5.4.1.

Switch requirements for redundant operation

The redundancy in the series connected converter requires overrating of the semiconductor repetitive blocking voltages, U_{DR}. This is because the total turbine output voltage is externally controlled and is equal before and after the module fault. The total required blocking voltage for a switch in a converter unit is found by including a redundancy term in Eq. 3.8:

$$U_{DR} = U_{DC,i} \cdot (1 + \frac{y}{100}) \cdot \frac{N+z}{N} \tag{3.34}$$

z is the number of redundant modules. y is a safety factor.

The same voltage overrating will have to be included in the phase-to-phase insulation in the stator segments and the segment to ground insulation. The redundant operating requires a derating of the turbine power proportional to the number of lost modules. The upside of the overrating is that the component stress will be reduced during normal operation.

Quasi-steady-state analysis of the passive rectifier operation following a converter unit trip

The quasi-steady state after the trip is characterized by a partially discharged DC bus, and the VSC functioning as passive rectifier. Speed and turbine power determine the exact operating DC voltage for the unit. Due to the harmonic components injected in the faulty module's electromagnetic torque by the diode bridge, the system should only be in this state temporarily, before eliminating the fault.

The DC voltage of a tripped converter unit is described by two cases based on the turbine operating point and the diode bridge conduction mode:

1. Discontinuous conduction - no-load
2. 120° conduction - normal operation

Continuous conduction mode occurs only for DC currents much higher than the nominal current of this system, and is not considered, Sec. 3.4.1.

After a unit trip, the total DC-link voltage, $u_{dc,tot}$=N$u_{dc,n}$ remains the same. Consequently, the DC-link current, $i_{dc,link}$ is given by Eq. 3.35, where $p_{dc,h}$ is the power from one of the N-1 healthy modules.

$$i_{dc,link} = \frac{p_{dc,h}}{Nu_{dc,n} - u_{dc,f}}(N-1) \tag{3.35}$$

Subscript h refers to a fully functional (healthy) module, and f to a faulty module, $u_{dc,tot} = N \cdot u_{dc,n} = N$.

The approximation as current source is depending on a relatively large number of modules. Thus, the larger the number of N, the more the current will be decided by the healthy modules, and not influenced by the faulty unit operation point.

Discontinuous conduction mode of diode bridge

In no load operation, the relation between the DC-bus voltage and generator induced voltage is given by Eq. 3.15.

$$u_{dc,f} = \frac{\sqrt{3}}{2} n_{mech} u_n$$

Diode bridge normal conduction mode

In the normal conduction mode, the relation between the tripped converter unit DC-side voltage and turbine speed is given by Eq. 3.12, repeated here:

$$u_{dc,f} = n_{mech}\left(\frac{3\sqrt{3}}{2\pi}u_n - \frac{9}{8\pi}x_s i_{dc,link}\right)$$

$i_{dc,link}$ is given by the approximation of the $N-1$ modules as a current source according to Eq. 3.35. By combining Eq. 3.35 and Eq. 3.12, the tripped converter DC voltage is obtained as a function of the healthy module power and turbine speed, Eq. 3.36.

$$\begin{gathered} u_{dc,f}^2 - u_{dc,f}\left(Nu_{dc,n} + A\right) + \left(A \cdot Nu_{dc,n} - B \cdot p_{dc,h}(Nu_{dc,n} - 1)\right) = 0, \\ A = \frac{3\sqrt{3}}{2\pi} n_{mech} u_n, B = \frac{9}{8\pi} n_{mech} x_s \end{gathered} \tag{3.36}$$

Eq. 3.36 is valid from from no load up to nominal conditions. The calculated, tripped converter unit DC-bus voltage is shown in Fig. 3.9 for speed of 0.3 pu-1.0 pu and power from 0.1 to 1.0 pu.

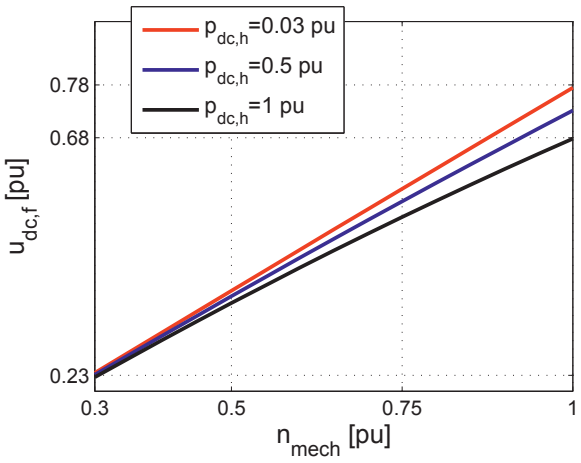

Figure 3.9: $u_{dc,f}$ **as function of speed of the turbine for** $120°$ **plotted for different outputs from the healthy modules. (N=9).**

Estimated DC-bus voltage of a tripped converter unit

By referring to Fig. 3.9, it is verified that the most important factor deciding the DC-bus voltage of the tripped module, and hence also overvoltage in the healthy modules, is the rotor speed. The healthy-module power results in smaller, but still noticeable variations, approximately 10 % of the rated DC voltage at nominal speed. This gives an indication on how accurate the approximation of the $N-1$ healthy modules as current source is: If the operating point is altered, the faulty-module bus voltage will respond, and the DC-link current will depend on this response. The less variation in the DC-bus voltage due to change in turbine power, the more accurate the DC-current source approximation.

The increase in healthy module bus voltage, $u_{dc,h}$, following from a converter unit trip at low speed is comparable to a complete bypass. As a consequence, the voltage rating of the semiconductors, U_{DR}, should take this into account to guarantee fail-to-safe operation and avoid excessive overvoltage stress of the healthy module switches, Eq 3.37.

$$U_{DR} = U_{DC} \cdot (1 + \frac{y}{100}) \cdot \frac{N + z + 1}{N} \tag{3.37}$$

z is the number of redundant modules. y is a safety factor.

Reconnection of tripped converter unit during turbine operation

In the case of a falsely triggered converter unit trip, it is possible to reconnect this module directly, without shutting down if the converter unit DC bus is not discharged completely. The reconnection of a tripped unit demands that care is taken to avoid inrush currents and loss of control. Flux weakening control (see Sec. 4.2.4) can be utilized to reduce the effective stator voltage, so that the depth of modulation, u_{cmd}, defined by Eq. 3.38, is limited.

$$u_{cmd} = \frac{u_{s,i}}{u_{dc,i}} \tag{3.38}$$

Imposing $u_{cmd} = 1.0$ ensures control reserve during reconnection and prevents inrush currents. Flux weakening is achieved by the injection of d-axis current. From Sec. 3.4, it is known that a module in the series connection is required to provide power for DC-bus voltage support. The q-axis does current therefore need to be controlled so that the module power is equal before and after reconnection. Summarized, the current references for reconnection of the faulty module should comply with the following demands:

- $u_{cmd} \simeq 1.0$
- $u_{dc,reconnect} \simeq u_{dc,f}$

$u_{dc,reconnect}$ *is the module voltage during reconnection.*

D-axis current reference: A depth of modulation equal to 1.0 is introduced, which results in the following relation, Eq. 3.39:

$$\begin{aligned} &u_{s,f} \leq u_{dc,f} \Rightarrow u_{q,f}^2 + u_{d,f}^2 \leq u_{dc,f}^2 \\ &\Rightarrow \left((-r_s i_{d,f} + n_{mech} x_s i_{q,f})^2 + (-r_s i_{q,f} - n_{mech}(x_s i_{d,f} - \psi))^2 \right) \leq u_{dc,f}^2 \end{aligned} \tag{3.39}$$

Solving Eq. 3.39 for $i_{d,f}$ results in Eq. 3.40, (subscript i is omitted for simplicity, $u_{dc,f}$ is given by Eq. 3.12):

$$\begin{aligned} i_{d,f} &= \frac{n_{mech}^2 x_s \psi}{r_s^2 + (n_{mech} x_s)^2} - \frac{\sqrt{C}}{r_s^2 + (n_{mech} x_s)^2} \\ C &= -2 r_s^2 n_{mech}^2 x_s^2 i_{q,f}^2 - r_s^4 i_{q,f}^2 \\ &\quad + 2 r_s^3 i_{q,f} n_{mech} \psi + r_s^2 u_{dc,f}^2 - r_s^2 n_{mech}^2 \psi^2 \\ &\quad - n_{mech}^4 x_s^4 i_{q,f}^2 + 2 n_{mech}^3 x_s^2 r_s i_{q,f} \psi + n_{mech}^2 x_s^2 u_{dc,f}^2 \end{aligned} \tag{3.40}$$

By neglecting stator losses, Eq. 3.40 can be simplified into Eq. 3.41:

$$i_{d,f} = \frac{n_{mech}\psi - \sqrt{u_{dc,f}^2 - (n_{mech}x_s i_{q,f})^2}}{n_{mech}x_s} \tag{3.41}$$

In Fig. 3.10(a), the flux weakening current required for reconnection is given as a function of the DC-side current and rotor shaft speed. The required $i_{d,f}$ depends more on the system power than the turbine speed.

Q-axis current reference: The q-axis current, $i_{q,f}$, which preserves the DC-bus voltage during reconnection is estimated from Eq. 3.42, assuming no losses.

$$\begin{aligned} &\Rightarrow i_{q,f}\psi_i n_{mech} = u_{dc,f} i_{dc,link} \\ &\Rightarrow i_{q,f} = \frac{u_{dc,f} i_{dc,link}}{\psi_i n_{mech}} \end{aligned} \tag{3.42}$$

The application of Eq. 3.42 will result in a minor underestimate of $i_{q,f}$. Hence, the DC voltage will decrease slightly, and the depth of modulation will increase. A more accurate value for $i_{q,f}$ is obtained by compensating for the stator losses, Eq. 3.43.

$$\begin{aligned} i_{q,f} &= \frac{u_{dc,f} i_{dc}}{\psi n_{mech}} + \frac{r_s i_{s,f}^2}{n_{mech}\psi} \\ \Rightarrow i_{q,ref} &= i_{q,f} + \frac{r_s i_{s,f}^2}{n_{mech}\psi} \end{aligned} \tag{3.43}$$

During reconnection, priority is given to the q-axis current, to avoid collapse of the DC-bus voltage.

In Fig. 3.10(b), the safe-operation area for reconnection is illustrated. The module current, i_s, is restricted to 1.0 pu in steady state, and a transient limit of 1.2 pu. Reconnection at nominal speed and module power results in a too high overall current requirement. A compromise must be made, and the d-axis current should be limited according to Eq. 3.44.

$$i_{q,f}^2 + i_{d,f}^2 \leq i_{s,max} \Rightarrow i_{d,f} \leq \sqrt{i_{s,max}^2 - i_{q,f}^2} \tag{3.44}$$

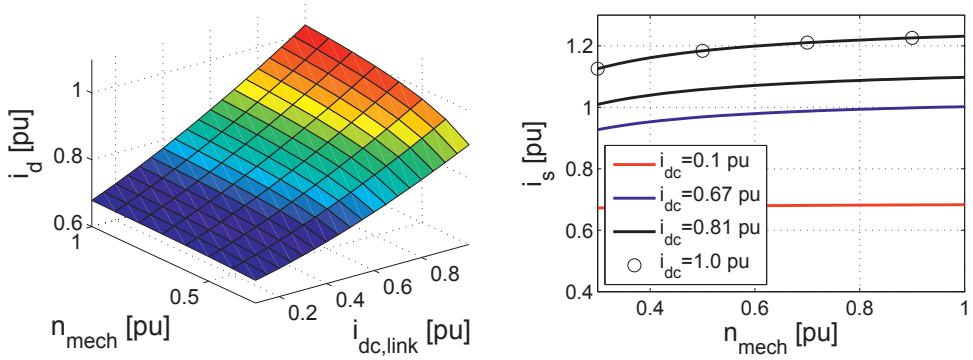

(a) (b)

Figure 3.10: Estimated current for linear operation of the converter unit during reconnection. a) D-axis current. b) Corresponding, total stator current as function of turbine speed. Plotted for different DC-link currents.

Direct and quadrature axis currents during module fault

An option for reconnection of the module which results in a lower current requirement than identified in Fig. 3.10(b), is to apply d- and q-axis current reference equal to the fault current components, ($i_{q,f}$ $i_{d,f}$). Since $u_{dc,f}$ is the same as above, the q-axis current is according to Eq. 3.43. By introducing Eq. 3.35 for $i_{dc,link}$, Eq. 3.45 is obtained.

$$i_{q,f} = \frac{p_{dc,h}(N-1)}{Nu_{dc,n} - u_{dc,f}} \cdot \frac{u_{dc,f}}{n_{mech}} \tag{3.45}$$

For a diode rectifier, the first harmonic of the AC current is given by Eq. 3.46.

$$i_{s,f} = \frac{3\sqrt{3}}{2\pi} i_{dc,link} \tag{3.46}$$

The d-axis current in the passive rectifier is obtained by combining Eq. 3.45 with Eq. 3.46 into Eq. 3.47.

$$i_{d,f} = \frac{p_{dc,h}(N-1)}{(Nu_{dc,n} - u_{dc,f})} \sqrt{\left(\frac{3\sqrt{3}}{2\pi}\right)^2 - \left(\frac{u_{dc,f}}{n_{mech}}\right)^2} \tag{3.47}$$

where $u_{dc,f}$ is given by Eq. 3.12.

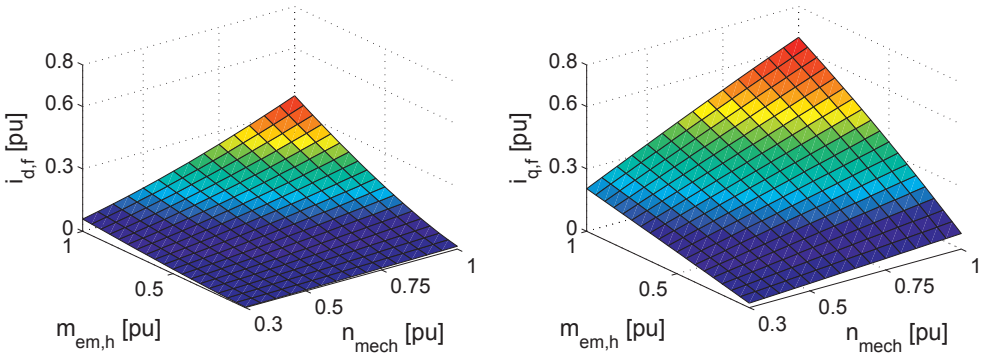

Figure 3.11: Currents after a converter unit trip as function of rotor speed and torque in the functioning modules. a) Absolute value of d-axis current b) q-axis current

The d- and q-axis currents are illustrated in Fig. 3.11(a) and Fig. 3.11(b) respectively, as function of healthy module torque and turbine speed.

The difference between the two options for d-axis current set point are compared by simulation in Sec. 5.4.1.

Redundant operation physical limit

Fail-to-safe operation for a converter unit trip requires that the DC-link current is larger than zero. If the DC-link current is negative (i.e. motor mode), the capacitor of the tripped module is charged instead of discharged. Motor mode introduces therefore a serious threat to the components in the case of a trip. A DC chopper should be included in each module to protect the converter against overvoltages in this case. This modular chopper solution results in higher energy dissipation capability requirements than one high voltage chopper, but provides better module protection, see Appendix E.4. The mechanical bypass connector in Fig. 3.4 is necessary to provide safe operation in redundant mode. In Appendix E.6, the resulting overvoltage from not including the additional protection is demonstrated by simulation.

3.5.3 Mitigation of overheating in a module

Minimal turbine derating strategy for fault-tolerant operation

Continuous condition monitoring may increase system reliability and availability by allowing preventive actions when an abnormal situation occurs [23]. An example of such a situation for the modular converter system is overheating in a single segment due to problems with the module cooling system. In order to avoid causing damage to the module, the AC current should be reduced in the problematic module, i.e. reducing losses. In order to reduce the AC current in a single module, there are two feasible strategies for the series connected converter:

1. Reduce the power in all modules equally, to comply with the faulty module current limit.
2. Reduce the DC-bus voltage of the faulty module, to comply with the faulty module current limit.

The principles are explained based on the power balance in one module, Eq. 3.48: A reduction in $i_{q,f}$ demands DC-side power reduction, since the speed, and hence stator q-axis voltage, u_q is not changed. The DC power can be reduced in two ways: either by reducing $i_{dc,link}$ (strategy 1) or the faulty module DC-bus voltage $u_{dc,f}$ (strategy 2)

$$\begin{aligned} p_{dc} &= i_{dc,i} \cdot u_{dc,i} \\ &= u_{q,f} \cdot i_{q,f} \\ \Rightarrow u_{dc,f} &= \frac{u_{q,f}}{i_{q,f}} i_{dc,link} \end{aligned} \tag{3.48}$$

Strategy 1 will result in unnecessary deloading of the healthy modules, but equal voltage stress in all modules. Strategy 2 allows the N-1 healthy modules to provide full power, but requires increased voltage rating of the components. Strategy 2 results in reduced DC-link current at the nominal operating point, since the power in the healthy modules is at maximum and the bus voltages increases, Eq. 3.49.

$$i_{dc,link} = \frac{p_{dc,h}}{u_{dc,h}} \tag{3.49}$$

Identification of the physical and operational limits for independent module derating

It is beneficial to decrease the output power in the faulty module, $p_{dc,f}$ until the total turbine derating exceeds the nominal power of one module. This ensures that

the converter system is exploited fully during a situation that requires deloading of a single module.

This limit is operational, and given by Eq. 3.50.

$$\left(\sum_{i=1}^{N-1} p_{dc,i,red}\right) + p_{dc,f} = \sum_{i=1}^{N-1} p_{dc,h} = p_{dc,lim} \tag{3.50}$$

$p_{dc,i,red}$ *is reduced power of a healthy module.*

When this limit is reached, the faulty module should be disconnected to continue in redundant N-1 operation.

The second constraint on the individual deloading mode is the lower limit for DC-bus module voltage. This limit is physical, and occurs when the VSC starts to behave as uncontrolled diode rectifier. By neglecting the commutation voltage drop in Eq. 3.12, this occurs when:

$$u_{dc,lim} \simeq \frac{3\sqrt{3}u_n}{2\pi} n_{mech} \simeq 0.826 u_n n_{mech} \tag{3.51}$$

$u_{dc,lim}$ *is the minimum DC-bus voltage which can be controlled without flux weakening.*

For the series connection in current limit operation, flux weakening cannot contribute to a lower, steady-state stator-segment voltage. The reason is that maximum power for a given current is obtained with zero d-axis current. Since the reason for reducing the DC voltage is to maximize the turbine power output under constrained module current, flux weakening would be counter productive.

There is a close relation between high turbine speed and high loading of a wind turbine. The following discussion of the power limit is therefore focused on nominal speed. For a lower speed, the identified limits for individual deloading will be less restrictive.

The DC-voltage reference, $u_{dc,f,ref}$, is given by Eq. 3.52 for individual deloading of the fault module.

$$u_{dc,f,ref} = \frac{n_{mech}\psi_i \cdot (i_q - \Delta i_{q,f})}{i_{dc,link}} \tag{3.52}$$

$\Delta i_{q,f}$ *is the required current reduction in the faulty module.*

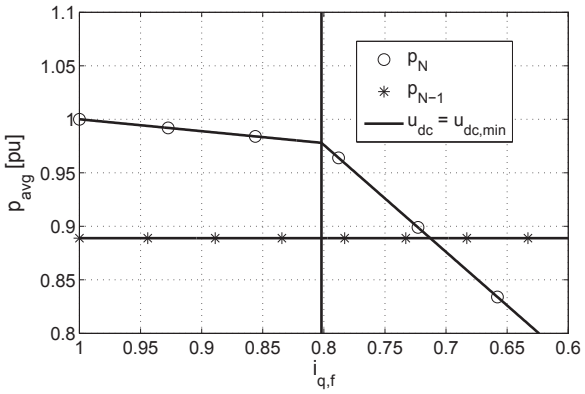

Figure 3.12: Average power output from the series connected converter with reduced functionality in one converter at nominal speed, as function of reduction in current limitation from the nominal value.

The total turbine output power is given by Eq. 3.53:

$$p_{dc,tot} = \sum_{i=1}^{N-1} p_{dc,i} + (u_{dc,f} \cdot i_{dc,link}) \tag{3.53}$$

Eq. 3.52 and Eq. 3.53 are valid until the voltage reference equals $u_{dc,lim}$. After this point, further module stress reduction is achieved by a general torque reduction for the entire turbine. The torque reference, $m_{em,ref}$, for this mode, is described by Eq. 3.54.

$$m_{em,ref} = \psi_i \left(\Delta i_{q,f,udc0} + i_{q,f,lim}\right) \tag{3.54}$$

In Eq. 3.54, $\Delta i_{q,f,udc0}$ is the AC-current reduction obtained by decreasing the module DC-bus voltage. $i_{q,f,lim}$ is the current limit for the faulty module.

The total turbine output power is now given by Eq. 3.55.

$$p_{dc,tot} = (N-1) n_{mech} \cdot m_{em,ref} + (n_{mech} \cdot i_{q,f,lim} \psi_i) \tag{3.55}$$

The limit at which it is more beneficial to disconnect the faulty module than continue to reduce the torque is found by combining Eq. 3.52 to Eq. 3.55.

This results in Eq. 3.56, which gives the turbine torque, $m_{em,ref,lim}$.

$$\begin{aligned} p_{lim} &= (N-1)\cdot n_{mech} m_{em,ref,lim} + n_{mech}(m_{em,ref,lim} - i_{q,f,lim}\psi_i) \\ &\Rightarrow N \cdot n_{mech} m_{em,ref,lim} = p_{lim} + n_{mech} i_{q,f,lim}\psi_i \\ &\Rightarrow m_{em,ref,lim} = \frac{p_{dc,lim} + n_{mech} i_{q,f,lim}\psi_i}{N \cdot n_{mech}} \end{aligned} \tag{3.56}$$

$p_{dc,lim}$ is given by Eq. 3.50.

In Fig. 3.12, the different deloading operation regions are illustrated for N=9 and nominal turbine speed. In the figure, p_N is the maximum output power available to the grid as function of current limit reduction in a converter unit. p_{N-1} is redundant operation with one module disconnected. The vertical line indicates when the lower bus-voltage, $u_{dc,min}$, is reached. This crossover occurs when $i_{q,f}$ is 0.80 pu. Before this point, the module current deloading is achieved via reduction of $u_{dc,f,ref}$. After the point, further reduction is achieved through the main torque reference. When p_N crosses p_{N-1}, it is more beneficial to disconnect the faulty module than continue to reduce the overall system torque. At this point, the current in the faulty module is reduced by 33 %.

3.6 Summary of the system description

In this chapter, the proposed generator/converter solution suitable for a HVDC transformerless wind turbine is presented. The impact of the generator technology on the converter topology design is highlighted. The converter topology proposed for the system is a modular, series connected converter consisting of N 3-phase voltage source converter units. One of the most important requirements imposed by the generator design is balanced converter unit DC-bus voltages. This voltage balance is required for optimal utilization of the insulation system. The analyzes, results and conclusions presented throughout this thesis are general, for any number of modules. For examples with numerical values, N=9 modules is used.

A mathematical representation of the generator seen from the converter control perspective is presented. The modeling approach allows for the machine to be represented by N virtual 3-phase PMSGs with common speed.

The consequence of variable module parameters is analyzed in this chapter. A DC-bus voltage imbalance between the converter units due to parameter deviation is identified. An analytic expression relating the parameter deviations to the turbine power capture is developed, under the constraint of balanced DC-bus voltages.

The last part of this chapter is focused on identifying the possibilities for implementing fault tolerance. Emphasis is on obtaining fail-to-safe and redundant operation. Two types of module faults are investigated: 1) A converter unit trip. Fail-to-safe transition and direct, continued redundant operation have been identified for the system when operated as generator. If the system is operated as motor, additional protection circuits (DC choppers) are required for the protection of the system. 2) The possibility for individual deloading of a module in the case of overtemperature. This results in minimum total turbine derating. Expressions for the physical and operational limits for this mode are developed.

4 Control System Synthesis for the Modular Series Connected Converter

The modular control system synthesis presented in this chapter is developed based on the system constraints from the previous chapter. Each module controller is based on a vector current control, with necessary additions for a series connected converter. The control system is synthesized so that all changes of control strategy is implemented in the main turbine control. Finally, fault-tolerant control additions are included.

4.1 Requirements for the control system imposed by the series connection

The following system characteristics identified in the previous chapter will influence the control system synthesis:

- *DC-bus voltage, steady-state deviations:* A DC-bus voltage control system which compensates the DC-bus voltage deviations is required for optimal utilization of the generator insulation system. The DC-bus voltage control should be robust with respect to parameter variations.
- *Magnetic decoupling:* There is negligible magnetic coupling between the stator segments, and each module can be treated as an independent 3-phase generator.
- *Modularity:* Both the generator and converter are modular. To exploit this feature, the control system should be designed for modular operation.
- *Fault tolerance:* Redundant mode and independent deloading control should be feasible to implement with the synthesized control structure. This requires the DC-bus voltage to be robust with respect to the operating point.

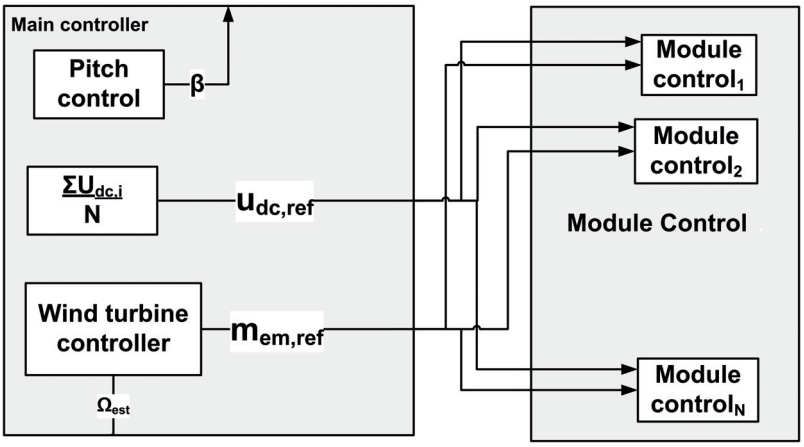

Figure 4.1: Overview of the control system for Concept 4. The turbine controller units are in the main control, and the converter unit control blocks in the modules.

The control proposed for Concept 4 (Sec. 2.3) [36] is used as the starting point, Fig. 4.1. It is based on a cascaded control: The torque reference is generated by the wind turbine power control, and distributed to the module vector current control. The DC-bus voltage reference is distributed to the DC-bus voltage controllers. Control of the DC-bus voltages is handled in the respective modules.

The (simplified) control flow for the control of one converter unit in the series connection is illustrated in Fig. 4.2. All coordination between the module controllers is handled at the turbine control level.

In the following sections, the different control blocks are treated in detail. The discussion starts with the innermost loop, and moves out in the cascade.

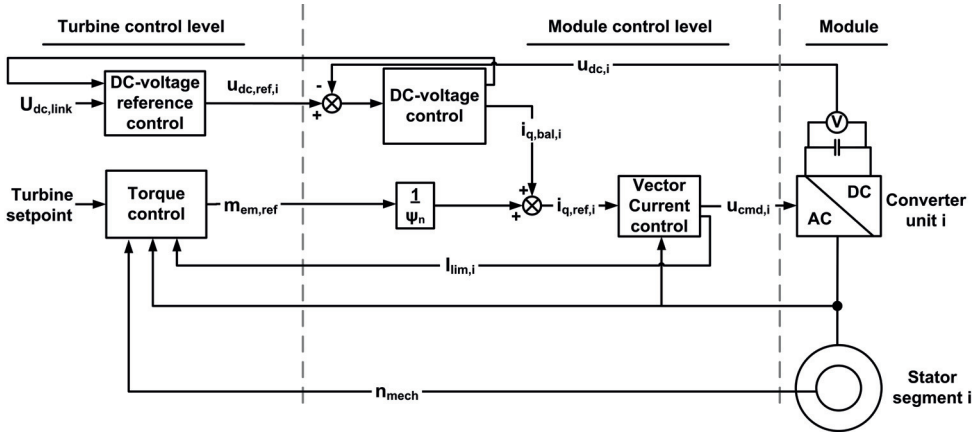

Figure 4.2: Simplified control system illustrating the main blocks for the control of a module.

4.2 Module control

A detailed view of the control system of each module is presented in Fig. 4.3. The main blocks are addressed in this section.

4.2.1 Vector current control

The current control can be implemented independently for each module, due to the magnetic decoupling between the stator segments. A common current control structure is the vector current control [79, 80]. The q-axis current is used for torque control, and the d-axis current for magnetization. The synthesis of the current control for module i is based on the stator segment i's dynamic equation in the dq-plane, Eq. 4.1 (extracted from Eq. 3.6).

$$\begin{aligned} u_{d,i} &= -(r_s i_{d,i} + l_s \cdot \frac{di_{d,i}}{dt}) + n_{mech} x_s i_{q,i} \\ u_{q,i} &= -(r_s i_{q,i} + l_s \cdot \frac{di_{q,i}}{dt}) - (n_{mech} x_s i_{d,i} - \psi_i) \end{aligned} \tag{4.1}$$

$u_{dq,i}$ are the stator segment output voltages, $i_{dq,i}$ module currents, r_s winding resistance and l_s stator segment synchronous inductance.

The current control is implemented as a two-variable control system. A compensation of the cross-coupling terms in Eq. 4.1 is included, Eq. 4.2.

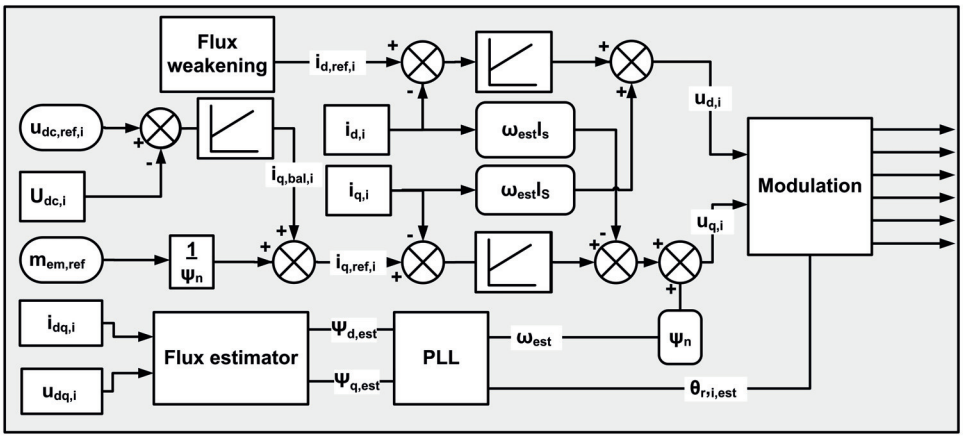

Figure 4.3: Block diagram for the analyzed control system for each module, illustrated with flux estimation for rotor position tracking.

$$
\begin{aligned}
u_{d,i}(s) &= \frac{K_p(1+sT_i)}{sT_i} + n_{mech} x_s i_{q,i} \\
u_{q,i}(s) &= \frac{K_p(1+sT_i)}{sT_i} - (n_{mech} x_s i_{d,i} - \psi_i)
\end{aligned}
\tag{4.2}
$$

$u_{dq,i}$ are the current control output voltage references. K_p is the proportional gain, T_i is the integral time constant.

The PI control parameters are tuned using the modulus optimum criterion [79]. The stator electric pole is canceled with the integral time-constant, and the proportional gain is used for crossover frequency tuning, according to Eq. 4.3.

$$
\begin{aligned}
K_p &= u_{dc,n} \frac{l_s}{T_{pe}} \\
T_i &= \frac{l_s}{r_s}
\end{aligned}
\tag{4.3}
$$

In Eq. 4.3, $u_{dc,n}$ nominal DC-bus module voltage, and T_{pe} is the sum of the estimated delays in the control loop.

The detailed tuning of the current control is given in Appendix B.1 and the simulation of a step response to the current controllers for the modular series connected converter is presented in Appendix E.1. The behavior is found to be identical to that of a single converter system.

4.2.2 Current-control mode small-signal stability of the series connected DC-bus voltages

In the current-control mode[1], the quasi-steady-state characteristic of a converter unit is equivalent to a constant power load (CPL) [110]. That is, for small disturbances, the current control maintains the AC current, and hence the AC power constant. On the DC side of the converter unit, this causes the current to increase if the voltage is reduced, and vice verse. The CPL behavior can be modeled by a negative resistance. This behavior is known to cause stability problems in power systems.

For the series connected converter, the situation is slightly different: Since the turbine output voltage is externally controlled, the negative resistance behavior of the converter units is not causing problems for the DC-distribution grid voltage stability. However, the internal distribution of DC-bus voltages in the series connection is affected by the CPL behavior of the converter units. This is demonstrated by the qualitative small-signal-stability analysis in the following paragraphs. The stability is analyzed for perturbations in the DC-bus voltage for a converter unit. Since a turbine may enter motor mode during for instance acceleration phases, both generator- and motor-modes are considered.

The small-signal analysis refers to the constant power curves in Fig. 4.4. The curves are drawn as a function of module DC-bus-voltage and -current, for both motor and generator operation mode of a module. For a given power, the DC-bus voltage is inversely proportional to the absolute value of the DC current. In the figure, the horizontal lines mark the voltage operation limits, and the vertical lines mark the current limits.

Generator mode stability

The power balance for a converter unit i, can be expressed by Eq. 4.4 for generator operation . Since the converter unit is current controlled, the AC power, $p_{ac,i}$, is constant in quasi-steady-state for the turbine:

$$\begin{aligned} u_{dc,i} i_{dc,i} &= p_{ac,i} \\ i_{dc,i} &= i_{c,i} + i_{dc,link} \\ u_{dc,i} \cdot (i_{c,i} + i_{dc,link}) &= p_{ac,i} \end{aligned} \tag{4.4}$$

[1]current-control mode is used throughout the thesis to describe the operation of the series connected converter units without DC-bus voltage control.

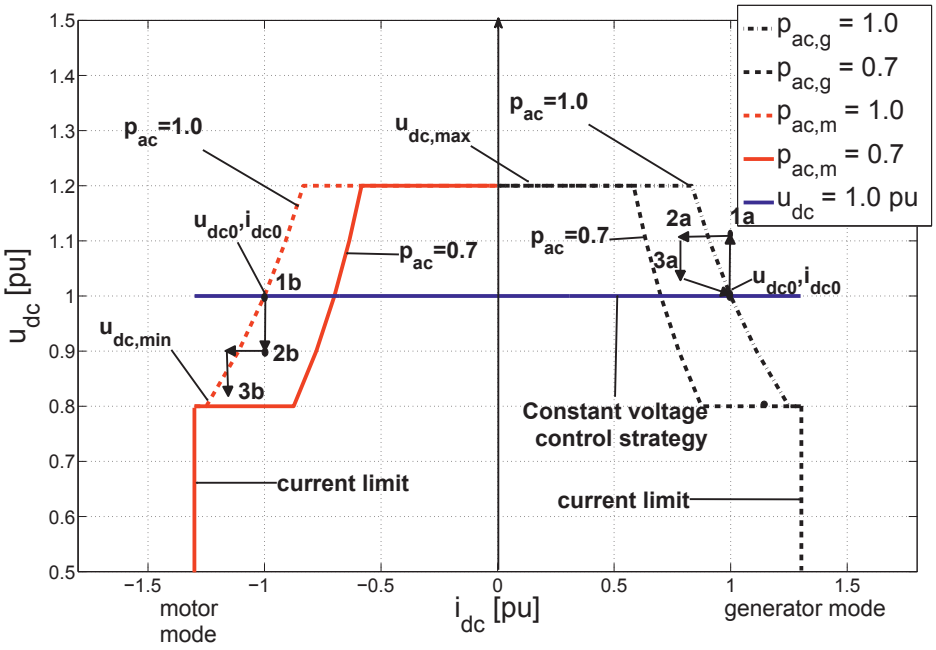

Figure 4.4: Constant power load for small-signal stability analysis. $u_{dc,i}$-$i_{dc,i}$ curve for generator (*subscript - g*, positive module DC current, i_{dc}) and motor mode (*subscript - m*, negative i_{dc}).

$i_{dc,link}$ *is the constant DC-grid current, common for all modules.* Introducing Eq. 4.5 for the capacitor current $i_{c,i}$:

$$i_{c,i} = c_i \frac{du_{dc,i}}{dt} \tag{4.5}$$

This results in Eq. 4.6, which gives the relation between the converter unit voltage and power, and the DC-link current.

$$u_{dc,i} \cdot (i_{dc,link} + c_i \frac{du_{dc,i}}{dt}) = p_{ac,i} \tag{4.6}$$

Eq. 4.6 is used to interpret the constant power curves of the generator mode, starting from steady-state (u_{dc0}, i_{dc0}) in Fig. 4.4: If a small positive disturbance $\Delta u_{dc,i}$ is introduced to the DC-bus voltage (Point 1a in the figure), this leads to a reduction in the converter DC current, i_{dc}, (2a). Since the DC-link current is maintained constant, the difference in current will have to come from the capacitor current, i_c. This will discharge the capacitor, and result in a reduction in the bus voltage (negative $\dot{u}_{dc,i}$) (3a). Since the bus voltage is reduced, the converter

current increases again. Eventually, the DC-bus voltage converges towards a stable operating point. This stable point is given by the steady-state expression for the DC-bus voltage distribution, Eq. 3.24 in Sec. 3.4.2. Hence, it is independent of the transient states. For a small negative disturbance in the bus voltage, the reasoning is equal, but opposite.

In the generator mode, the constant power load operation of the modules does not introduce stability issues for the series connection. Control of the DC-bus voltages is therefore not necessary to guarantee stability in generator mode.

Motor mode stability

The motor mode of the series connection is analyzed using the same reasoning as for the generator mode. The direction of power flow is changed, and hence also the DC-link current. By introducing the opposite main current direction in Eq. 4.6, Eq. 4.7 is obtained for the motor mode:

$$\begin{aligned} u_{dc,i} \cdot (i_{dc,link} - i_{c,i}) &= -p_{ac,i} \\ u_{dc,i} \cdot (i_{dc,link} - c_i \frac{du_{dc,i}}{dt}) &= -p_{ac,i} \end{aligned} \tag{4.7}$$

The stability is analyzed by relating Eq. 4.7 to the constant power curve for motor mode in Fig. 4.4: In motor mode, a small, negative voltage disturbance (Point 1b) results in an increase in converter DC current (2b). Since the DC-link current is constant, the additional current will be drawn from the bus capacitor. Consequently, there is a negative rate of change in capacitor voltage (3b), eventually decreasing the DC-bus voltage. This again causes the converter unit DC current to increase, and the situation is escalating. Hence, the negative resistance behaves as positive feedback, which reinforces the initial disturbance. This behavior will continue until one of the converter units in the series connection reaches the voltage level for which the VSC starts behaving as an uncontrolled rectifier. At this point, the control of the converter unit is lost.

Hence, the internal distribution of the DC-bus voltages of the series connected converter is instable in the motor mode. Moreover, this instability cannot be improved with an external, stable DC-link voltage. This is in contrast to single-module systems, and parallel systems, where external control can be utilized to improve the stability. For the series connection, control of the converter unit DC-bus voltages is necessary to guarantee stability.

The small-signal stability for DC-bus voltages is verified by the simulation results presented in Sec. 5.2.2.

4.2.3 DC-bus voltage control

The demand for DC-bus voltage control is introduced by motor mode instability, Sec. 4.2.2, and deviating DC-bus voltages for optimal utilization of the insulation system, Sec. 3.1.2. In order to respect the system modularity, a DC-bus voltage control is included for each module. In the following paragraphs, the synthesis of the DC-bus PI controller is presented and a linearized model of the DC-voltage control loop is developed for tuning and robustness analysis. The tuning is selected based on the following criteria:

1. No overshoot in the controlled DC voltages for minimization of oscillations.
2. Parameter variation robustness.
3. Operating condition robustness.

The DC-voltage control is in cascade with the q-axis current control. A rule of thumb for cascaded controllers is that the inner loop should have approximately one decade larger bandwidth than the outer loop. This approach is found to provide a satisfactory controller response, as will be demonstrated in the following.

Linearized model for the DC-bus voltage control analysis

The relation between the q-axis current and DC-bus voltage of a module is given by Eq. 4.8, by assuming that $i_{dc,link}$ can be regarded as a disturbance (the subscript i is omitted in this paragraph).

$$\begin{aligned} p_{ac} = p_{dc} \Rightarrow & u_q \cdot i_q = u_{dc} \cdot i_{dc} = u_{dc}\left(c\frac{du_{dc}}{dt} + i_{dc,link}\right) \\ \Rightarrow & \frac{du_{dc}}{dt} = \frac{u_q \cdot i_q}{c \cdot u_{dc}} - \frac{i_{dc,link}}{c} \end{aligned} \tag{4.8}$$

p_{dc} is power measured at the DC rails of a converter unit.c is the DC-bus capacitance

The set of equations describing the relation between the current reference, $i_{q,ref}$ and module bus voltage, u_{dc} is given in Eq. 4.9.

$$\begin{aligned} u_q &= -\frac{u_q}{T_{pe}} + \frac{K_{cm}K_p}{T_{pe}}x_r - \frac{K_{cm}K_p}{T_{pe}}i_q + \frac{K_{cm}K_p}{T_{pe}}i_{q,ref} \\ \dot{i_q} &= -\frac{1}{l_s}u_q - \frac{r_s}{l_s}i_q + \frac{n_{mech}\psi}{l_s} \\ \dot{x_r} &= -\frac{1}{T_i}i_q + \frac{1}{T_i}i_{q,ref} \\ \dot{u_{dc}} &= \frac{u_q i_q}{c \cdot u_{dc}} + \frac{i_{dc,link}}{c} \end{aligned} \tag{4.9}$$

where x_r represents the internal integrator variable of the PI-current control. K_{cm} is the voltage ratio between the input and output voltage of the converter in per unit.

Linearizing Eq. 4.9 around the operating point (i_{q0},u_{q0},u_{dc0}) results in Eq. 4.10:

$$\begin{pmatrix} \dot{\Delta u_q} \\ \dot{\Delta i_q} \\ \dot{\Delta x_r} \\ \dot{\Delta u_{dc}} \end{pmatrix} = \begin{pmatrix} \frac{-1}{T_{pe}} & -\frac{K_{cm}\cdot K_p}{T_{pe}} & \frac{K_{cm}\cdot K_p}{T_{pe}} & 0 \\ \frac{-1}{l_s} & -\frac{r_s}{l_s} & 0 & 0 \\ 0 & \frac{-1}{T_i} & 0 & 0 \\ \frac{i_{q0}}{c\cdot u_{dc0}} & \frac{u_{q0}}{c\cdot u_{dc0}} & 0 & \frac{-u_{q0}\cdot i_{q0}}{c\cdot u_{dc0}^2} \end{pmatrix} \cdot \begin{pmatrix} \Delta u_q \\ \Delta i_q \\ \Delta x_r \\ \Delta u_{dc} \end{pmatrix} + \begin{pmatrix} \frac{K_{cm}\cdot K_p}{T_{pe}} \\ 0 \\ \frac{1}{T_i} \\ 0 \end{pmatrix} \cdot i_{q,ref} \tag{4.10}$$

Subscript 0 indicates that the constant is derived from a linearization of the corresponding state variable.

The transfer function from $i_{q,ref,i}$(s) to Δu_{dc}(s) based on Eq. 4.10 is Eq. 4.11.

$$H_{iq,udc}(s) = \frac{K_p u_{dc0}\,(sT_i + 1)}{(sc_{pu}{u_{dc0}}^2 + u_{q0}i_{q0})} \cdot \frac{(-u_{q0} + si_{q0}l_s + i_{q0}r_s)}{(s^3T_i l_s T_{pe} + s^2T_i r_s T_{pe} + s^2T_i l_s - sT_i K_p + sT_i r_s - K_p)} \tag{4.11}$$

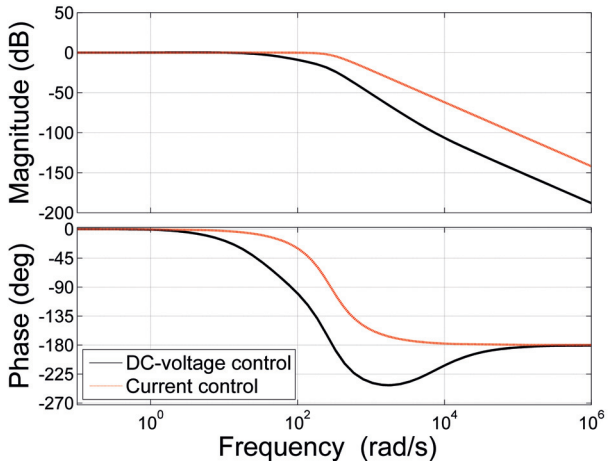

Figure 4.5: Closed loop frequency response for the DC-bus voltage control and current control.

The open loop DC-bus voltage control, $H_{udc,o}(s)$ is given by Eq. 4.12:

$$H_{udc,o}(s) = H_{dc,pi}(s)H_{iq,udc}(s) \cdot u_{dc,ref} \tag{4.12}$$

$H_{dc,pi}(s)$ is the transfer function for the PI control

Proposed tuning for the DC-voltage control loop

The closed loop DC-voltage control frequency response is shown in Fig. 4.5, together with the current control loop for comparison. This controller tuning (parameters in Table 4.1), results in an acceptable phase margin for all operating conditions and parameter variations, as will be demonstrated in the next paragraph. The simulation results of the dynamic responses are presented in Sec. 5.2.3.

Table 4.1: DC-voltage control parameters

Parameter	*Value*
$K_{p,dc}$	2.13 pu
$T_{i,dc}$	0.64 [s]

Robustness analysis of the DC-bus voltage balancing

The modular control system requires that each module control can function independent of the other modules for variable conditions. This demands that the proposed tuning provides sufficient stability margins for variable turbine operating points and module parameter deviations. The robustness of the control is assessed by replacing the nominal value of the parameter "X" according to Eq. 4.13 in Eq. 4.12.

$$X = X_n \pm \Delta X \tag{4.13}$$

The analyses are conducted for different DC-bus voltage and capacitor values. Variations in stator-resistance and -inductance do not affect the stability margins, Appendix B.3. The following analyses are conducted for a turbine speed of 0.3 (i.e., start-up conditions) and 1.0 pu.

DC-bus voltage variations: The controller stability margins with $n_{mech} = 0.3$ are investigated for variations between 23 % and 130 % of the nominal DC-bus voltage, Fig. 4.6(a). A converter unit DC voltage of 0.23 pu is the theoretical minimum bus voltage which can occur in a tripped converter unit according to Sec. 3.5.2. A stable DC-voltage control at this point is required for controlled reconnection of a falsely tripped module. The high voltage (1.30 pu) corresponds to redundant mode with two out of nine modules disconnected. The frequency responses show acceptable stability margins (phase margin larger than 45°) for all bus voltages. The minimum phase margin identified is 58°, for u_{dc}=0.23.

In Fig. 4.6(b), the frequency response for nominal speed is presented. A DC voltage of 0.83 pu is introduced as the lower limit, which corresponds to the limit for individual deloading operation, Sec. 3.5.3. The results show satisfactory stability margins (approximately 50° for $u_{dc} = 0.83$), and the control system is sufficiently robust with respect to different bus voltages.

Different bus capacitances: In Fig. 4.6(c) and Fig. 4.6(d), the frequency responses for capacitor size values from 75 % to 125 % of the nominal are presented. The two plots are for start-up and nominal speed respectively. The worst case concerning phase margin is for 75 % at nominal speed and light load, Fig. 4.6(d). At 0 dB, the phase margin is 48°, which is marginally above the normally prescribed 45°. Hence, the proposed controller tuning is sufficiently robust with respect to variations in the capacitance. As a result, partial faults in the bus capacitor banks in each unit can be tolerated.

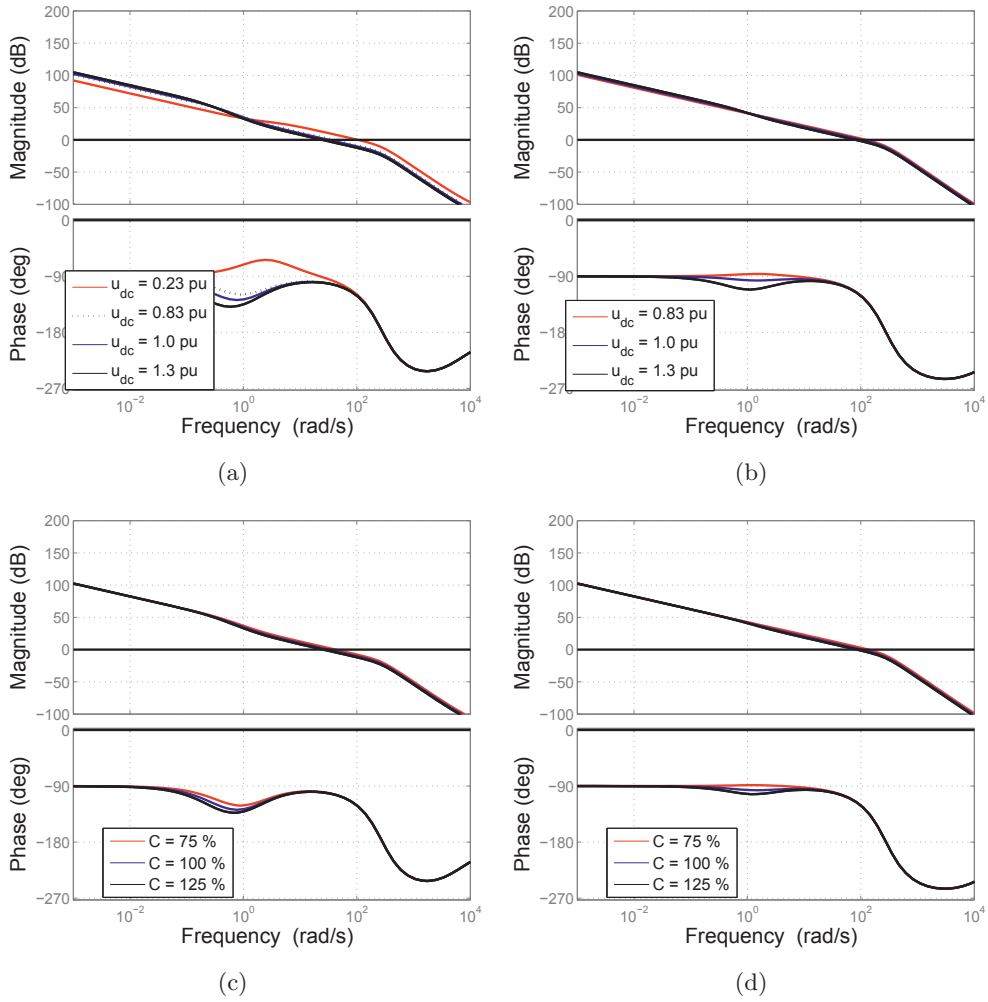

Figure 4.6: Frequency response of open loop control for different parameters. a) Variable DC voltage, n_{mech} = 0.3 pu b) Variable DC voltage, n_{mech} = 1.0 pu c) Variable bus capacitor, n_{mech} = 0.3 pu d) Variable bus capacitor, n_{mech} = 1.0 pu.

4.2.4 Flux weakening control

Flux weakening control is normally utilized to extend the operating speed range of the motor drives, for constant power and reduced torque [111]. There are also examples of the utilization for implementing loss minimization strategies [80,112]. For wind turbines, constant overspeed is not commonly used, since this results in high mechanical stress on the turbine. However, transients such as wind gusts or sudden loss of load can result in temporary speed increase. To enhance the transient performance under such transients, flux weakening is introduced in each

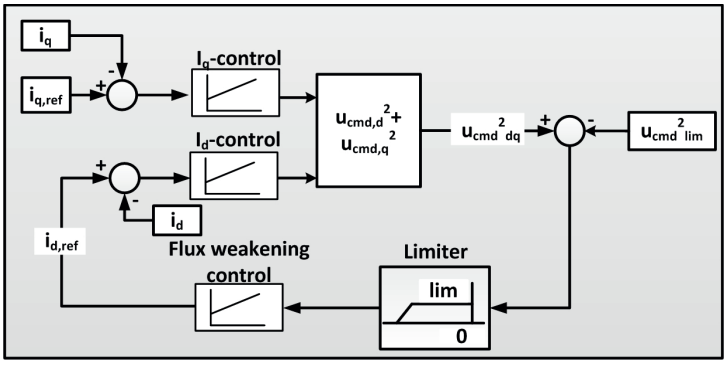

Figure 4.7: Block scheme of the implemented flux weakening control in each module controller.

module controller. The flux weakening reduces the apparent stator voltages to within the converter unit limits, and therefore prevents limitation of the current control output. Flux weakening control is achieved through injection of a d-axis current working opposite of the stator flux linkage. This reduces the resulting q-axis voltage and therefore the total output voltage, Eq. 4.14:

$$\begin{aligned} u_{d,i} &= -r_s i_{d,i} + n_{mech} x_s i_{q,i} \\ u_{q,i} &= -r_s i_{q,i} - n_{mech}(x_s i_{d,i} - \psi_i) \end{aligned} \tag{4.14}$$

An independent flux weakening control for each module ensures equal behavior around nominal operation, independent of stator segment flux linkage differences.

During flux weakening operation, the q-axis current is limited to comply with module current constraints, according to Eq. 4.15.

$$i_{q,i} \leq \sqrt{i_{s,max}^2 - i_{d,i}^2} \tag{4.15}$$

The flux weakening control implemented in this thesis, Fig. 4.7, is proposed in [113]. It is based on feedback of the square sum of the depth of modulation for the d- and q-axis, $u_{cmd,dq}^2$. This is compared to the modulation limit, $u_{cmd,lim}^2$. The controller is active when the compared value is larger than zero. Tuning and frequency response of the flux weakening controller are given in Appendix B.2.

Maximum steady-state flux weakening for the AF-IL PMSG in per unit is given by Eq. 4.16. The module current and synchronous reactance are the two limiting factors.

$$x_s \cdot i_{d,max} = x_s \cdot i_{s,n} = 0.33 \tag{4.16}$$

$i_{s,n}$ is the module nominal current.

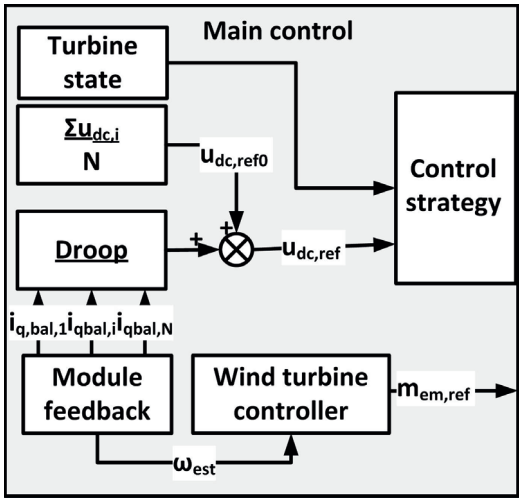

Figure 4.8: Main turbine control structure, allowing for different control strategies and fault mitigation.

4.3 Turbine main control system

The block scheme for the turbine main control is given in Fig. 4.8, and the details are presented in the next sections.

4.3.1 Power capture control

There are several control strategies proposed for the operation of variable speed wind turbines. Maximum power point tracking (MPPT) has received most attention [114–116] but there are also other strategies. These strategies implement active power control and grid support [117, 118]. It is outside the scope of this work to engage in a discussion of the advantages and disadvantages of the different methods. However, the dynamic performance of the modular series connected converter should be analyzed for realistic control strategies. An MPPT based on indirect speed control (ISC) [116] is implemented in this thesis. The ISC offers a simple, but robust control system.

The turbine operation is divided into four regions, Fig. 4.9(a). Region I is constant, minimum speed, which is normally set to avoid interference with the tower resonance frequencies. Region II is the MPPT region. In region III, the turbine has reached nominal speed, but not rated power. In this mode, the turbine speed is limited to 1.0 pu by the torque control. In the last region, IV, the turbine is in power control mode, i.e., the pitch controller constrains the power capture to the rated value. The block diagram for the ISC is presented in Fig. 4.9(b). The

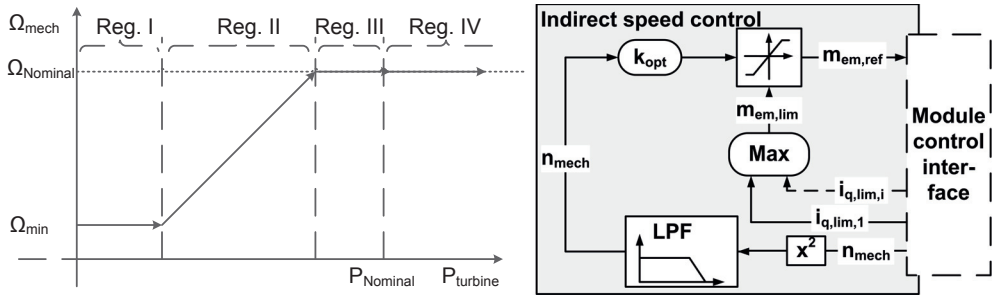

Figure 4.9: a) Control regions for the indirect speed control (ISC). b) Block diagram for the ISC.

tuning of the ISC is presented in Appendix B.4.

Module current limit: If the current limit is reached in some of the modules before the main current limit for the turbine is reached, the torque reference should be reduced. This reduction is implemented by taking the absolute value of the current limitation (i.e. the difference between the current required to control the module-torque and -DC-bus voltage, and the maximum current in the module) from the module controllers as input to the power capture control. The module that is subject to the strongest limitation will decide the reduction in the turbine torque reference. This feedback allows the turbine control to take into account the additional power required for DC-bus voltage control, and limit the torque reference as described in Sec. 3.4.3. Hence, a sufficient control reserve for DC-bus voltage control is obtained for all normal operating conditions.

4.3.2 DC-voltage reference set-point control

The DC-bus voltage set point used in the module controllers, $u_{dc,ref0}$, should be selected so that

$$Nu_{dc,ref0} = u_{dc,tot} \tag{4.17}$$

The DC-voltage set point can be generated in two different ways:

- Based on voltage measurement of the entire DC-link of the series connection, divided by N.
- Based on the average of the voltage measurements obtained in each module.

The first option imposes the following steady state relation between the controlled DC-bus voltages and the DC-bus voltage set point, Eq. 4.18:

$$\begin{aligned} \frac{u_{dc,tot}}{N} \quad & -u_{dc,1} = \quad 0 \\ \vdots \quad & \vdots \quad \vdots \\ \vdots \quad & \vdots \quad \vdots \\ \frac{u_{dc,tot}}{N} \quad & -u_{dc,N} = \quad 0 \\ \Rightarrow N\frac{u_{dc,tot}}{N} \quad & -\sum_{i=1}^{N} u_{dc,i} = 0 \end{aligned} \tag{4.18}$$

where

$$\sum_{i=1}^{N} u_{dc,i} = u_{dc,tot}$$

For an ideal system, Eq. 4.18 is always fulfilled. However, in reality there may be errors in the measurements. Hence, the relation between the actual DC-bus voltage and the measured value in each module is given as:

$$u_{dc,i} = u_{dc,i,msr} \pm \Delta u_{dc,i} \tag{4.19}$$

Inserting Eq. 4.19 into Eq. 4.18 and rearranging yields Eq. 4.20.

$$\begin{aligned} u_{dc,tot} - \sum_{i=1}^{N} u_{dc,i,msr} \mp \sum_{i=1}^{N} \Delta u_{dc,i} = 0 \\ \Rightarrow u_{dc,tot} - u_{dc,tot} \mp \sum_{i=1}^{N} \Delta u_{dc,i} = 0 \end{aligned} \tag{4.20}$$

If Eq. 4.20 is not fulfilled, at least one DC-bus voltage control will not be able to obtain zero DC-voltage regulation error. This will cause this the integrator of this control to wind up, resulting in instability in the control system.

To solve this stability problem, the average of the measured DC-bus voltages at the modules is introduced as the DC-bus voltage reference set point, $u_{dc,ref0}$, Eq. 4.21.

$$u_{dc,ref0} = H_{filt,0}(s)\frac{1}{N}\sum_{i=1}^{N} u_{dc,i} \tag{4.21}$$

By applying the average measured voltage as set point, eventual measurement errors will be compensated for in the reference according to Eq. 4.22:

$$\frac{1}{N}\sum_{i=1}^{N} u_{dc,i} - \sum_{i=1}^{N}(u_{dc,i,msr} \pm \Delta u_{dc,i}) = 0 \tag{4.22}$$

The equality in Eq. 4.22 is always fulfilled in steady state and the measurement errors will not causes stability problems for the DC-bus voltage control system.

Therefore, the average of the modules measured DC-bus voltages, Eq. 4.21, is used for the DC-bus voltage set point in this thesis.

4.3.3 Torque-based DC-voltage droop control

The necessity of the droop control

The degrees of freedom in the DC-voltage control system is $N-1$ when the DC-link voltage is set by a central converter. The result is that $N-1$ DC-bus voltage controllers would result in correct voltages for all N converter units. The N^{th} bus voltage would be given by Eq. 4.23.

$$u_{dc,tot} = \sum_{i=1}^{N} u_{dc,i} \Rightarrow u_{dc,j} = u_{dc,tot} - \sum_{i\neq j}^{N} u_{dc,i} \tag{4.23}$$

However, modularity in the control system requires that all module controllers are equal. Since this results in N DC-bus voltage controllers, the system becomes overdetermined. For an overdetermined system, there exists many solutions to the defined control problem, which in this case is to balance the DC-bus voltages. The possible solutions are different combinations of outputs from the DC-bus voltage controllers, which all fulfill the required DC-bus voltage balance control. This can be explained by referring to the module power balance in Eq. 3.9 (repeated below), which gives the fundamental relation between the DC-bus voltages and module output powers.

$$u_{dc,i} = \frac{p_{dc,i}}{p_{tot}} \cdot u_{dc,tot}$$

Since the DC-bus voltage balance control task is:

$$u_{dc,1} = u_{dc,2} = ... = u_{dc,N}$$

it is, from Eq. 3.9 required that

$$p_{dc,1} = p_{dc,2} = ... = p_{dc,N} \tag{4.24}$$

Eq. 4.24 does only require that the DC-bus voltage controllers regulate the module power relatively to the total power. The absolute value of the module power and total power is not taken into consideration, and may vary freely as long as the correct output power relation is preserved.

Given ideal control loops, this overdetermined control should not cause problems, since all control responses would be equal. However, each of the DC-bus voltage controllers may have slightly different transient responses. It is the combination of these different DC-bus voltage control responses and the overdetermined control system that causes the problems. The reason is that the DC-bus voltages are coupled, Eq. 4.23. For example, if one fast module control is required to compensate -5 % DC-bus voltage and a slow control $+5$ % DC-bus voltage, the fastest module can also take part in the compensation of the slow module, e.g. the slow fast control may provide $+7.5$ %, and the slow -2.5 %. Thus, the actual turbine torque, $m_{em,turbine}$ will differ from the torque set-point, $m_{em,ref}$, Eq. 4.25,

$$m_{em,turbine} = m_{em,ref} + \frac{1}{N}\sum_{i=1}^{N} i_{q,bal,i}\psi_i \tag{4.25}$$

$m_{em,ref}$ is the turbine control system torque reference output, $i_{q,bal,i}$ is DC-voltage control output of module i.

Since the DC-bus voltage balance control should affect the converter unit DC-voltages only, and not the turbine torque, a load-sharing control is introduced in the next paragraph.

The overdetermined DC-bus voltage control system, without droop control, is illustrated by simulations presented in Sec. 5.2.4. The results demonstrate the effect, that $\sum_{i=1}^{N} i_{q,bal,i}\psi_i \neq 0$.

The torque-based DC-voltage droop control implementation

Traditionally, load sharing in AC grids is implemented by frequency droop control [119]. This droop is a proportional feedback loop based on changes in the grid frequency which results in changes in the power reference set-point. This method

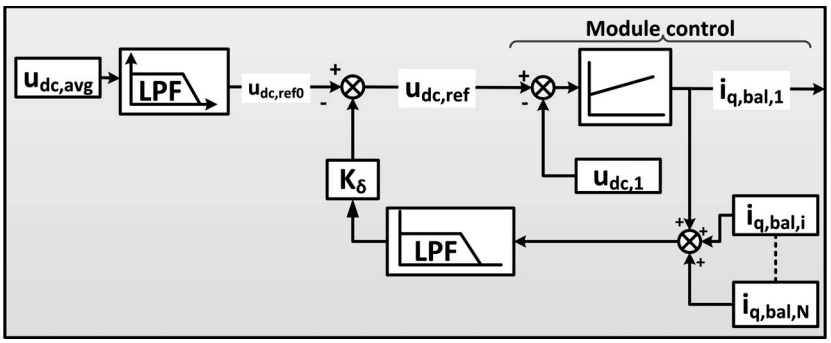

Figure 4.10: Droop control loop including the DC-bus voltage control scheme

ensures stable load sharing, and avoids controllers fighting each other to control the frequency, i.e. an overdetermined control system. In DC grids, there is no frequency to control. The load sharing control has therefore been proposed implemented as a droop based on the DC-grid voltage [120, 121]. This concept can be extended to the control of the series connected converter: Since the common, controllable variable is the turbine torque, the droop is based on the difference between torque set-point and the actual torque. Hence, the control is a *torque-based DC-voltage droop control*.

The torque-based DC-voltage droop control is different from a standard droop control in the way, that it includes multiple inputs from all the modules of the system. Also, it provides a common reference input to all modules. Additionally, the implemented droop ensures that the average torque of all modules is equal to the torque reference, Eq. 4.26.

$$m_{em,ref} = \frac{1}{N}\sum_{i=1}^{N} m_{em,i} = m_{em,turbine} \tag{4.26}$$

The load sharing of the torque-based DC-voltage droop control is achieved by multiplying the sum of output from the modules DC-bus voltage controllers (the last term of Eq. 4.25 when assuming ψ=1.0) with the droop constant. The product is used as feedback to the DC-bus voltage set point, $u_{dc,ref0}$, Eq. 4.27. This addition to the set point is equal for all modules. Consequently, the resulting DC-bus voltage reference, $u_{dc,ref}$, is common for all modules.

$$u_{dc,ref} = u_{dc,ref0} - k_\delta \cdot \left(\sum_{i=1}^{N} i_{q,bal,i}\right) \tag{4.27}$$

In Eq. 4.27, $u_{dc,ref0}$ is the voltage set point according to Eq. 4.21. k_δ is the droop proportional gain, and $u_{dc,ref}$ is the actual reference input to the DC-bus voltage controllers.

In steady state, the DC-bus voltage reference and the DC-bus voltage set point are equal:

$$u_{dc,ref} = u_{dc,ref0}$$

The function of the DC-voltage droop control explained

The function of the droop control is explained as follows (referring to Fig. 4.10): If the sum of DC-bus voltage control outputs ($\sum_{i=1}^{N} i_{q,bal,i}$) is larger than zero, the droop feedback leads to a reduction in the DC-bus voltage reference, $u_{dc,ref}$, compared to the DC-bus voltage set point. This reduction in DC-voltage reference leads again to a corresponding reduction in all the controller outputs since the measured DC-link voltage is constant. As a result, the error between applied torque and torque reference is reduced, and hence the amplitude of the droop feedback. Eventually, the droop term in Eq. 4.27 is brought to zero. When this term equals zero, the droop feedback is eliminated and the DC-voltage control system reaches steady state. In this state, the DC-bus voltage reference equals the DC-bus voltage set point. The reasoning is identical, but with opposite signs, for a negative torque contribution from the controllers, i.e. $\sum_{i=1}^{N} i_{q,bal,i} \leq 0$. The effect of the torque-based DC-voltage droop is demonstrated by the simulations presented in Sec. 5.2.4.

The mathematical proof for the effect of the torque-based DC-voltage droop is given in the next paragraph.

Droop control elimination of controller output

In steady state, the DC-bus voltage control equations, including the droop, are given by Eq. 4.28:

$$\begin{aligned}
u_{dc,ref0} &- k_\delta \textstyle\sum_{i=1}^{N} (i_{q,bal,i}) - & u_{dc,1} &= 0 \\
&\vdots & \vdots & \\
&\vdots & \vdots & \\
u_{dc,ref0} &- k_\delta \textstyle\sum_{i=1}^{N} (i_{q,bal,i}) - & u_{dc,N} &= 0 \\
&\Rightarrow N u_{dc,ref0} - N k_\delta & \sum_{i=1}^{N} (i_{q,bal,i}) - \sum_{i=1}^{N} u_{dc,i} &= 0
\end{aligned} \tag{4.28}$$

In Eq. 4.28, it is assumed that the PI control are able to fulfill their task, i.e.

$u_{dc,ref}$=$u_{dc,i}$. This assumption is valid if Eq. 4.21 is used for the DC-voltage reference set point. In steady state, Eq. 4.21 becomes:

$$u_{dc,ref0} = \frac{1}{N}\sum_{i=1}^{N} u_{dc,i} \tag{4.29}$$

By inserting Eq. 4.29 for $u_{dc,ref0}$ into Eq. 4.28, Eq. 4.30 is obtained:

$$N\frac{1}{N}\sum_{i=1}^{N} u_{dc,i} - Nk_{\delta}\sum_{i=1}^{N}(i_{q,bal,i}) - \sum_{i=1}^{N} u_{dc,i} = 0 \tag{4.30}$$

Since the first and the last term are identical, the droop feedback will fulfill the following relation, Eq. 4.31:

$$\Rightarrow Nk_{\delta}\sum_{i=1}^{N}(i_{q,bal,i}) = 0 \tag{4.31}$$

If both N and k_{δ} are non-zero, $\sum_{i=1}^{N} i_{q,bal,i}$ is zero. Hence, it can be concluded that the torque-based DC-voltage droop control removes the steady state error between the actual applied turbine torque and the torque reference, according to Eq. 4.25.

At the same time, no droop control is a special case, with k_{δ}=0. From Eq. 4.31, it can be seen that if this is the case, $\sum_{i=1}^{N} i_{q,bal,i}$ can take any value.

In Appendix C.1, the demonstration is extended to also include the controller dynamics.

Droop-control parameter analysis

The droop control response can be tuned by two parameters: The droop gain, k_{δ} and the filter time constant of the feedback loop, $T_{filt,\delta}$. In order to investigate the effect of different parameters values, the transfer function from $u_{dc,i}$ to $u_{dc,ref}$ is developed :

$$u_{dc,ref} = u_{dc,ref0} - k_{\delta}H_{filt,\delta}(s)\sum_{i=1}^{N}(i_{q,bal,i}) \tag{4.32}$$

$H_{filt,\delta}$ is the droop feedback filter transfer function

$i_{q,bal,i}$ is described by Eq. 4.33:

$$i_{q,bal,i} = H_{pi,dc}(s)(u_{dc,ref} - u_{dc,i}) \tag{4.33}$$

Eq. 4.34 is obtained by combining Eq. 4.32 and Eq. 4.33:

$$u_{dc,ref} = u_{dc,ref0} - k_\delta H_{filt,\delta}(s) H_{pi,dc}(s) \sum_{i=1}^{N} (u_{dc,ref} - u_{dc,i}) \tag{4.34}$$

If all DC-voltage references are equal, the simplification in Eq. 4.35 can be applied.

$$\sum_{i=1}^{N} u_{dc,ref} = N \cdot u_{dc,ref} \tag{4.35}$$

Inserting Eq. 4.35 in Eq. 4.34 results in Eq. 4.36.

$$\begin{aligned} u_{dc,ref}\,[1 + N k_\delta H_{pi,dc}(s) H_{filt,\delta}(s)] = \\ u_{dc,ref0} + N k_\delta H_{pi,dc}(s) H_{filt,\delta}(s) \cdot u_{dc,avg} \end{aligned} \tag{4.36}$$

Additionally, introducing $u_{dc,ref0} = H_{filt,0}\, u_{dc,avg}$ results in Eq. 4.37:

$$\begin{aligned} u_{dc,ref}\,[1 + N k_\delta H_{pi,dc}(s) H_{filt,\delta}(s)] = \\ H_{filt,0} u_{dc,avg} + N k_\delta H_{pi,dc}(s) H_{filt,\delta}(s) u_{dc,avg} \end{aligned} \tag{4.37}$$

The transfer function of the droop control from $u_{dc,avg}$ to $u_{dc,ref}$ is obtained by rearranging Eq. 4.37:

$$\frac{u_{dc,ref}}{u_{dc,avg}} = \frac{H_{filt,0}(s) + N \cdot k_\delta H_{pi,dc}(s) H_{filt,\delta}(s)}{(1 + N \cdot k_\delta H_{pi,dc}(s) H_{filt,\delta}(s))} \tag{4.38}$$

Filter time constant: The impact of different time constants of the droop feedback filter, $T_{filt,\delta}$, is evaluated for values in the range from 0 (no filter) to 5 s based on the frequency response obtained with Eq. 4.38, Fig. 4.11(a). Setting the droop filter time constant $T_{filt,\delta}$ to zero results in $u_{dc,ref}$ responding to all changes in the voltage measurements feedback. There is a small damping factor, approximately -1 dB for higher frequencies. This corresponds to the droop acting as an additional feedback control with k_δ as gain. An approximately first order response is observed for the filter time constants up to the averaging filter constant,

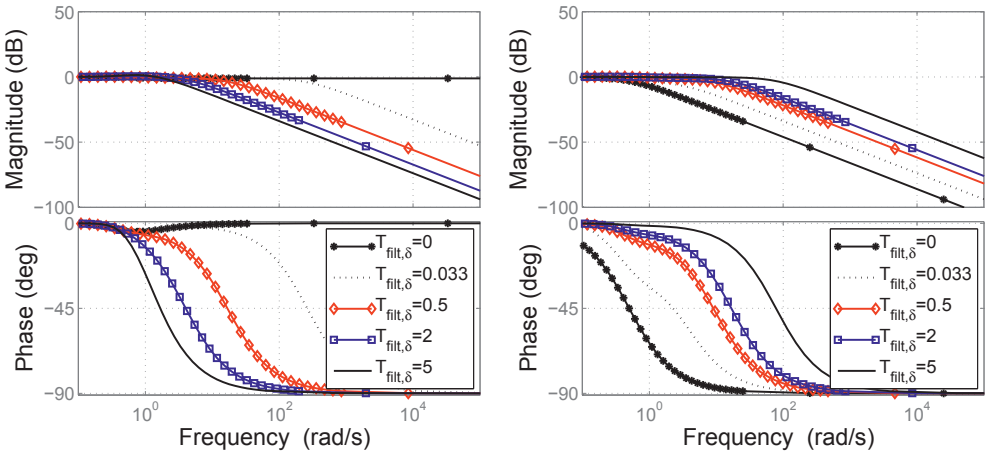

Figure 4.11: a) Frequency response of $u_{dc,ref}$ as function of droop feedback filter time constants, with k_δ=0.1 b) Frequency response of $u_{dc,ref}$ as function of droop gain (k_δ) with $T_{filt,\delta}$=0.5 s

$T_{filt,0}$. The droop filter dominates the frequency response for such values. For droop filter constants higher than $T_{filt,0}$, there is a small resonance top in the frequency response. This will lead to an overshoot in the reference response to DC-bus voltage changes.

The filter time constant is chosen as a trade-off between sensitivity to low frequency noise, response to fast grid voltage changes and avoidance of the overshoot. The following two guidelines can be extracted from the frequency responses:

- $T_{filt,\delta} \ll T_{filt0}$ - to avoid overshoot
- $T_{filt,\delta} \gg T_{\omega_e}$ - to avoid influence by the electric frequency of the generator.

$T_{filt,\delta}$=0.5 is selected for further analysis.

Droop gain: The droop gain frequency response is evaluated for k_δ in the range from 0 to 0.5, Fig. 4.11(b)($T_{filt,\delta}$ is 0.5 s). $k_\delta = 0$ corresponds to open loop, i.e. no droop control. This response is solely decided by the reference set-point filter, $T_{filt,0}$. With a droop gain different from zero, all values were found to result in a stable response, without overshoot. $k_\delta = 0.1$ is selected for further analysis to avoid a noise-sensitive system. The droop steady-state characteristic for k_δ=0.1 is presented in Fig. 4.12

The transient responses for the droop control for different values of k_δ and $T_{filt,\delta}$ is evaluated by simulation in Appendix E.3.

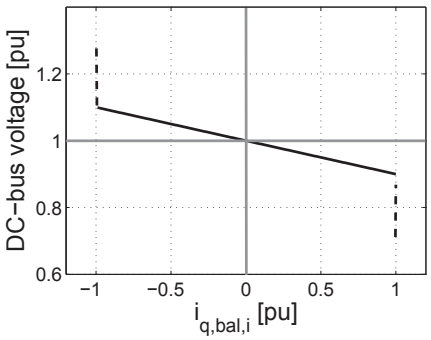

Figure 4.12: Torque-based DC-voltage droop characteristics, with $k_\delta = 0.1$. The dashed lines marks the steady-state current limits.

4.4 Fault-tolerant control additions

4.4.1 DC-bus voltage reference control for redundant operation

In the case of a converter unit trip, the DC-bus voltage references for the remaining modules should compensate for the overshooting voltage from the tripped module according to Eq. 4.39.

$$u_{dc,ref,h}(N-1) + u_{dc,f} = u_{dc,tot} \tag{4.39}$$

$u_{dc,ref,h}$ is the voltage reference input to the healthy modules, $u_{dc,f}$ the measured bus voltage of the faulty unit.

Eq. 4.39 is implemented by the reference modification in Fig. 4.13. The consequence of not implementing this modification is a system, where the healthy modules and the external voltage control will attempt to control the total DC-link voltage.

After the converter chain has stabilized its redundant $N-1$ operation with the faulty module still connected in the converter chain, there are two possible scenarios for the further operation:

1. Reconnecting the tripped module in the case of a false trip.
2. Bypass the tripped module in the case of a true failure.

For a limited time, operation with one diode rectifier and $N-1$ healthy modules can be tolerated. In this intermediate state the control system decides which of the two cases should be the next stage. Simulation results for both cases are given in Sec. 5.4.1.

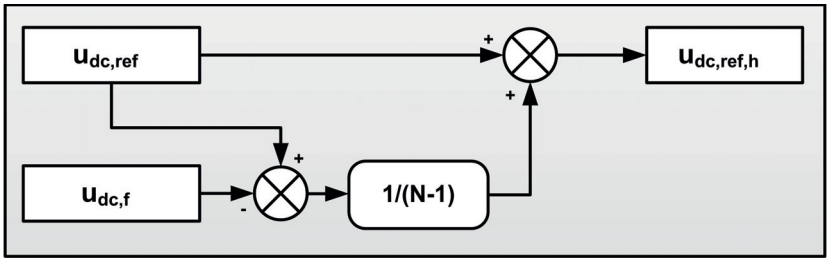

Figure 4.13: DC-voltage reference generation in the case of a tripped converter unit

4.4.2 Individual module deloading control

Individual deloading can be achieved with the DC-bus voltage reference controller shown in Fig. 4.14. The current reference is compared to the reduced current limit of the affected module. The output, $i_{q,ref,adj}$, is used as a reference to the PI control which generates the bus-voltage reference reduction, $\Delta u_{dc,ref,j}$. $\Delta u_{dc,ref,j}$ is subtracted from the average DC-voltage reference. The control output is limited by the passive rectifier mode of the VSC unit, $u_{dc,ref,min}$. Additional deloading after this limit is reached is achieved by reducing the turbine torque reference. If the turbine power output decreases beyond what can be achieved with $N-1$ healthy modules, the faulty module should be disconnected, and the system continues in redundant mode.

The reduction in a faulty module DC-bus voltage reference, $\Delta u_{dc,ref,f}$ from the faulty module is redistributed to the references of the remaining $N-1$ modules, as discussed for redundant mode in the previous section.

4.4.3 Other control strategies feasible with the implemented structure

In this chapter and the previous, it has been emphasized that the preferred control strategy is balanced DC-bus voltages. This will ensure equal stress on the insulation system of the machine, and for normal conditions result in balanced loading of the different parts of the system. It has, however, been demonstrated that sometimes, other control strategies may be more beneficial, e.g. fault tolerance.

The following paragraph lists other feasible control strategies which can be implemented with the same, modular control structure. These are not discussed further, but given as an example of the possibilities offered by this control system[2].

[2]This list of alternative control strategies is the work of Kjell Ljøkelsøy, SINTEF, written for Publication 2, Sec. 1.4.

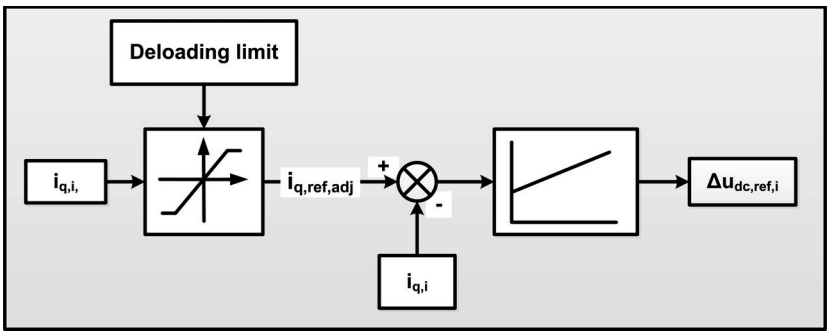

Figure 4.14: Controller structure for individual module deloading by adjustment of the DC-bus voltage control

- *Equal AC current:* The DC voltage is adjusted so that the AC current is equal in all converters. The DC-bus voltage control ensures stability.
- *Temperature balance:* The DC voltage is adjusted to balance different losses in either the converter units or stator segments, to equalize the temperature in the modules.
- *Mechanical stress:* A mechanical model of the generator may be utilized to estimate the forces and deformations in the construction caused by the torque. This can be used to adjust the torque in the modules independently to improve the force distribution and to counteract imbalances in the generator assembly.
- *Oscillation damping:* A large mechanical system like a wind turbine may be exposed to poorly damped mechanical oscillations in the generator itself, the turbine blades, the shaft, or the tower. These oscillations may be detected by strain gauges, displacement measurements, or other methods. The generator control system can be used for active damping by adding frequency components to the reference signals, which makes the generator windings create forces that counter the oscillations.
- *Overvoltage limitation:* The set points for the module DC-bus controllers can be utilized to prevent overvoltages by introducing a strict, upper voltage limit. This operation mode should have priority over the other modes, and is a part of the protection system for the series connected converter.

4.5 Summary of the control synthesis

In this chapter, the synthesis of a control system for the modular, series connected converter in a wind turbine is presented. The emphasis is on designing a robust, modular control system. Safe operation for the converter chain is guaranteed, and constraints imposed by the special generator design are respected. The system is

designed in such a way that different control strategies can be implemented in the turbine main controller, without changing the internal structure of the module controllers.

In Fig. 4.8, a detailed overview of the main controller is given. The structure depends on feedback measurements of the currents, DC-bus voltages and state of the converter units. Fault-tolerant operation modes (redundancy and independent module deloading) can be achieved by individual adjustment of the module DC-bus voltage references. A torque-based DC-voltage droop is introduced in the DC-voltage reference control to avoid an overdetermined system

The module control block diagram is presented in Fig. 4.3. It is based on a standard 3-phase vector current control. A DC-bus voltage control is implemented as a PI control in cascade with the q-axis current control loop. It is demonstrated that it is possible to obtain a set of DC-voltage controller parameters which results in a satisfactory robust control system for all operating conditions.

In addition to the parts addressed here, each module needs a pulse width modulation (PWM) and rotor position tracking. The PWM-method is a choice based on the converter unit topology [122]. In this thesis, a simple Sinusoidal Carrier Based PWM has been implemented. The rotor position relative to the stator segment can be based on position measurement, or a sensorless control (such as [123]).

5 Transient System Analysis Based on Simulations

This chapter presents EMTDC/PSCAD simulations for the transient analysis of the modular series connected converter and segmented generator. The chapter is divided into four sections. In the first section, the simulation model is described. In the second section, the control system blocks are analyzed, and the impact of non-ideal system parameters is evaluated. The third section deals with full system transient behavior for regular turbine operation. In the last section, simulation results for the analysis of fault-tolerant modes are presented.

5.1 Simulation model

The main simulation components and connections are illustrated in Fig. 5.1. A brief description of each module is given in the following.

Generator: Each of the stator segments of the AF-IL PMSG is modeled using one standard 3-phase machine model. (The validity of this approach is discussed in Sec. 3.1.3). The model is a synchronous machine with fixed excitation for emulation of permanent magnet machine behavior [124]. N=3 modules are used for the simulation model, for similarity with the laboratory setup, and reduce computational effort. The three models are interconnected via a first-order dynamic model of the shaft, according to Eq. 5.1.

$$\tau_{mech}\frac{dn_{mech}}{dt} = m_{turbine} - \frac{1}{N}\sum_{i=1}^{N} m_{em,i} \tag{5.1}$$

$m_{turbine}$ is the per unit output torque from the wind turbine blade model, and $m_{em,i}$ is the electro-magnetic torque (in pu) of the i-th stator segment. τ_{mech} is the mechanical time constant, relating the inertia and the rated power of the

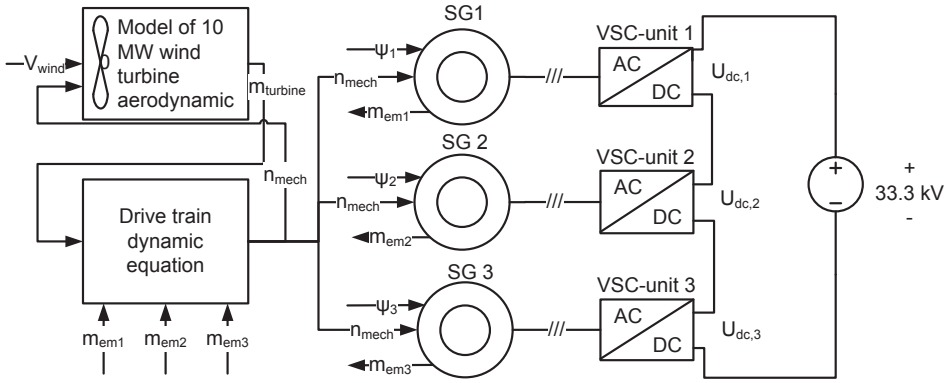

Figure 5.1: Main electrical- and mechanical components and connections in the simulation model of the modular, series connected converter system.

turbine. The output, shaft speed, n_{mech}, serves as input to the stator segment models.

For the fault mode simulations, Sec. 5.4, the model is made of N=9 modules in the place of N=3. The reason for doing so is that the increase in DC-bus voltage in a healthy converter unit with N=3 becomes unrealistically high, i.e. an increase of 50 % in case of a bypassed module. This yields a large differences in voltage ratio for the converter units. The result is that the depth of modulation and dynamic performance of the current controllers is very different from what the system was designed for. With N=9, the DC-bus voltage increase is 12.5 % in the case of a bypass, which is much closer to the design operating point.

Converter unit: The VSC units are implemented using ideal switches to model the semiconductors. The high voltage DC side and the low voltage AC side are split up to overcome numerical problems experienced with floating generator models in PSCAD. A detailed discussion on this issue and the solution is presented in Appendix D.1.

DC link: The DC link is modeled as a stiff DC voltage behind a simple L/R-approximation of the DC cables (parameters are given in Table D.2). The cable impedance results in small response in the voltage at the turbine to different turbine operating points. This model is not sufficiently accurate for investigations of rapid electromagnetic phenomena such as DC-short circuits and high frequency voltages.

Turbine model: The wind turbine model in PSCAD emulates the blade aerodynamic characteristics. It is based on [125, 126]. The parameters of the power-coefficient (C_p) curve are different from those found for a modern 10 MW turbine design, but the response to wind speed and turbine speed is sufficiently realistic for the system investigations presented here.

Control implementation: The control system is implemented using continuous control blocks, and the measurements are considered ideal. Asynchronous communication between the module controllers is emulated by implementing a lag of 0.9 ms (90 % of the PWM frequency) between the reference update of module 1 and module 2 and 3.

Rotor angle: The rotor angles are output from the machine models, i.e. assumed measured.

Initialization: In the simulations, the system is initialized using the voltage source representing the DC link to charge the converter unit DC buses. Hence, bus capacitance variations will result in differences in the initial bus voltage. The initialization is perform before t=0.0 s.

Parameter variations: In some of the simulations results, the system is analyzed with variations in the module parameters, according to Table 5.1.

Table 5.1: Parameter deviations from nominal values in simulation

Module	η_i	r_s	ψ_i
module 1	-2 %	$+25$ %	-5 %
module 2	0 %	-25 %	$+5$ %
module 3	0 %	-25 %	$+5$ %

5.2 Control system blocks transient analysis

In this section, the transient response of the most important blocks in the modular control system is analyzed. The simulation tests are designed to isolate the effect of one controller at the time. Sec. 5.2.1 and Sec. 5.2.2 are focused on the modular series connected converter in current-control mode. The DC-bus voltage control is analyzed in Sec. 5.2.3 and the torque-based DC-voltage droop control is addressed in Sec. 5.2.4. The results of this section are used to demonstrate the basic relations for the system described, and that the control synthesis (Chapter 4), results in a stable, modular control system for the series connected converter.

5.2.1 DC-bus voltages response in current-control mode

In Sec. 3.4.2, the relation between steady-state DC-bus voltages and variations of parameters between modules is identified for current-control mode (Eq. 3.24).

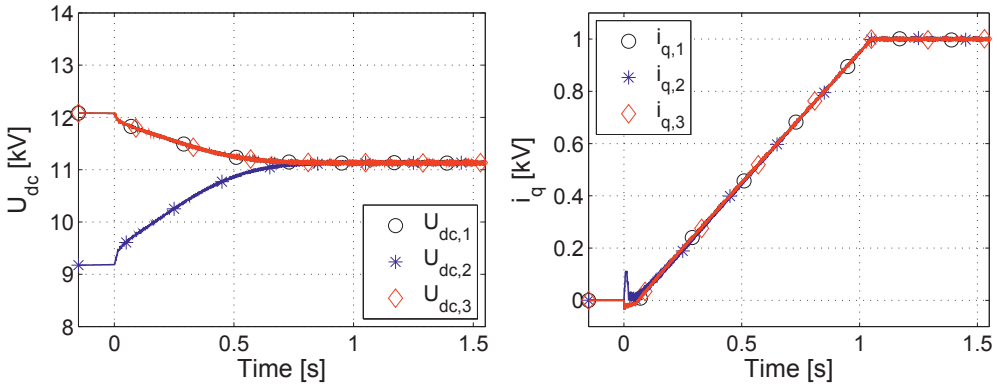

(a) (b)

Figure 5.2: Current-control mode DC-bus voltage response for initially unequal charged modules. a) DC-bus voltages b) q-axis currents.

The interpretation of Eq. 3.24 is, that the DC-bus voltages depends only on parameters that affect the output power from each module. The bus voltages of the converter units are independent of the bus capacitances and previous states, i.e. DC-bus voltages. To demonstrate this independence, the system is simulated with different initial DC-bus voltages and different bus capacitances ($C_2 = 2 \cdot C_{1,3}$). The remaining module parameters are kept equal. The converter units are activated at t=0 s, and the generator speed is 1.0 pu. The simulation results of the DC-bus voltage response in current-control mode are presented in Fig. 5.2(a), with the applied ramp in q-axis current in Fig. 5.2(b). The DC-bus voltages are slowly converging towards a stable state with all bus voltages equal the average voltage, $u_{dc,avg}$. Hence, the simulation results demonstrates that the steady-state DC-voltage distribution is independent of the earlier system states, and bus capacitance. Thus, it is only active power output from the converter units, that will affect the DC-bus voltage balance.

5.2.2 Small-signal stability of DC-bus voltage in current-control mode

The DC-bus voltage small-signal stability in the current-control mode is analyzed qualitatively in Sec. 4.2.2. It is found that the system is instable in motor mode, and stable in generator mode. It is therefore argued that DC-bus voltage control is important for the stability of the modular series connected converter. Simulation results which supports this conclusion are presented in Fig. 5.3(a)-Fig. 5.3(d).

Initially, the system is stable in generation mode with a torque reference of 0.3 pu and n_{mech}=0.5 pu. The torque reference is ramped down to -0.3 pu (motor mode),

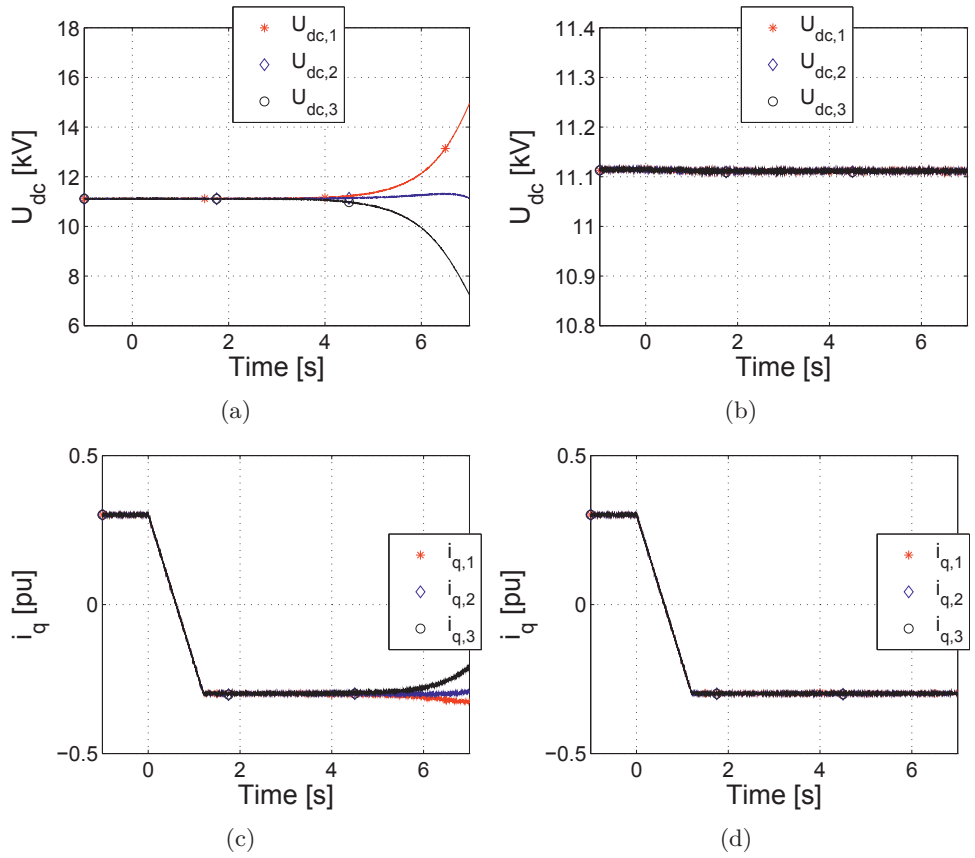

Figure 5.3: Transition from a stable generator mode to motor mode. a) Current control: Instable DC-bus voltages b) DC-voltage control: Stable voltages with DC-bus voltage control. c) Current control: q-axis currents. d) DC-voltage control: q-axis currents.

starting from t=0 s. While the system is in generator mode, the converter unit DC-bus voltages are stable, Fig. 5.3(a). After the transition to motor mode, the bus voltages start to diverge: First slowly, but with escalating response. Eventually, control of the current in converter unit 3 is lost around t=4 s. At this instance, the DC voltage in module 3 is lower than the induced stator segment voltage, and the VSC starts behaving as an uncontrolled rectifier. The same simulation sequence is repeated with the DC-bus voltage control activated, Fig. 5.3(b) and Fig. 5.3(d). The system stability with respect to DC-bus voltage is now preserved for both generator- and motor-mode. Consequently, control of the q-axis currents is preserved, Fig. 5.3(d)

5.2.3 DC-bus voltage control transient responses

The DC-bus voltage control synthesis is based on the assumption that the tuning can be based on the parameters for a single module, and that this design will function with the modules connected in series. In Sec. 4.2.3, it is demonstrated that the DC-bus control, without the droop control, is robust with respect to parameter- and operating-point variations within a single module. The simulation results presented in the following paragraphs are used to verify that the same DC-bus voltage control tuning yields satisfactory performance in the modular series connected converter. The performance requirements are:

- No overshoot in the controlled DC-bus voltages.
- Robust with respect to variations in parameters between modules.
- Rejection of disturbances, such as asynchronous reference update.

DC-bus voltage control step response in a series connection

To avoid overshoot in the controlled DC-bus voltages is important for the control of the modular series connected converter. The reason is, that if the DC-bus voltage of one converter unit overshoots, also the other DC-bus voltages will overshoot. The consequence will be an oscillatory behavior of the DC-bus voltage controllers. A step response is simulated to verify that such oscillations will not occur with the converter units connected in series, Fig. 5.4. The step response in DC-bus voltage reference is achieved by first initiating the system at the operating point set by the MPPT for a wind speed of 6 m/s (turbine torque of 0.2 pu and machine speed of 0.3 pu). At this stage, the DC-bus voltage control is not active. It is assumed that the stator flux linkages results in segment 1 having a decreased excitation of 5 %, while segment 2 and 3 have an increase in excitation of 5 %. This difference in flux linkage results in an initial DC-bus voltage imbalance between the converter units. The difference is in accordance with the theoretical considerations in Sec. 3.4. The difference between module DC-bus voltages and the reference creates a step response when the control is activated at t=0 s. The initial transient of the response charges/discharges the bus capacitors to the reference value. Since the average excitation is not equal to the nominal value, the charging of converter unit 1 requires a higher current compared to the discharging of converter unit 2 and 3. The system reaches steady state after 0.5 s. In steady state, a small, constant balancing current, $i_{q,bal,i}$ is maintained to compensate the constant power difference between the modules. The consequence of this steady-state contribution is that the current limit will be reached in some modules before the others. This will have to be compensated for in the main turbine control, which leads to reduction in the rated turbine torque.

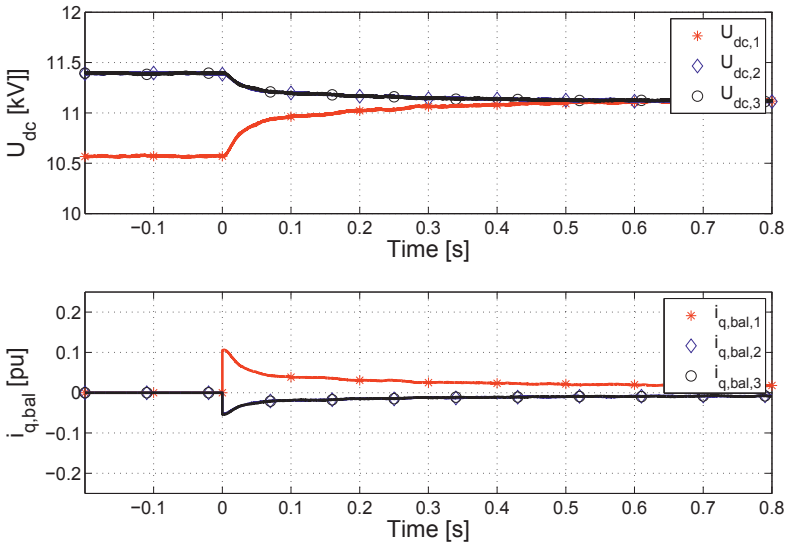

Figure 5.4: DC-bus voltage control response with imbalanced stator segment flux linkage. $m_{em,ref}$=0.2 pu, n_{mech}=0.3 pu. Top to bottom: DC-bus voltage response after the turn on of the voltage control. Output from the module DC-bus voltage controllers.

This is demonstrated theoretically in Sec. 3.4.3. The effect of this module current limit is further investigated in Sec. 5.3.1.

The DC-bus voltage step response demonstrates satisfactory behavior with respect to the avoidance of overshoot in the controlled DC-bus voltages. Additionally, the robustness against variations in stator segment flux linkage is verified.

The simulation of a similar step response, but with variations in DC-bus capacitances, is presented in Appendix E.2. The results demonstrates a satisfactory robustness with respect to variations in bus capacitors. It can therefore be concluded that the control performs satisfactory with respect to variations between module parameters in the series connection.

DC-voltage response to step in torque reference

A modular control system with asynchronous modules requires that the DC-bus voltage control provides disturbance rejection. This disturbance rejection should ensure that the consequences of the asynchronous update of module references are minimized, and that the system operation is not compromised. The robustness against such disturbances is analyzed by simulating a step in the turbine torque reference, Fig. 5.5. Initially, the system is brought to steady state at a speed of 0.3 pu, a torque of 0.1 pu, and the DC-voltage control is activated. The parameter variations are according to Table 5.1. At t=0 s, a step to 0.75 pu is applied. The

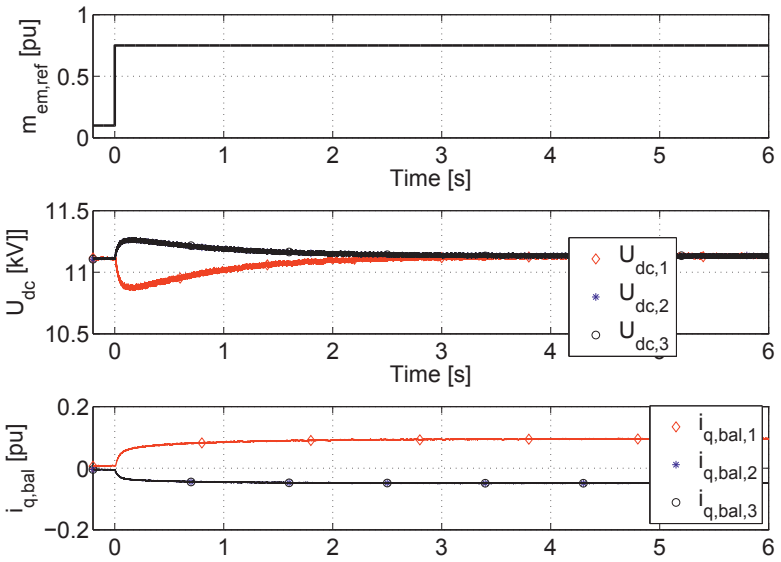

Figure 5.5: Response to a step in torque with fixed shaft speed. From top to bottom: Torque reference input. DC-bus voltages. DC-bus voltage control output.

effect on the DC-bus voltages is minor, and compensated by the DC-bus voltage control in each module. A maximum DC-voltage imbalance of approximately 1.8% is observed following the torque step. Hence, the DC-bus voltage control system is capable of limiting the impact of a disturbance in the torque satisfactorily.

5.2.4 Torque-based DC-voltage droop control

The simulation results which are used to analyze the torque-based DC-voltage droop control are all obtained by applying a torque reference step for a turbine speed of 0.9 pu. The torque step is from 0 to 0.75 pu, and the DC-bus voltage control is active.

Droop control response

In Sec. 4.3.3, it is argued that the DC-bus voltage control system without DC-voltage droop, is overdetermined. Additionally, it is stated that this overdetermined DC-bus voltage control can influence the steady-state torque of the turbine. As a result, the actual operating point of the turbine will differ from the set point generated by the turbine torque control. This phenomena is demonstrated by the simulation results presented in Fig. 5.6(a): The primary objective of the DC-voltage control system is fulfilled, i.e. the converter unit bus voltages are balanced.

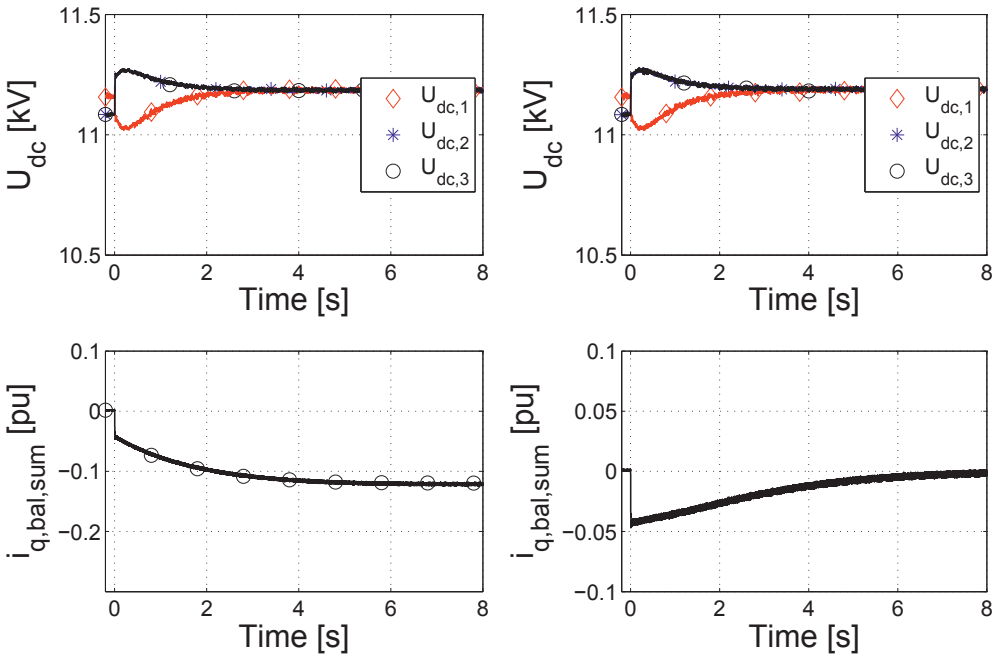

Figure 5.6: Droop control effect. a) Response without droop control b) Response with droop. Top to bottom: Module DC-bus voltages. Sum of DC-bus voltage control outputs.

However, the sum of the DC-bus voltage control outputs is not zero, but approximately -0.1 pu. This sum will be added to the torque reference, resulting in a steady-state contribution to the turbine torque from the DC-bus voltage control system. In this example simulation, the applied turbine torque will be 0.1 per unit less than the reference torque. As a consequence, the active power output of the turbine is influenced by the DC-bus voltage control.

The issue with overdetermined DC-voltage control is solved by introducing the torque-based DC-voltage droop, defined in Eq. 4.27, Sec. 4.3.3. The effect of the droop is demonstrated by repeating the simulations described in the previous paragraph, with the droop control implemented, Fig. 5.6(b). The DC-bus voltage control shows similar performance with regards to voltage balancing compared to the case without droop. Thus, the DC-voltage control primary objective is fulfilled also with the droop control. Additionally, the net contribution from the DC-voltage control system is brought back to zero, after a period of approximately 6 s. Hence, the turbine steady-state operation will not be influenced by the DC-voltage control when the droop is included. That is, the applied turbine torque will equal the torque reference in steady state.

The results presented in this paragraph demonstrate, that the torque-based DC-voltage droop is necessary for a modular control synthesis. This is because the modular control system requires that all modules are equal, and the turbine control requires, that the DC-bus voltage control only affects the converter unit's DC-bus voltage balance.

5.2.5 Flux weakening control in a turbine with variable module parameters

The flux weakening control is introduced to improve the controllability during transient overspeed of the turbine. In this paragraph, its performance is evaluated in the modular series connected converter in DC-bus voltage balance control mode. The purpose of the analysis is to identify special concerns related to the utilization of the flux weakening in the series connection. The variations in the module parameters defined in Table 5.1 are applied. The simulation results are presented in Fig. 5.7. The system is first brought to steady state at nominal wind- and turbine-speed. At nominal operation, the flux weakening of module 2 and 3 are active, due to the higher flux linkage in the corresponding stator segments. At t=0 s, a step in the wind speed (13 m/s - 15 m/s) is applied. As a result, the turbine speed increases, before the pitch control is able to limit the power capture. The consequence is an increase in the induced voltage of the stator segments, and higher flux weakening current requirement in module 2 and 3. The flux weakening control of module 1 remains inactive, due to the lower excitation of this segment. The result of the DC-bus voltage balance control is that there is additional current capacity in module 2 and 3, which can be used for the required flux weakening. The reduction in q-axis current during the transient is therefore minor. It can therefore be concluded, that the combination of DC-bus voltage balance control and flux weakening does not degrade the transient performance of the system during overspeed.

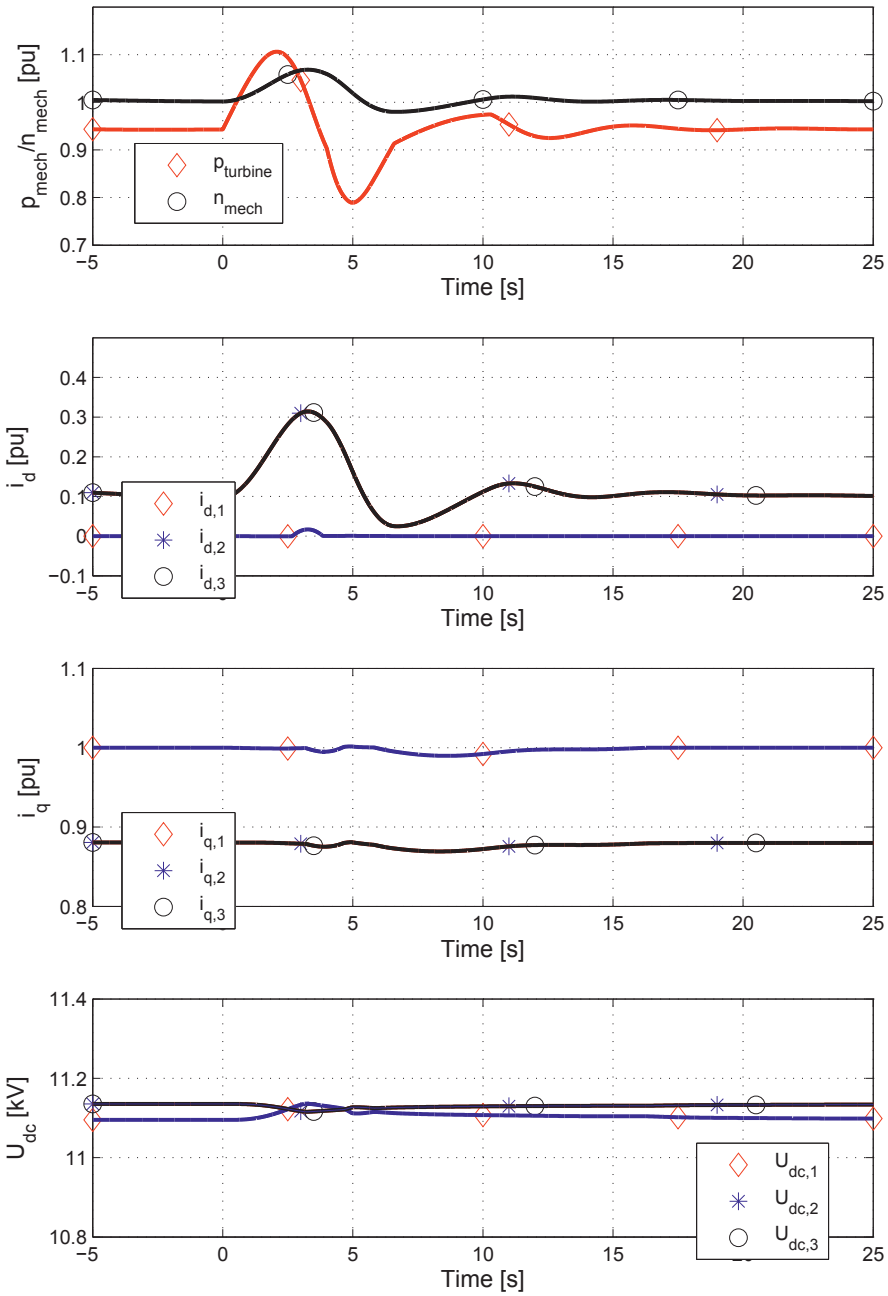

Figure 5.7: Flux weakening control with variable module parameters. Step in wind from 13 to 15 m/s, t=0 s. From top to bottom: Power/speed of the turbine. D-axis currents. Q-axis currents. DC-bus module voltages.

5.3 Turbine dynamic performance analysis

The results in this section are used to verify the correlation between DC-bus voltage control strategies and the performance of the modular series connected converter in a wind turbine.

5.3.1 Comparison of turbine power capacity under different control strategies

The DC-bus voltage balance control can result in different current loading for the modules. In Sec. 3.4.3, it is demonstrated that this difference in current loading can result in reduced power capacity from the turbine. In addition, the system transient behavior can be affected, since the current limit will be reached in some modules before others. Therefore, in the first part of this section, the modular series connected converter is analyzed for a balanced DC-bus voltage control, and compared to alternative control strategies. The simulation results are obtained applying a wind ramp from 6 m/s to 13 m/s, and parameter variations according to Table 5.1. The three control strategies evaluated are:

1. Current-control mode.
2. DC-bus voltage balance up to current limit, then current-control mode (uncompensated voltage control).
3. DC-bus voltage balance and derating of the turbine nominal torque/power when the current limit is reached (compensated voltage control).

The results are presented in Fig. 5.8, displaying the results for module 1.

Current-control mode: The first set of results (red lines, diamond shaped markers) in Fig. 5.8 are obtained for current-control mode. The deviation in voltages is increasing with the turbine speed and power, in accordance with the relations developed in Sec. 3.4.2. At 13 m/s, the voltage deviates from its average by 8 % (approximately 900 V). This deviations does not appear to be large. However, it will be reflected on the generator segment insulation requirements, and comes in addition to redundancy overrating requirements. Another consequence is that the torque in segment 2 and 3 is 5 % above the rated, while in module 1, it will be 5 % less. This will cause an imbalance in the mechanical forces distributed along the generator disk. The current-control mode results possibly in large deviations in module stress, in addition to instability risk around start-up, and is not a suitable operation strategy.

DC-bus voltage control without compensation for current limitation: The second set of results (blue curve, asterisk shaped marker) in Fig. 5.8 are ob-

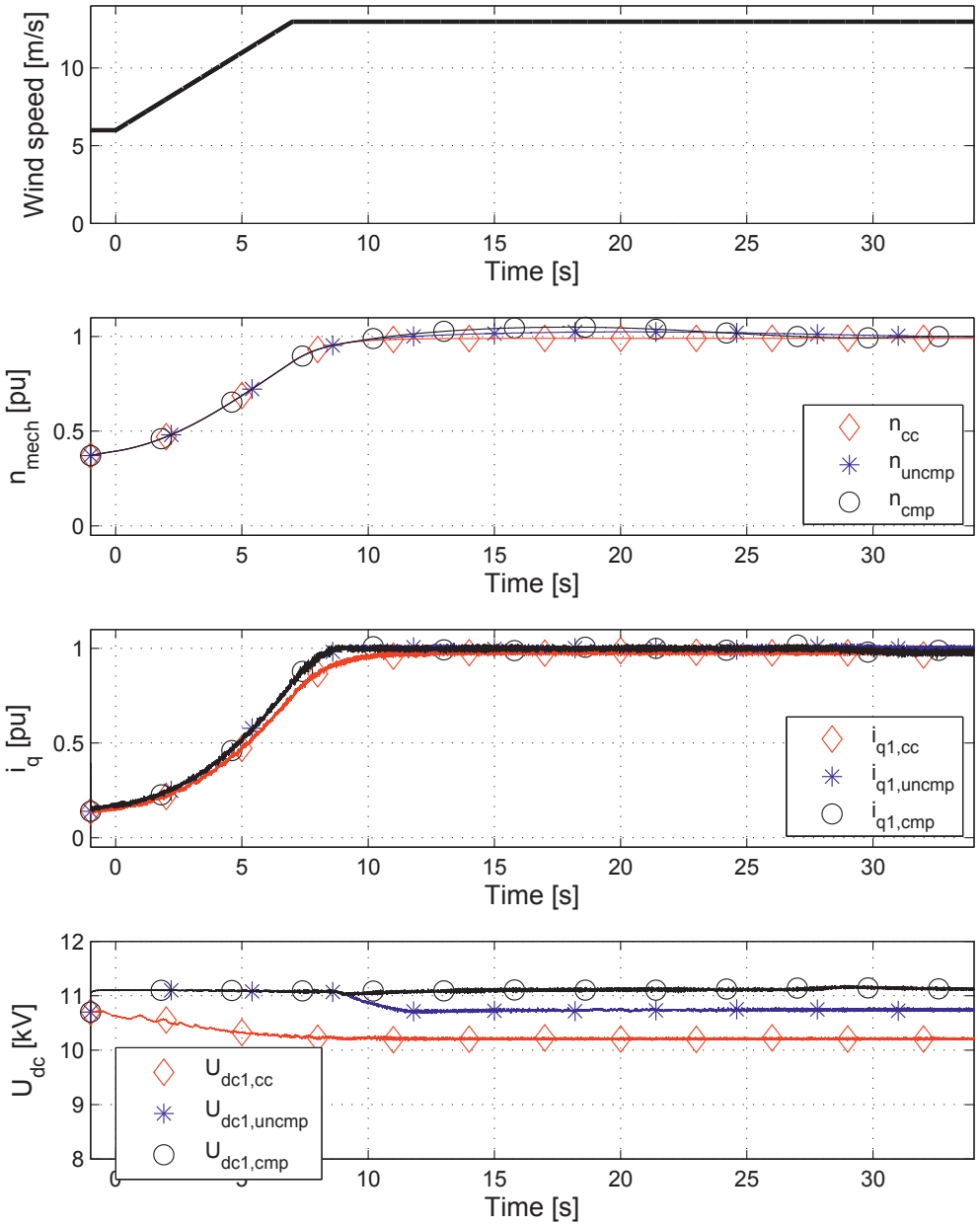

Figure 5.8: Comparison of current control (cc), uncompensated DC-bus balance control (uncmp) and compensated DC-bus balance control (cmp) for a wind ramp from 6 m/s to 13 m/s. From top to bottom: Wind speed input. Turbine speed. Q-axis current from module 1. DC-voltage response in module 1.

tained for uncompensated DC-voltage control. Thus, the DC-voltage balance is maintained when possible, but priority is given to torque control. The steady-state current limit is reached in module 1 when the torque reference is approximately 0.93 pu, due to the contribution from the DC-bus voltage control. Consequently, DC-bus module voltage control is lost since there is no control reserve for voltage regulation. This means that an imbalance in the mechanical stress on the construction is allowed to occur at maximum load. However, the long term stress on the insulation is reduced compared to a completely uncontrolled strategy, since balanced buses are achieved up to approximately 93 % of the power range. The small signal instability in motor mode will not cause problems in this mode, since control is regained when the torque reference is reduced.

DC-bus voltage balance with compensation for current limitation: For the last simulation results in Fig. 5.8 (black line, circular marker), converter unit DC-bus voltage control is given priority. In order to obtain balance for the entire operating range, the additional current demand from the DC-voltage control is taken into account by the torque limiter in the turbine control, reducing the torque reference so that Eq. 5.2 holds for all modules

$$m_{em,ref} + i_{q,bal,i}\psi_n \leq i_{s,i,max}\psi_n \tag{5.2}$$

Equal to the uncompensated-reference case above, the current limit in module 1 is reached before the nominal turbine operating point. The consequence is that the turbine speed increases until the pitch control reacts and reduces the total turbine power sufficiently to comply with the required derating.

Comparison of captured power from the three control strategies

The simulation results demonstrate a significant difference in power capture between the three analyzed operation strategies, Fig. 5.9(a) (With corresponding pitch angle in Fig. 5.9(b)). The uncompensated DC-voltage strategy results in approximately 5 % more power at rated wind than the strictly balanced approach. Consequently, the system design should consider a trade off between necessary derating, DC-voltage control strategy, mechanical stiffness and tolerances in the turbine assembly.

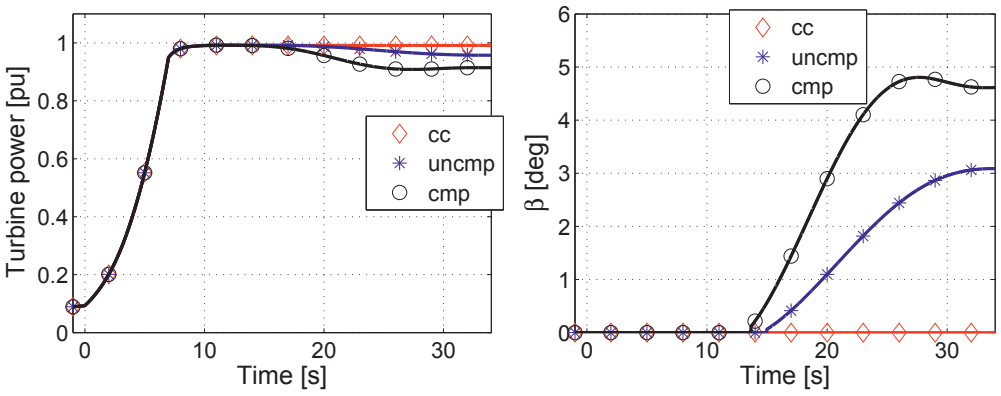

(a) (b)

Figure 5.9: Turbine power output for different control strategies a) Output power b) Corresponding pitch angle.

Comparison of modules connected in series and parallel

In the first part of this section, different strategies for operation of the series connected converter are analyzed. The required turbine derating when demanding balanced DC-bus voltages is demonstrated. Here, the steady-state performance is assessed for balanced DC-bus voltages, Fig. 5.10(a), and compared to a modular system with parallel DC buses, Fig. 5.10(b). For consistency, the module parameters are identical for the series- and parallel-connected cases.

For the cases with identical modules, there is no difference between the energy yield between series- and parallel-connected modular systems, since no compensation of power is required to maintain balanced bus voltages. With variations in module parameters, one of the drawbacks of the series connection compared to parallel systems becomes evident. The power capture is reduced for the series connection, while for the parallel case, the module parameters do not influence the output power. The loss of power can be explained by referring to Eq. 3.24: It is the module parameter difference from the average parameter values which is the determinant, not the absolute values.

From comparison presented above, it becomes clear that the total system efficiency gain which is claimed for the transformerless offshore wind turbine system in [61] may be lost or diminished. The system efficiency will depend on the combination of control strategy and module parameter variations.

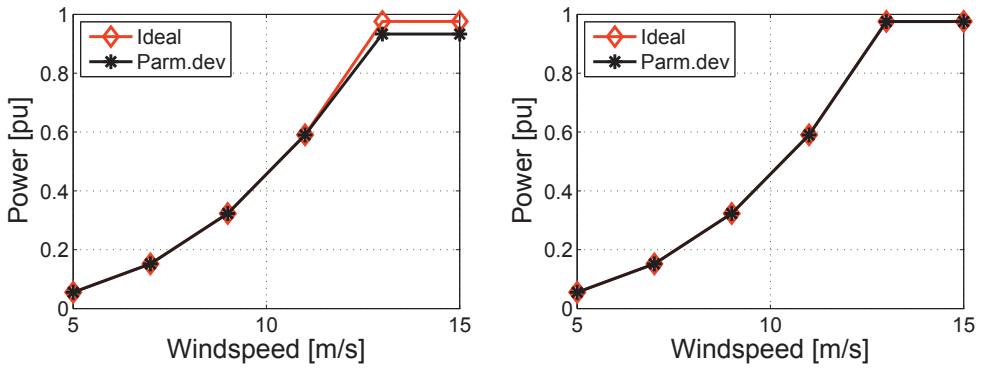

Figure 5.10: Turbine captured power as function of the wind speed for identical and variable module parameters. a) Series connection. b) Parallel connection.

5.3.2 Turbine simulation with realistic wind speed input

The noise, gusts and ramps of the wind are neglected to isolate and illustrate certain aspects of the system behavior for the simulation results in the previous sections. In the following, the wind speed pattern in Fig. 5.11(a) is applied, in order to assess the system performance for more realistic conditions. The wind speed curve is generated based on the input data from Table D.1.

The system transient performance is evaluated for three different cases:

- Balanced DC-bus voltages and equal module parameters in the system.
- Current-control mode and parameter variations.
- Balanced DC-bus voltages and parameter variations.

According to the previous sections, and the theory developed in Chapter 3, this should result in equal power for the two first cases, and decreased power for the last case. This holds, according to Fig. 5.11(c). An additional observation is that there is little difference in the turbine speeds for the three cases, Fig. 5.11(b). This indicates approximately same stress on the mechanical drive train. If the derating due to the voltage balancing is disregarded, the turbine performance is equivalent to a standard, 3-phase machine.

Based on the simulated output power curves in Fig. 5.11(c), the consequences of the operation strategy on the energy yield can be estimated. For the entire time span, the energy capture is listed in the first column of Table 5.2. By splitting the energy output into before and after the rated speed is reached, the relation to Eq. 3.33 is verified. Before rated operation, the difference is negligible, while there is a 7 % deviation from the imbalanced case from rated speed. Applying

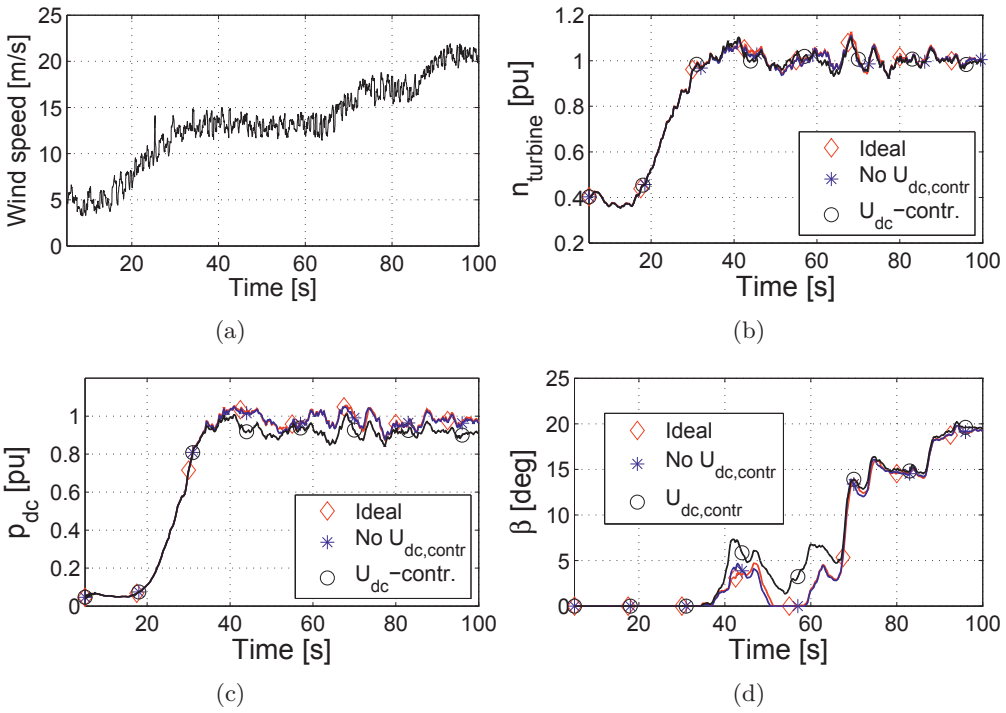

Figure 5.11: Transient, realistic wind input. Comparison of an ideal system, variable module parameters with and without DC-voltage balance control. a) Input wind speed b) turbine speed c) Converter chain output power d) Pitch angle, β.

the parameter deviations of Table 5.1 and introducing a current limit of 1.0 pu results in a theoretical maximum torque of 0.94 pu, i.e. 6 % deviation.

Table 5.2: Estimated energy capture

	Ideal case	*Imbalance case*	*Balanced case*
Energy produced , total	72.84 MJ	72.50 MJ	68.86 MJ
Energy before rated speed	7.96 MJ	7.93 MJ	7.92 MJ
Energy after rated speed	64.85 MJ	64.57 MJ	60.94 MJ

5.4 Transient fault analysis

This section presents the transient analyses of the fault scenarios which are investigated for steady state in Sec. 3.5: The transient response to a converter unit trip, the post-fault reaction to the trip (reconnection or bypass of the converter unit) and independent module operation. The purpose of this section is to verify that the faults do not result in unacceptable transient behavior, and consequently, that the steady-state fault-tolerant operational modes can be achieved.

The fault-tolerant simulation results are obtained with a turbine model consisting of N=9 modules. The reason for this is explained in Sec. 5.1.

5.4.1 Converter unit trip and redundancy

Response to converter unit trip

In Sec. 3.5.2, it is argued that there exists a DC-current path, and hence fail-to-safe mechanism, for a converter unit trip in the modular series connected converter. Additionally, it is demonstrated that the operation after a converter trip is indeed safe. However, this does not address the transient behavior following the fault. Fig. 5.12 presents therefore the simulation results for the response to a converter unit trip. The system is first brought to steady state at nominal-speed and -power. Then, converter unit 2 is tripped. The first consequence of the trip is that the diodes are reverse biased and the stator segment currents blocked. During this phase, the DC-link current is discharging the bus capacitor. After 1.65 ms, the faulty module DC-bus voltage, $u_{dc,f}$, is sufficiently reduced for the diodes to become forward biased. The converter unit is now entering a passive rectifier mode. The stator segment currents are flowing, and the DC-bus voltage is stabilized at the new level. Excess voltage is distributed to the $N-1$ healthy modules, resulting in a small increase in their bus voltage. All the healthy converter units continue the stable operation. The new operating point is characterized by the turbine rotor speed and the power extraction by the healthy modules, according to Eq. 3.36.

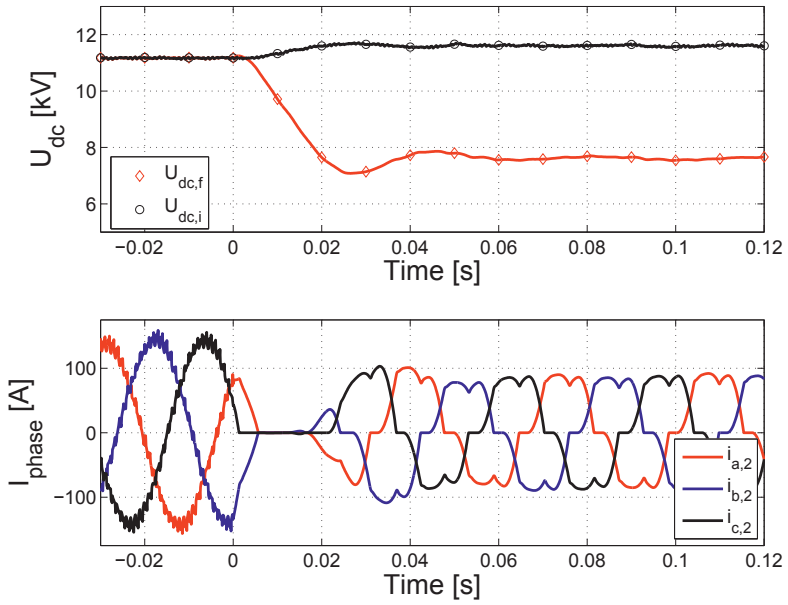

Figure 5.12: Converter unit trip at t=0.0 s. n_{mech} = 1.0 pu, $m_{em,ref}$=1.0 pu. Upper plot: DC-bus voltage of module 2 and and an arbitrary, healthy module *i*. Lower plot: Phase currents of stator segment 2.

Reconnection of a falsely tripped module

The possibility to perform a reconnection of a falsely tripped converter unit is discussed in Sec. 3.5.2. The steady-state flux weakening requirements for reconnecting with the converter unit operated in the linear region are identified. It is demonstrated, that the module-current requirements are too high for linear operation during reconnection near nominal operation. Therefore, the minimum flux-weakening current, that can be applied and still avoid inrush currents, is also identified. In this paragraph, the transient performance of the two strategies for reconnection are compared.

For the simulation results in Fig. 5.13, it is assumed that a false trip has occurred, and been detected. The transients after the trip are eliminated and the turbine operating point is n_{mech} = 0.8 pu, $i_{q,h}$ = 0.8 pu. Reconnection is initiated at t=0.0 s. First, the references for the d- and q-axis currents are set according to Eq. 3.40 and Eq. 3.43, for linear modulation (compensated case, *cmp*). Then, the reconnection of the converter unit with current references equal to the fault currents $i_{d,f}$ (Eq. 3.47 and $i_{q,f}$ (Eq. 3.45), is performed (uncompensated case, *uncmp*).

For the compensated case, a minor transient can be observed in the module voltage, $U_{dc,f,cmp}$ for the first phase. This transient is eliminated after approximately

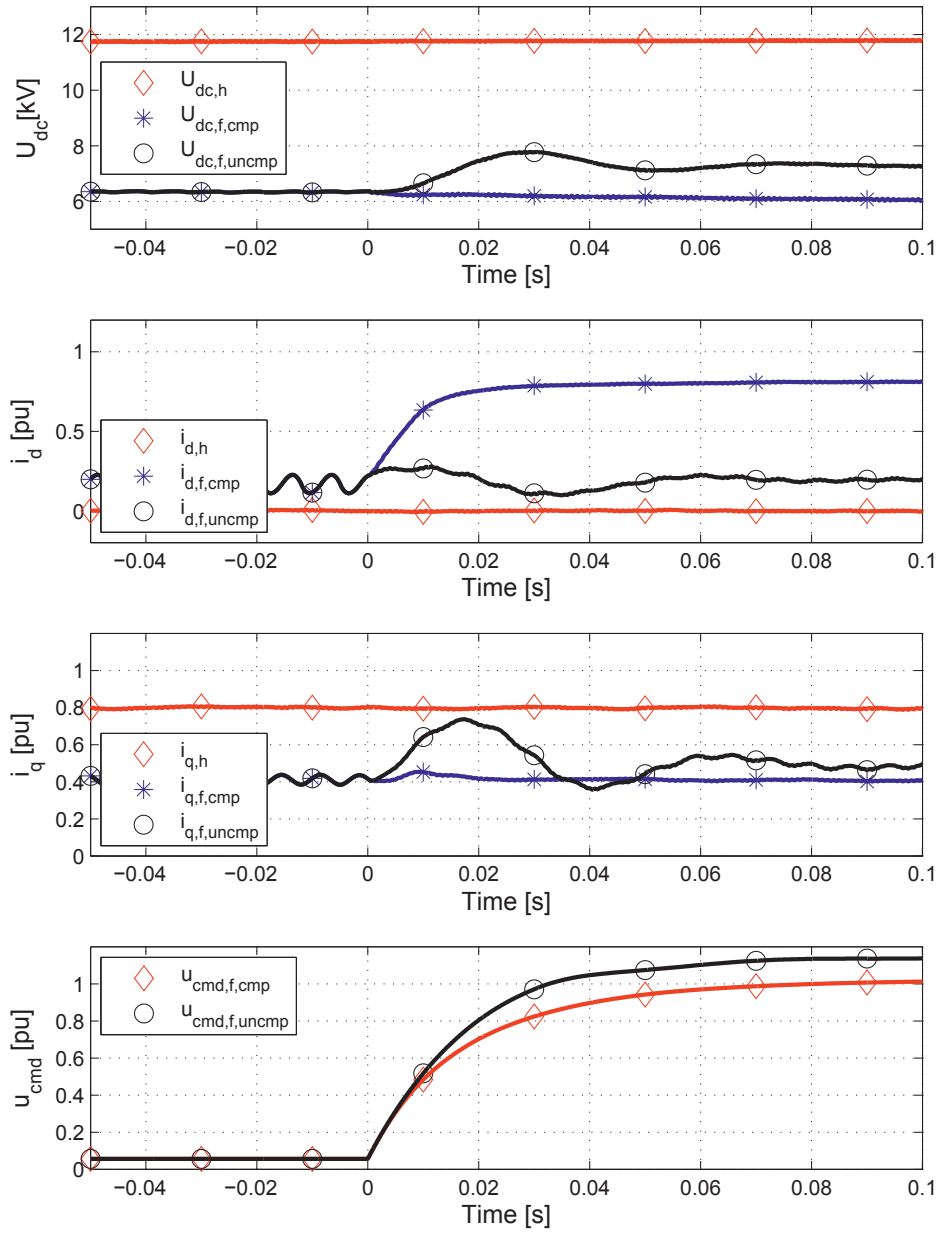

Figure 5.13: Reconnection of a tripped converter unit, $n_{mech} = 0.8$ pu and $m_{em,ref} = 0.8$ pu. From top to bottom: DC-bus voltage for a healthy module (h), tripped module (f,cmp) and tripped module without compensation(f,uncmp). D-axis current. Q-axis current. Degree of modulation.

50 ms, and the bus voltage is stabilized. The d-axis current is controlled to its reference value of 0.83 pu, and the depth of modulation is approximately 1.0, which is in accordance with the requirement. The DC-bus voltage is slightly lower after

the reconnection, indicating that the losses are not completely accounted for by the estimate in Eq. 3.43. The healthy converter units remain in practice unaffected during the operation.

From Fig. 5.13, it is clear that the uncompensated case yields a poor performance: The q-axis current experiences heavy oscillations, which are reflected in the converter unit DC-bus voltage. Consequently, the flux weakening results in an oscillating d-axis current. Hence, the uncompensated case results in a response which is not desirable.

When the steady state is achieved after the converter unit is reconnected, the module-DC voltage can be brought back to normal operation by applying a ramp to the DC-voltage control, and reducing the absolute value of $i_{d,ref,f}$. The procedure will be similar to the black-start of the system which is demonstrated in Sec. E.7, but applied to a single module.

Bypass of a tripped module during continued turbine operation

The complete bypass sequence for a converter unit trip is verified by the simulation results presented in Fig. 5.14. The results illustrates the transition from converter trip to redundant mode. The first phase (t=0.0 s to t=0.02 s) is identical to the trip demonstrated in Fig. 5.12. The second phase starts at t=0.02 s, when the opening of the circuit breaker is initiated. The phase currents are interrupted, and the DC-link current discharges the bus capacitor completely. In the third phase, the diodes of the faulty converter unit are forward biased, clamping the capacitor voltage to zero. The bypass is now completed and the fourth phase is a recovery phase for the remaining N-1 modules: Since the DC-bus voltage control references are not updated sufficiently fast after the trip, the healthy module DC-bus voltage controllers are overreacting. This is the cause of the transient drop in the DC-link current. Finally, the bypass operation is completed at t=0.4 s and redundant operation is achieved for the modular series connected converter.

Except for the sudden loss of torque in segment 2 due to the converter unit trip, there are no extreme physical stresses during the bypass. The most important effect is the transient drop in DC-link current which is approximately 35 %.

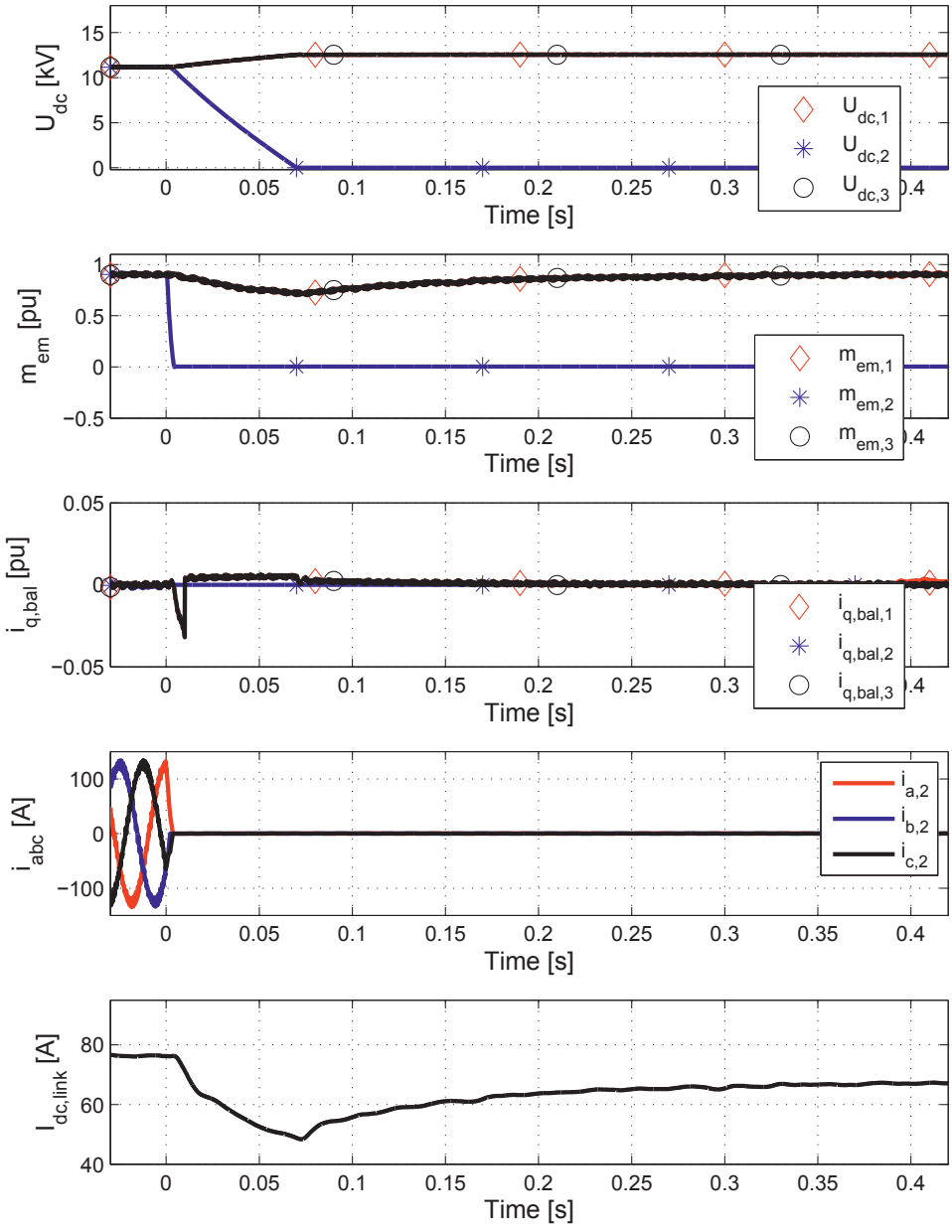

Figure 5.14: Bypass of module 2 during operating, n_{mech}=0.9, $m_{em,ref}$=0.9. Top to bottom: DC-bus voltage. Stator segment electromagnetic torque. DC-bus voltage control output. Stator segment currents faulty module. DC-link current.

5.4.2 Module overtemperature mitigation through individual deloading control

The possibility for independent module deloading control is analyzed theoretically in Sec. 3.5.3. This analysis requires that the full voltage-operating range of the converter unit is utilized. Based on this operating range, the physical limit for the individual deloading is identified. Further deloading of the module requires reduction in the total turbine torque. The transient behavior of this control is analyzed based on the simulation results presented in Fig. 5.15: First, the current limit is reduced to 0.9 pu in module 1 at t=0 s. This limit is within the range of the individual deloading operation. The DC-bus voltage reference for module 1 is reduced accordingly, while the overshooting DC-voltage is distributed to the $N-1$ healthy modules. The q-axis current of the affected module is reduced by the output of the DC-bus voltage control in module 1, and equally increased for the healthy modules. The total turbine power derating at this stage is minor, but required in order to not overload the $N-1$ healthy modules. At t=20 s, the current limit is further reduced, to 0.6 pu. This deloading requirement is beyond the limit for voltage reduction. As a consequence, the faulty module voltage reference is first reduced to its minimum, entering maximum overmodulation of the converter unit. After this limit is reached, the remaining deloading is achieved through reduction of the total turbine torque. The total turbine output power is 72 % of the rated power when the deloading is completed. This means that the faulty module should be disconnected, to maximize the turbine output. However, this limit is operational, and the disconnection is in theory only required to maximize the turbine output power. The modular series connected converter may continue to function in the obtained operating point.

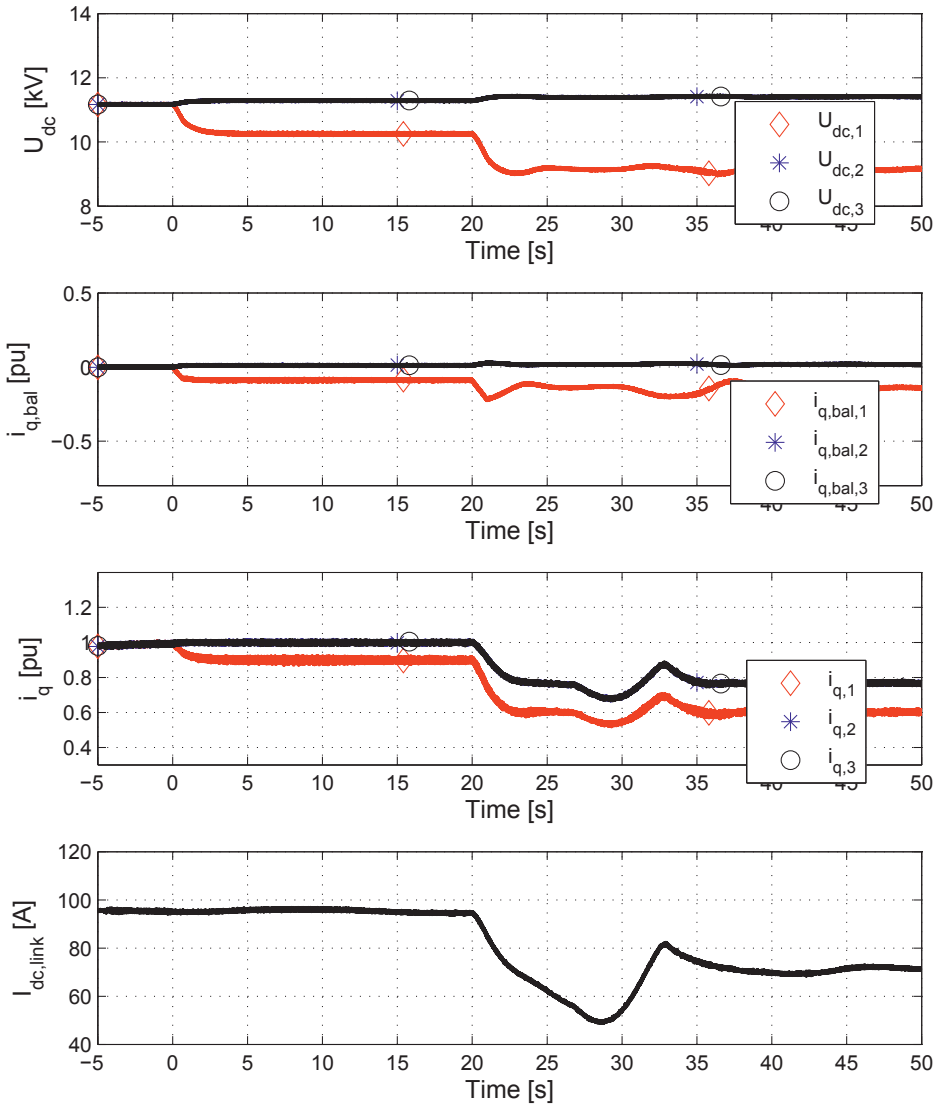

Figure 5.15: Independent deloading of module 1. t=0 s, $i_{q,lim} = 0.9$ pu, t=20 s, $i_{q,lim} = 0.6$ pu. From top to bottom: DC-bus voltages. DC-bus voltage control output. Module q-axis currents. Turbine output current, $I_{dc,link}$.

5.5 Summary of system transient analysis

This chapter has given the analysis of the dynamic performance of the converter operation and control based on simulations in PSCAD. First, the transient behavior of main blocks of the modular converter control system is analyzed. The emphasis is on verification of the properties for the different control blocks presented in the control synthesis. This section started with the module control, i.e. current control and DC-voltage control, and continued on to the droop control verification and transient performance evaluation. The simulation results have verified, that the control synthesis yields a stable, modular control system for the modular series connected converter.

Second, the simulation results for evaluation of the system performance in normal turbine-operation mode are presented. These simulation results confirmed that the overall performance is similar to a standard generator/converter solution for a variable speed wind turbine. However, it is shown that the choice of control strategy for the DC-bus voltages of the converter units will affect the power capture capability, given the presence of module parameter variations. For equal (ideal) module parameters, the DC-bus voltage control strategy will not influence the turbine maximum power.

The third part of this chapter analyzed converter unit fault scenarios. The impact of a converter unit trip on the converter chain is investigated, and the response is found to be acceptable for the remaining functioning modules. Additionally, the continued operation possibilities (bypass or reconnection) are analyzed - both can be achieved without compromising the converter chain. The individual module deloading control is demonstrated, including the transition from individual deloading to turbine deloading control.

The system can provide black-start functionality. The principle of such an operation is demonstrated in Appendix E.7.

6 Experimental Verification

This chapter presents the premises, limitations and results from the experimental verification of the theory and simulation results from Chapter 3-5. The generator model, control blocks, system operation, redundancy and fault tolerance are verified. The purpose of the experimental verification is proof of concept.

6.1 Introduction

6.1.1 Motivation and scope for the experimental work

The experimental results presented in this chapter are intended for conceptual verification of the theoretical results and simulations in the previous chapters. Two main objectives have been defined:

- Verification of the behavior of the series connection of 3-phase converters in which one or more modules are operated on a floating potential, herein the simulation model.
- Verify the operation and control concepts developed for the generator/converter system

Only [36] has earlier presented experimental results for the converter concept investigated in this thesis. This experimental verification was based on a laboratory setup consisting of two converter units connected in series. Each VSC unit was connected to separate generators which were mounted on the same shaft. The obtained results verified the DC-bus voltage control aspects and converter operation. The experimental results presented in this thesis builds on these results, and generalizes them, by extending the series connection to include several floating converter units. Additionally, the operation of the converter chain together with one physical, modular generator unit is verified. Finally, the developed fault-tolerant concepts are investigated.

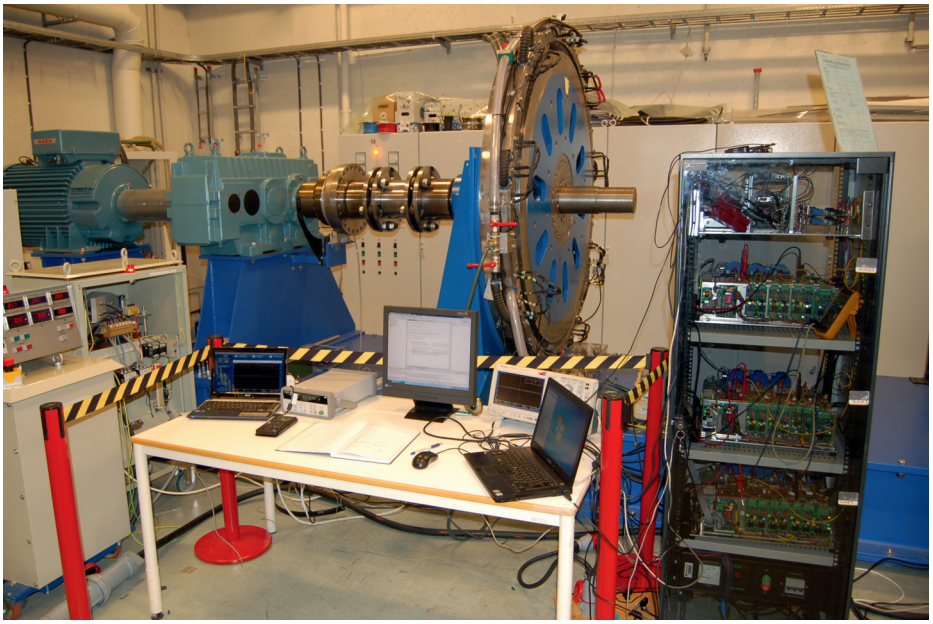

Figure 6.1: Laboratory setup: Input induction machine, gearbox and low speed shaft connection to the large diameter modular generator in the back. Modular series connected converter with the FPGA-control cards in the rack.

At a more detailed level, the following aspects are investigated experimentally:

- The magnetic decoupling between stator segments, for verification of the modular control approach and simulation model for the generator.
- Stable operation of the series connection of VSC units with one or more units operated on a floating voltage potential in generator mode.
- The impact of module parameter variations on the DC-bus steady-state voltages in current-control mode.
- The DC-bus voltage control system:
  - Feasibility of a modular control synthesis approach for the converter chain, with floating modules connected to a single machine.
  - Droop control - functionality.
- Fault-tolerant control:
  - Converter unit trip and redundant operation of a VSC unit.
  - Individual module deloading control for overtemperature mitigation.

The experimental results presented in this chapter were obtained using a prototype of the AF-IL PMSG rated at 45.2 kW, with three stator segments and converter units rated at 20 kW each.

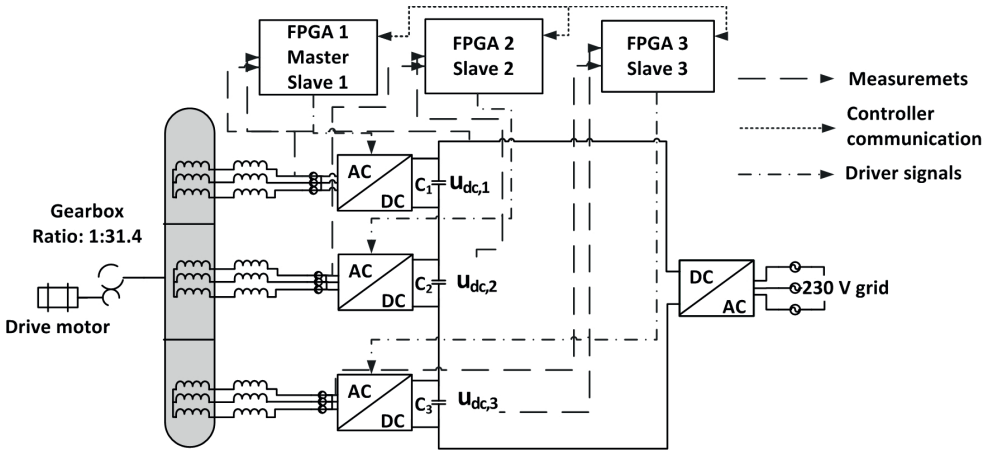

Figure 6.2: Principles of the experimental setup with the AF-IL PMSG prototype, modular series connected converter and load.

Limitations of experimental results

Due to the limitations of the laboratory setup, the special generator insulation solution is not investigated in the experimental work. Additionally, the generator prototype is not pushed to its mechanical limits. These limitations are not considered to constrain the experimental verification for this thesis.

6.1.2 General description of the laboratory setup

The 45 kW prototype of the AF-IL PMSG was made by SmartMotor [127]. The prototype generator is originally designed with a standard 3-phase stator winding, with a rated voltage of 240 V. For the setup presented here, Fig. 6.2, the windings are reconfigured into three electrically isolated 3-phase windings: One for each stator segment, as illustrated in Fig. 3.1, Sec. 3.1.1[1]. The generator prototype is derated in two ways due to limitations in the laboratory rig: 1) The nominal speed is reduced to 40 rpm due to limitations in the gearbox. 2) The nominal current is limited to 35 A_{rms}, due to trouble with the laboratory water cooling system. The 20 kW converter units are designed for laboratory use [128]. This includes oversized semiconductors [129], and a conservative protection system with an extensive interlock circuit resulting in robustness against overload and control system errors. An equipment list is given in Appendix F.5. In Table 6.1, the main parameters for the setup are listed.

[1]In Appendix F.2, the no-load voltages of the 3-phase configuration and three-segment configuration are documented and compared.

Two different DC loads are used for the experimental work:

- **Resistive load and diode bridge charging circuit:** A resistive load is utilized to verify the machine magnetic decoupling, impact of parameter deviations, the DC-bus voltage control system and the DC-droop control. The resistor is connected between the positive- and negative-rail of the DC link. To guarantee a minimum operating DC-bus voltage, a diode bridge is charging the DC link to 0.9 pu voltage at no load. For simplicity, the load is hereafter referred to as *resistive DC load*.
- **Grid connected converter in constant DC-link voltage control:** The grid-connected converter is emulating an externally controlled DC-link. This load is used for further verification of control and operation of the system, and the fault-tolerant modes.

Definition of load cases: Two variable load profiles are used for the laboratory tests. Load case 1 is variable torque, fixed speed, and load case 2 is variable speed, fixed torque. The profiles consists of stepwise ramps from low to high power and back to low power again. The detailed sequences are defined in Appendix F.4.

Table 6.1: Main laboratory parameters

Parameter	*Value*
AF-IL PMSG rated power	45.2 kW
Generator rated voltage, U_{ll}	240 V_{ll}
Generator rated current with water cooling, $I_{n,max}$	110 A_{RMS}
Generator rated current without water cooling, I_n	35 A_{RMS}
Generator rated speed, n_n	74 rpm
Max generator speed due to gearbox, n_{max}	40 rpm
Pole pairs	24
Number of modules, N	3
VSC-unit rated power	20 kW
VSC-unit switching frequency f_{sw}	2 kHz
VSC-unit bus capacitor C_{bus}	3300 μF
Total DC-link voltage with resistive load $U_{dc,tot}$	225 V
Total DC-link voltage with controlled voltage	300 V

6.1.3 Control system implementation

The control system is implemented using three identical control cards [130], one for each converter unit. The cards are based on Xilinx Virtex 5 FPGA[2] [131] with integrated PowerPC440 processor [132]. In accordance with the control system synthesis in Chapter 4, the interface between the master (turbine) control and slave (module) controllers is consisting of the torque- and DC-bus voltage reference. Additionally, the state of the master control is distributed to the slaves.

A standard control system frame is used as starting point for the modular controllers. The frame has been developed at the department as multi-purpose converter control system[3] based on the state machine in [133]. This controller frame contains a vector current control, hysteresis current control, voltage control, hardware and software dq-transformations, and software protection system. The purpose is to allow the user to focus on the implementation of high level control, without having to deal with the configuration details. A floating-point unit is included to avoid integer programming. The user can select and deselect control blocks with software settings depending on what is relevant for the application.

Some necessary additions to the standard 3-phase control have been developed for the modular control system:

- *Master/slave communication system:* For transfer of references, states, measurements and fault messages.
- *DC-bus voltage control:* Discrete PI control in each module controller.
- *Sensorless control:* A flux estimator and phase-locked loop (PLL) in each module for independent rotor position tracking.
- *DC-bus voltage reference control:* The torque-based DC-voltage droop control and DC-voltage average voltage reference is implemented in the master control routine.

Details on the implementation are given in the following paragraphs.

[2] A field programmable gate array (FPGA) allows the user to design and program the hardware, in opposition to the digital signal processor (DSP) where the hardware architecture is defined by the manufacturer. This allows the user to customize the hardware to fit the needs of the specific controller

[3] The standard control frame was developed by Sachin Thopate when he was master student at NTNU, Kjell Ljøkelsøy, SINTEF, and Roy Nilsen, Wärtsilä. Debugging and standardization was by Salvatore D'Arco, SINTEF, and the author.

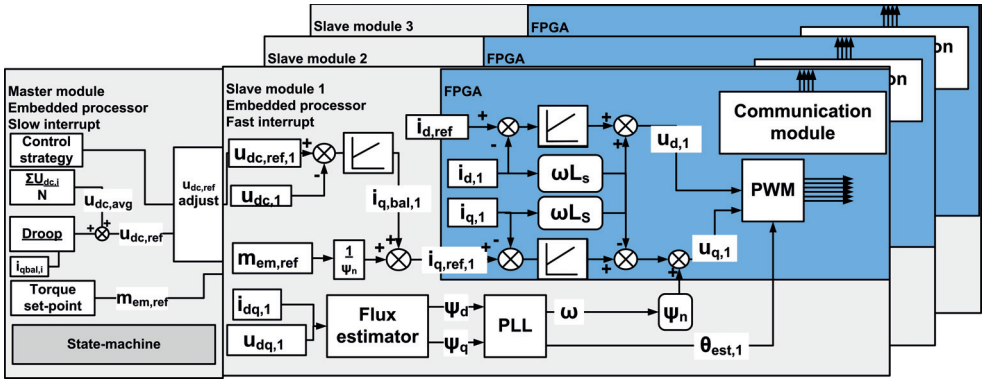

Figure 6.3: Block scheme of the modular control system with the FPGA-implementation level of the different control blocks indicated.

Control implementation hierarchy

The FPGA chip in each control card contains the processes that require high bandwidth. These include current controllers, measurement sampling, dq/abc-transformations, converter protection and master/slave communication bus. The relatively slower parts of the control system are implemented in the processor. The processor is divided into three levels: A background routine, an interrupt routine triggered by the PWM-carrier counter reset, and a timer-driven interrupt routine. The background routine is low priority, and is operating when the processor has available capacity. This routine handles the signal processing for real-time monitoring of control variables via the control card D/A-converter. The module control is implemented in the PWM-interrupt routine, which is given the highest priority in the processor. This routine contains the sensorless rotor position tracking, DC-bus voltage control and measurement sampling. FPGA-control blocks input/output is performed in this interrupt, together with software level fault detection. The timer-driven interrupt operates at 10 ms. In the slave controllers, reference update and state-machine duplication are handled in this routine. In the master-control timer interrupt routine, the DC-bus voltage reference control, main state-machine, and torque limiter functions are implemented. All user interactions, such as torque set point command and activation of the DC-voltage control system are input to the master timer interrupt. The organization of the control levels in the FPGA/Processor system is illustrated in Fig. 6.3.

Modular state machine and fault handling

The system state is set in the master-module state machine and duplicated to the slave modules. A simple state-update confirmation system has been developed

to ensure that all control modules have received, and are ready to enter the new state: First, the master control sends out the state update to the slaves. When the slaves have received the command, an acknowledge signal is returned to the master. The master is not allowed to update its state before both slave control cards have set the confirmation flag.

The fault detection in a module is transmitted to the other two modules in the same PWM-interrupt execution as the fault is detected, and each PWM interrupt starts by checking for fault messages from the other modules. This allows fault handling for the full modular converter system in maximum two switching periods. In order to update the system state, a flag is set by the fault handling routine, and the state machine is updated in the next execution of the timer-driven interrupt.

Master/slave communication

The communication between the master card and the two slave cards is programmed as FPGA modules. The communication is asynchronous, 32-bit data transfer. The external connection point on the control card is a digital, parallel, 20-pin input/output (IO) port. In the master module, an external peripheral controller (EPC) controls the data traffic [134]. Only eight of the 20 pins are available for data transfer, and each transfer is therefore divided into four sequences by multiplexing. The remaining pins are reserved for control signals such as read, write, device ready, and address specification.

The slave part of the communication system is designed as a 32-bit RAM-array, with generic size. Each 32-bit data cell consists of four bytes (8 bits per byte). A data cell is assigned to a specific address, and its bytes are given addresses from 0 to 3 relative to this base address. The RAM module is implemented with access both via the processor bus of the slave controllers and the external, parallel IO-port. The external access is controlled by the master module EPC. Data which are written by the master are read only for the slave, and vice verse. If a data cell is accessed, it is flagged as busy, and not available for other processes. This avoids conflicts between read and write processes, and is an important part of the realization of an asynchronous control system. Priority is always given to the ongoing process.

A software check of the updated references is performed in each of the control cards to avoid the effect of communication noise. This check compares the newly read variable to the previous. If the difference is outside a defined threshold, the new value is considered corrupted, and discarded. In the case of a corrupted variable, the old value is used until the next update cycle.

Rotor position estimate

A sensorless rotor position tracking scheme is implemented for each slave control module/stator segment. The flux estimator is based on that presented in [123], adapted to the PLL [135]. The resulting angles are the rotor positions referred to the respective stator segments.

Feedback-measurement configuration

The feedback measurements in each module consist of the 3-phase currents measured at the converter unit output terminals, and a DC-bus voltage measured across the bus capacitor. AC-current measurements are obtained with LEM current trafoshunfts [136] and DC-voltage by LEM voltage transducers [137]. The measured values are sampled in the control card AD-converter [138] and processed in each module control.

The per-unit values for the dq-current components and DC-bus voltages are sent to the master control unit for coordination of the control system.

6.1.4 Simulation model for comparison with the experimental work

The simulation model used for comparison of the experimental data to the simulation results in Sec. 6.2 is in principle equal to that used in Chapter 5, except that the rotor angles are estimated instead of measured. The DC load is modeled by a resistor in combination with an ideal diode bridge. The module parameters are according to the nominal parameters of the AF-IL PMSG prototype, Table 6.1.

6.2 Experimental result with resistive DC load

A schematic of the experimental setup is shown in Fig. 6.2. With the resistive load, the grid-connected AC/DC converter in the figure is exchanged with a DC-side resistor. A diode bridge is used to charge the DC link to an initial voltage of 0.9 pu at no load. The resistive load, R_{load}, is set manually, in steps. A nominal DC-link voltage of 225 V is used, i.e. 75 V per module.

The DC-voltage control reference is allowed to vary freely between 0.85 pu and 1.2 pu, depending on the system operating point. Inside these limits, the purpose of the control system is to balance the bus voltages. Outside the voltage limits,

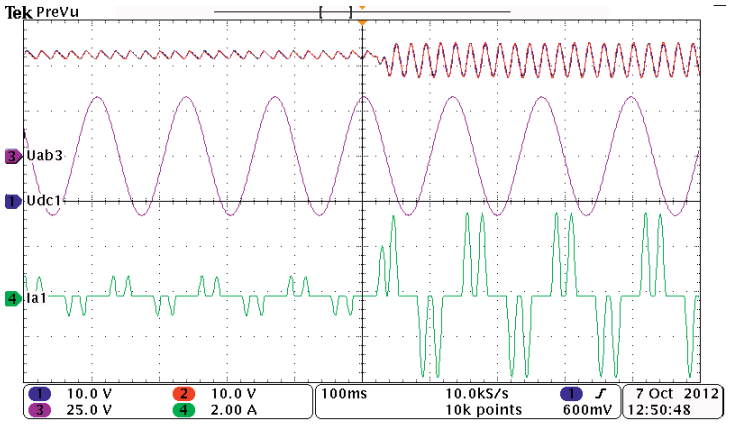

Figure 6.4: Magnetic decoupling of stator segments. Response to a step in the resistive DC load. (Ch.1 and 2: DC-bus voltages of the two connected modules. Ch.3: Induced voltage of the disconnected segment. Ch.4 Current of module 1).

the DC-bus control system is used to actively control the torque to prevent under- and overvoltages.

6.2.1 Magnetic coupling between stator segments

The results presented in this section are linked to the generator model development, Sec. 3.1.1 and Sec. 3.1.3.

The validity of neglecting magnetic coupling between the generator segments is verified by the results in Fig. 6.4. Hence, the assumption that the stator segments can be modeled as separate generators is also verified. In the experiment, two stator segments are loaded, while the third segment is disconnected. The generator speed is 20 rpm, and the DC buses are not precharged. The two connected converter units are used as passive rectifiers. A step in the DC load is applied at $t = 500\,ms$, with the system in steady state. The response to this step is observed as an increase in the phase current of module 1. In addition, the voltage ripple of $U_{dc,1}$ and $U_{dc,2}$ is noticeably higher. No response is observed in the induced voltage for the disconnected stator segment, neither transient nor stationary. Hence, it can be concluded that the magnetic coupling between the stator segments is negligible.

6.2.2 Current-control mode

Sec. 6.2.2 is related to the development of steady-state models in Sec. 3.4.2. It also demonstrates the stable operation of the system in the generator mode, Sec. 4.2.2.

Base configuration - no manipulation of the circuit

The module parameter dependency of the DC-bus voltage deviations in current-control mode is verified using experimental results obtained with the variable load cases defined in Appendix F.4. For load case 1, Fig. 6.5(a) shows the experimental results, with R_{load} set to 44 Ω. The initial deviation in the converter unit DC-bus voltages, $\Delta U_{dc,i}$, is 2.30 V, corresponding to an imbalance of 3.8 %. Hence, there are module parameter variations affecting the converter unit DC-power output present in the laboratory setup. At peak load, the deviation is 2.4 V, which is a negligible difference from the initial conditions. For load case 2, the results are presented in Fig. 6.5(b), with $R_{load} = 80$ Ω. There is a slight increase in the DC-bus voltage deviation as function of load compared to case 1 (From 2.1 V to 2.8 V).

The combination of the results from load case 1 and 2 suggests that the DC-bus voltage imbalance mainly depends on the rotor speed, and is independent of module current loading. According to the theoretical considerations in Sec. 3.4, this indicates that the stator segment flux variations are most prominent. However, the variations are too small to draw a definite conclusion.

The frequency of the oscillations in the uncontrolled DC-bus voltages corresponds to the mechanical generator speed. These oscillations are due to imbalances in the generator mechanical construction, which results in time varying flux linkage in the stator segments (see Fig. 6.5(b)). The average of the oscillations for the three converter unit voltages is zero, and hence, the DC-link current does not contain these oscillations.

The simulation results of Cases 1 and 2 in current-control mode are presented in Fig. 6.5(c) and Fig. 6.5(d) respectively. The simulation results coincide well with the experimental results. There are some minor differences in the total DC-link voltages at which the charging circuit (diode bridge) becomes reverse biased, but the main behavior of the converter system is the same. The cause of the difference is the simplified DC-load model, which does not take into account leakage inductances and losses in the transformer.

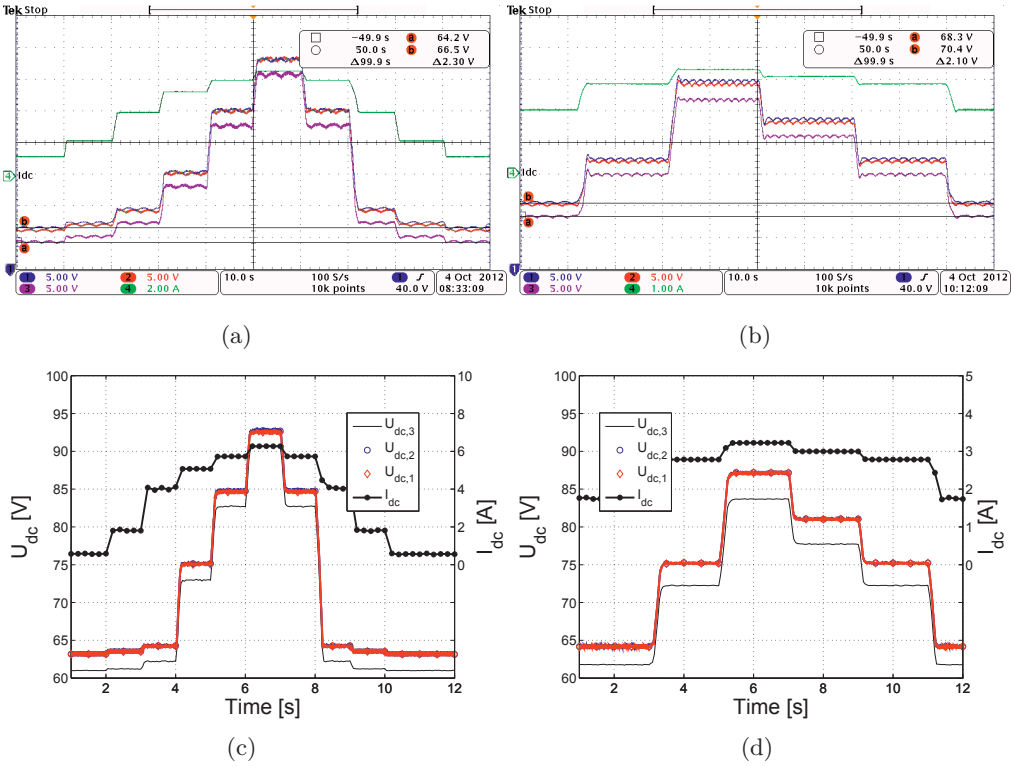

Figure 6.5: Current-control mode. a) Load case 1, experimental results. b) Load case 2, experimental results. c) Load case 1, simulation. d) Load case 2, simulation. (Ch.1: $U_{dc,1}$, Ch.2: $U_{dc,2}$, Ch.3: $U_{dc,3}$, Ch.4: $I_{dc,link}$).

Impact of variable module parameters

The results presented in the following paragraphs are used to further verify the relation between module parameter variations and DC-bus voltage deviations in current-control mode.

Loss imbalance: The losses in the different modules are modified by adding a 3-phase resistor[4] between one stator segment and the converter unit in series. This demonstrates the relation between variations in the module losses and the DC-bus voltage imbalance (according to the theory developed in Sec. 3.4.2). Load case 1 is repeated, first with the resistors added to module 1, Fig. 6.6(a). This module has the highest output power for the non-manipulated system, according to the previous paragraph. With added losses, $U_{dc,1}$ decreases relatively compared to the DC-bus voltages of the two unchanged modules, given an increasing system

[4]The resistor was measured to be 30 $m\Omega_{dc}$ per phase. Each resistor is made of a piece of steel wire.

loading. At the peak current loading, the power balance is changed sufficiently to alter the sign of the module-bus-voltage deviation.

The results in Fig. 6.6(b) are obtained with the resistors added to module 3. This converter unit has the lowest output power for the non-manipulated system. Consequently, the deviation of $U_{dc,3}$ from the average voltage is increasing with the system loading. At full load, the deviation is 9.9 V.

The results presented in Fig. 6.6(a) and Fig. 6.6(b) demonstrate the impact of module parameter variations on the converter unit DC-bus voltages.

Bus capacitance imbalance: According to the theoretical considerations in Sec. 3.4.2 and the simulation results in Sec. 5.2.1, a difference in module capacitance should not affect the steady-state behavior of the modular series connected converter in current-control mode. This is verified by adding a 3300 μF in parallel to the bus capacitors of module 2 and repeating load case 1, Fig. 6.6(c). The initial imbalance caused by the charging current is eliminated by the load current before acquiring the results. The added capacitor does not alter the DC-voltage imbalance compared to load case 1 for the base configuration, (Fig. 6.5(a)). Thus, it is verified that the steady-state DC-bus voltage deviations are independent of the bus capacitances in current-control mode.

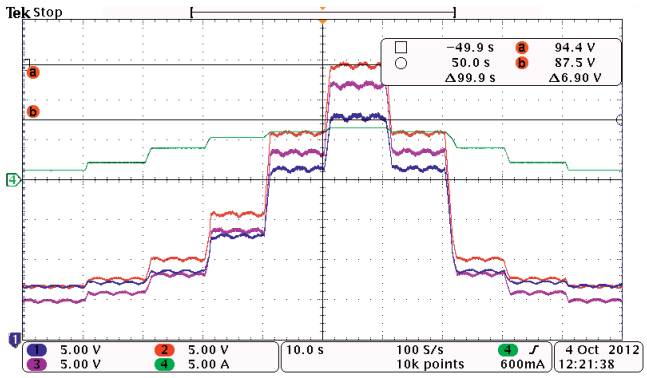

(a)

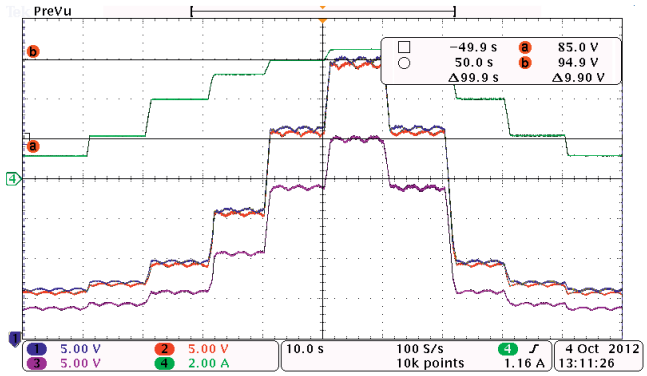

(b)

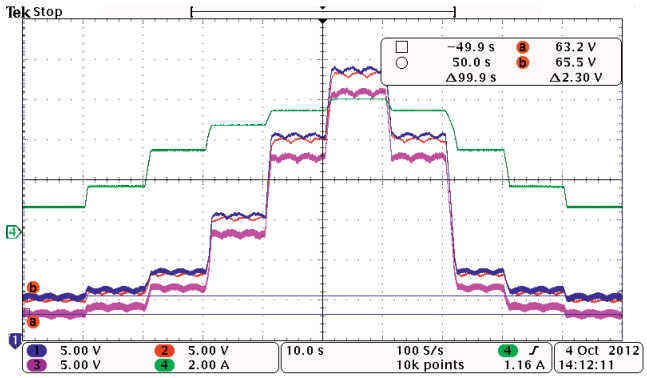

(c)

Figure 6.6: Current-control mode with manipulated module parameters, load case 1. a) Additional resistance in module 1 b) Additional resistance in module 3. c) $C_{bus,2}$ two times $C_{bus,1,3}$. (Ch.1: $U_{dc,1}$, Ch.2: $U_{dc,2}$, Ch.3: $U_{dc,3}$, Ch.4: $I_{dc,link}$).

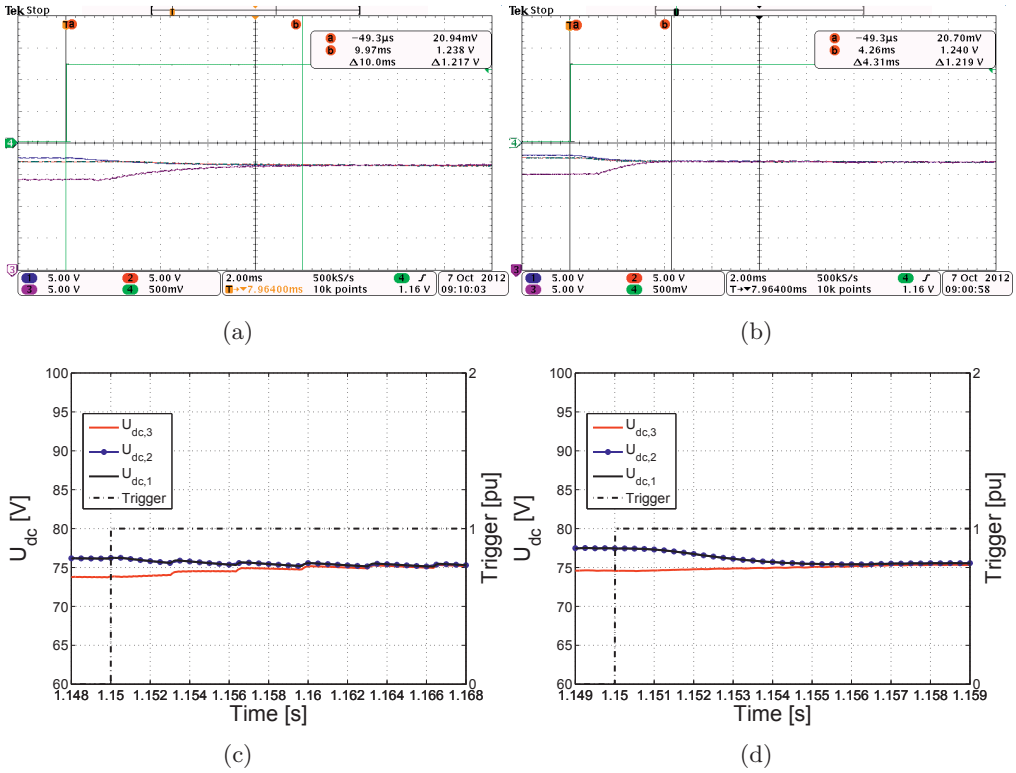

Figure 6.7: Activation of DC-bus voltage control. $m_{em,ref}$=0.04 pu. a-b) Experimental results, n_{mech} = 20 rpm and 40 rpm respectively. c-d) Simulation results, n_{mech} = 20 rpm and 40 rpm respectively (Ch.1: $U_{dc,1}$, Ch.2: $U_{dc,2}$, Ch.3: $U_{dc,3}$, Ch.4: Trigger).

6.2.3 DC-voltage control without droop control

The results presented in this section are used to verify the DC-bus voltage control synthesis Sec. 4.2.3, and the impact of not including the droop control.

DC-bus voltage balance control turn-on response

In the laboratory setup, the activation of the DC-bus voltage control was used to emulate a step response. Two set of results were obtained, for a generator speed of 20 rpm and 40 rpm. Since the DC-bus voltage control interacts with the module torque, doubling the speed should reduce the control response time by 50%.

The response to an activation of the DC-voltage balance control at 20 rpm and 0.04 pu q-axis current is presented in Fig. 6.7(a). The time to achieve balance is 10 ms. A response without overshoot is achieved, as required from the tuning, Sec. 4.2.3. Doubling of the generator speed, Fig. 6.7(b) results in a reduction

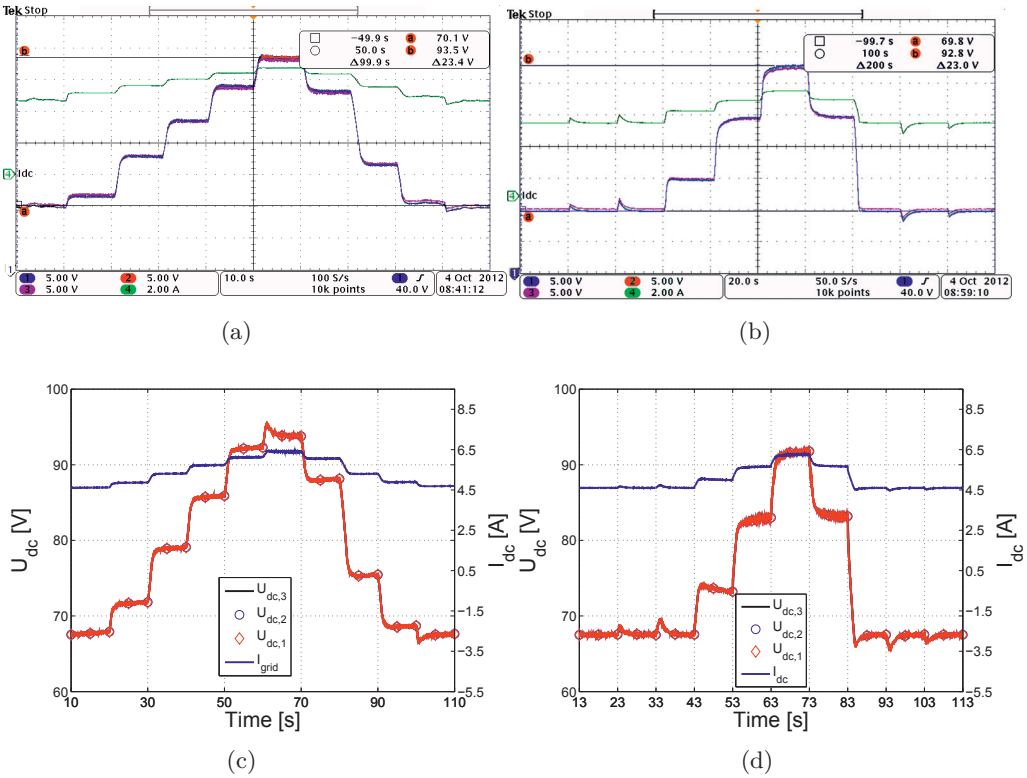

Figure 6.8: Response to a variable load profile, balanced DC voltages, load case 1. a) Experimental results without droop control. b) Experimental results with droop. a) Simulation results without droop control b) Simulation results with droop. (Ch.1: $U_{dc,1}$, Ch.2: $U_{dc,2}$, Ch.3: $U_{ab,3}$, Ch.4: $I_{dc,link}$).

of the DC-voltage balance response time by approximately 50 % ($\Delta T = 5.7$ ms, 57 %). As expected, the response time becomes generator speed dependent. The simulation results demonstrate the same behavior, Fig. 6.7(c) and Fig. 6.7(d).

Variable load response

The experimental- and simulation-results presented in Fig. 6.8(a) and Fig. 6.8(c) are used to verify the consequences of an overdetermined DC-voltage control system. In the results, the torque reference is equal for the time range from 10 to 20 s and the time between 80 and 90 s. Since the load is resistive, equal torque reference and generator speed should result in equal DC voltages, i.e. equal output power. However, from the results it is clear that this is not the case. This implies that the controllers are contributing to the total power output from the turbine. The contribution is a function of the previous system states. This will lead to non-

optimal performance for the turbine as is argued in Sec. 5.2.4. Consequently, even though the DC-bus voltage balance control primary task is performed satisfactory, it cannot be used for a modular control system.

6.2.4 DC-voltage control with droop

The following results are used for the verification of the torque-based DC-voltage droop control, Sec. 4.3.3.

The introduction of the droop control is demonstrated, theoretically and by simulations, to remove the DC-bus voltage control system steady state torque contribution, Sec. 4.3.3 and Sec. 5.2.4 respectively. In the following, the torque-based DC-voltage droop control is verified experimentally.

DC-bus voltage balance control response

The purpose of the DC-voltage droop is to remove steady-state contribution from the torque. At the same time, the droop should not affect the dynamic response of the DC-bus voltage balance control. This is verified by repeating the settings and operating point for the step response in Fig. 6.7(a), with the droop control activated, and compare the responses. The transient response to activation of the DC-voltage control system with the droop control is presented in Fig. 6.9. The time to achieve balanced DC-bus voltages is approximately 10 ms, which is equal to the case without the droop. Hence, it can be concluded that the DC-bus voltage control dynamic performance is not influenced by the droop control. This is in accordance with the simulation results and the control synthesis.

Variable torque with droop control - steady state output error removed

The torque-based DC-voltage droop should according to the control synthesis in Chapter 4 remove the steady-state offset between the torque reference and actual torque, which is caused by the DC-bus voltage control system. This is verified by the results presented in Fig. 6.8(b), page 125 (load case 1). By comparing these results with the corresponding results without droop, Fig. 6.8(a), the difference is identified: The steady-state deviation between the initial and final voltage levels which is observed in the no-droop case are removed by the droop control. Hence, the introduction of the droop eliminates the contribution from the DC-bus voltage control to the turbine torque. The simulation results show the same behavior, Fig. 6.8(d).

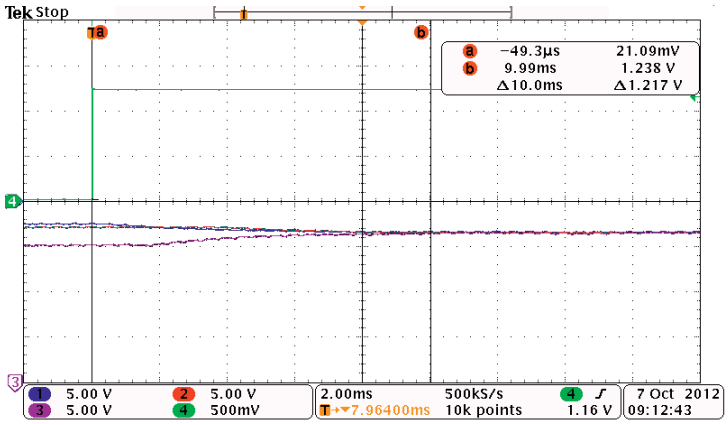

Figure 6.9: Activation of DC-bus voltage balance control, with droop control. n_{mech}=20 rpm, $m_{em,ref}$=0.04 pu. (Ch.1: $U_{dc,1}$, Ch.2: $U_{dc,2}$, Ch.3: $U_{dc,3}$, Ch.4: Trigger).

The transients observed in the DC-bus voltage in the initial part of Fig. 6.8(b) occur because the resistive load setting results in an initial DC-link voltage which is under the DC-bus voltage reference lower limit. Therefore, the DC-bus voltage control is actively increasing the power output to meet this minimum DC-voltage. Without the droop, the net contribution from the controllers is not eliminated when the generator torque set point is increased, which causes the torque offset. With the droop, this offset is reduced each time the torque is increased. Eventually, when the torque set point results in sufficiently high power to reverse bias the diode bridge of the load, the offset is completely removed, and the DC-voltage control ensures only balanced converter buses.

From the comparison of load case 1 with- and without the torque-based DC-voltage control, it can be concluded that the droop function is according to the control synthesis, Sec. 4.3.3, and simulations, Sec. 5.2.4. Thus, it is a necessary part of the modular control system.

6.2.5 Concluding remarks for the simulation model verification

The results obtained for the laboratory setup with resistive DC load have been compared to a corresponding simulation model in PSCAD. The main principles from the experiments have been recreated in the simulations. Both short transients due to the PI control response, overdetermined operation and longer torque- and speed-ramps have been simulated with results that coincide well with those obtained experimentally. There are only some minor differences observed, in the DC-voltage amplitudes for the variable load cases. These differences are due to an ideal load model. It is therefore possible to conclude that there is sufficient

similarity between the experimental setup and the laboratory simulation model.

Since the laboratory setup simulation model and the full systems simulation model in Chapter 5) are in principle equal, except for voltage- and power-level, the verification can be extrapolated to also include the full simulation model.

6.3 Experimental results with active DC load

In this section, the results are obtained with a fixed DC-link voltage. A converter connected to the 400 V laboratory grid, via a variable transformer, is utilized to emulate the externally controlled DC-link, Fig. 6.10(a). The converter is set to maintain the DC-link voltage to a constant value of 300 V (DC), i.e. 100 V per module. This configuration of the laboratory setup was used to verify the response to a step in the torque reference, and operation with the converter units in overmodulation. Additionally, the controlled DC load is capable of handling higher power than the resistive load. This made it possible to test the system for higher loading. Finally, the fault-tolerant control is verified.

All results are obtained with the DC-voltage droop control active.

Description of the grid connected converter - active DC load

The controlled DC-link voltage is provided by a 60 kVA converter connected to the 400 V laboratory grid via a variable transformer [139][5]. The transformer is used to adjust the AC-grid voltage to match the requested DC voltage. Additionally, it provides galvanic insulation. The converter consists of a two-level, 3-phase IGBT bridge, and an LCL filter, Fig. 6.10(a). This converter is designed for laboratory use, with oversized power circuit components, and extensive protection mechanisms. The control system, Fig. 6.10(b), is implemented on the same type of FPGA-control card as as applied for the modular series connected converter control.

The angle reference for the abc/dq transform is provided by a PLL based on voltage measurements at the AC-filter capacitors. This PLL uses a frequency difference feedback loop to enhance its capturing ability [135]. An active damping mechanism suppresses oscillations in the LCL filter by emulating a virtual resistor [140].

The DC-link voltage control is achieved by control of the d-axis current reference. The operation strategy is constant DC voltage. Hence, all power captured by the

[5]The description of the grid connected converter is written by Kjell Ljøkelsøy.

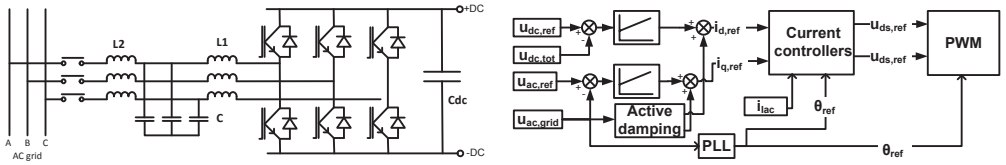

(a) (b)

Figure 6.10: a) Grid-connected converter topology b) Control system for the grid-connected converter

generator/converter is transferred back to the laboratory AC grid.

6.3.1 DC-voltage control response to a step in the torque

This section presents results which further the verification of the DC-voltage control system, linked to Sec. 5.2.3.

The DC-bus voltage control should be able to handle a step in the torque reference, if asynchronous module controllers are to be used. The controller capability to reject such a disturbance is verified by applying a step, $\Delta m_{em,ref} = 0.5$ (at n_{mech}=20 rpm). The results are presented in Fig. 6.11(a)(step-up) and Fig. 6.11(b) (step-down). This type of disturbance should be suppressed by the DC-bus voltage control system. For the step-up case, there is a small overshoot in the bus voltages. This overshoot is similar for the three converter units, and is caused by the response time of the grid-connected converter. Additionally, there is a small, initial imbalance in the voltages which is due to the asynchronous update of references in the modules. This voltage imbalance is quickly eliminated. For the step-down, Fig. 6.11(b), the time to achieve balance at the new operating point is longer than in the step-up. The reason is that there is less power flowing in the DC link, contributing to a longer charging time.

In Appendix F.3, the response to activation of DC-bus voltage control is documented for a controlled DC-link voltage. The response is similar to the corresponding response with resistive DC load.

Based on the results from this paragraph, and Sec. 6.2.3 and Sec. 6.2.4, it is verified that the DC-bus voltage control system functions in accordance with the control synthesis in Chapter 4.

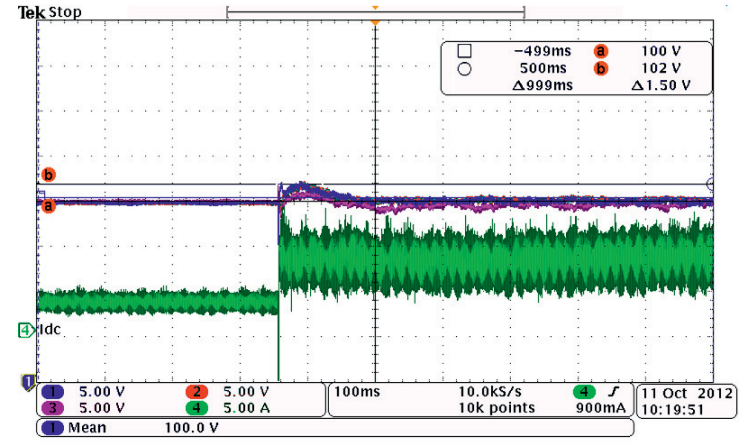

(a)

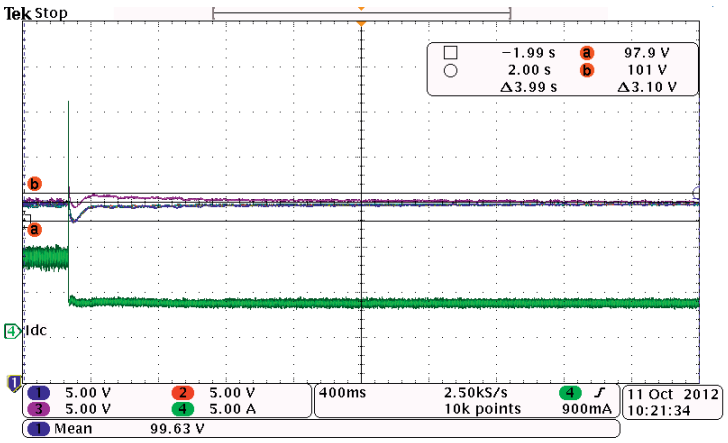

(b)

Figure 6.11: DC-bus voltage response to a torque step. $\Delta m_{em,ref} = 0.5$ pu, $n_{mech} = 20$ rpm. a) Step up from 0.2 to 0.7 pu. b) Step down from 0.7 to 0.2 pu. (Ch.1: $U_{dc,1}$, Ch.2: $U_{dc,2}$, Ch.3: $U_{dc,3}$, Ch.4: $I_{dc,link}$).

6.3.2 System response to variable load

This section relates to the system simulations in Sec. 5.3.2 .

The overall system performance is verified using high machine speed (40 rpm) and variable torque ramps as input. In Fig. 6.12(a), the torque is ramped up from 0.2 pu to 0.8 pu, via 0.5 pu. The impact on the DC-bus voltage is negligible, except for a minor increase in voltage ripple at the highest load. In Fig. 6.12(b), the torque is increased further, and the converter units are opreated in overmodulation. This overmodulation results in an increased DC-voltage ripple. However, the DC-bus

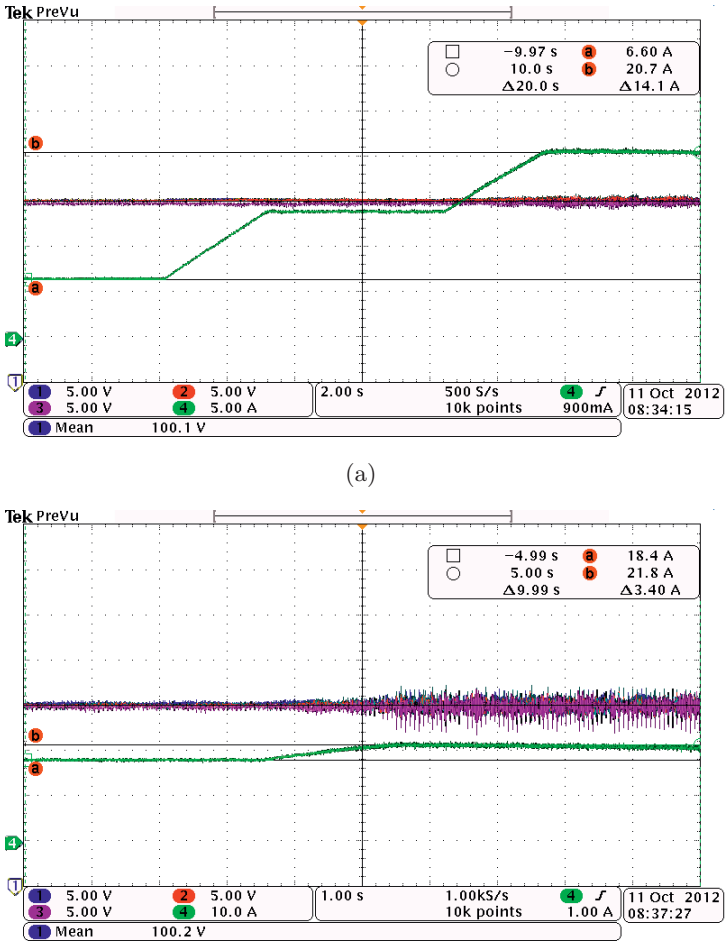

Figure 6.12: DC-bus voltage balance control under high system loading, n_{mech}=40 rpm. a) Torque ramp from 0.2-0.5-0.8 pu. b) Torque ramp from 0.7 to 0.9 pu, converter units entering overmodulation (Ch.1: $U_{dc,1}$, Ch.2: $U_{dc,2}$, Ch.3: $U_{dc,3}$, Ch.4: $I_{dc,link}$).

voltage balance control is unaffected. This response is expected, since the voltage balance should only depend on available active power capacity in the modules.

The verification that the DC-bus voltage control is also functioning in overmodulation is important for the individual module deloading control, since this relies on using the full voltage range of the converter unit. The individual module derating concept is verified in the next section.

6.4 Verification of fault-tolerant operation

The following section relates to the fault handling concepts developed in Sec. 3.5, control presented in Sec. 4.4, and transient analysis presented in Sec. 5.4.

Three cases are investigated for the verification of the fault-tolerant operation for the modular converter:

1. Operation with one of three converter units disconnected (redundant module operation).
2. Response to a trip in one converter unit during operation (fail-to-safe operation for converter unit trip).
3. Deloading control by individual DC-bus voltage reference control (overtemperature mitigation).

The full bypass operation described in Sec. 3.5.2 is not verified experimentally, due to limitations in the laboratory setup. However, the combination of the two first points above are considered sufficient for verifying the principles of a bypass.

6.4.1 Converter unit trip and redundant module operation

The redundant-module operation is verified with one module disconnected, and load case 1 (only the ramp-up part) applied, Fig. 6.13(a). Converter unit 1 is bypassed, which results in stator segment 1 not being loaded. The resistive DC load is used for this case and the two remaining modules are operated as normal. The observed behavior of the two connected converter units is the equivalent to that observed with all three modules operating in Sec. 6.2.4. Additionally, no problems caused by unevenly distributed torque were observed during the operation. Hence, it can be concluded that the system can handle redundant module operation.

The fail-to-safe operation following a converter unit trip is verified based on the results presented in Fig. 6.13(b). Converter unit 1 is tripped at a generator speed of 35 rpm and torque reference of 0.1 pu. The grid-connected converter is used as load, and set to maintain the DC-link voltage constant at 300 V. The initial part of the response is a drop in the bus voltage for module 1, and a corresponding increase in the two working modules. The freewheeling diodes are reverse biased, and the current in stator segment 1 is blocked. When $U_{dc,1}$ is sufficiently low, the tripped VSC unit starts behaving as a passive rectifier. Since the diode bridge introduces more harmonic components, the two remaining converter units experience increased voltage ripple. This ripple increase is naturally also found in the DC-link current. Continued, stable control of module 2 and 3 is still achieved.

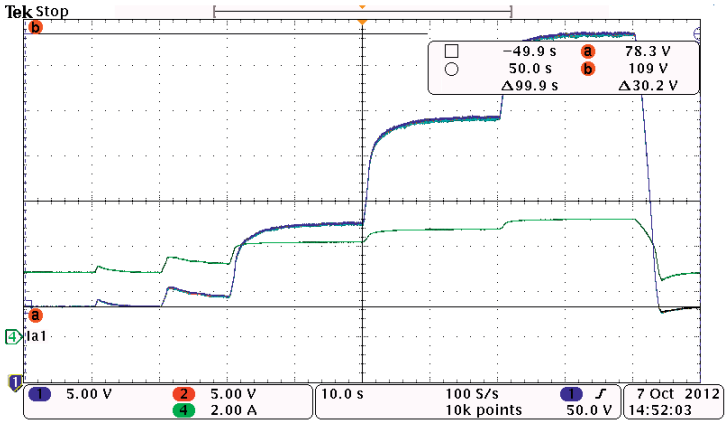

(a)

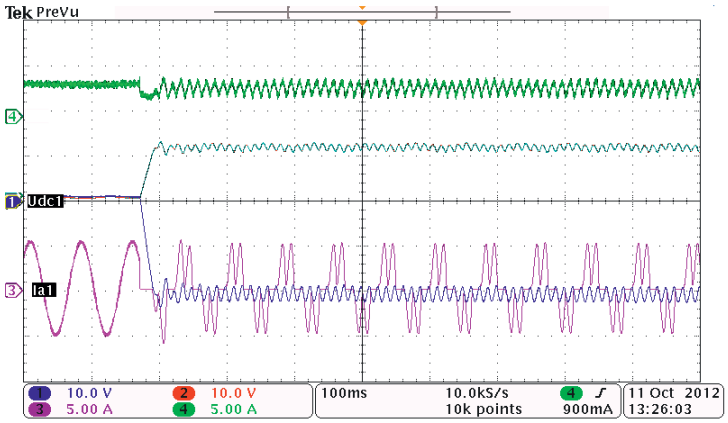

(b)

Figure 6.13: a) Variable load case 1 with module 3 disconnected, with the resistive DC load. (Ch.1: $U_{dc,1}$, Ch.2: $U_{dc,2}$, Ch.4: $I_{dc,link}$). b) Response to converter unit (1) trip with controlled DC-link voltage. $m_{em,ref}$ = 0.1 pu, n_{mech}=35 rpm.(Ch.1: $U_{dc,1}$, Ch.2: $U_{dc,2}$, Ch.3: $I_{a,1}$, Ch.4: I_{dc}).

The experimental results coincide well with the behavior of the simulated response in Sec. 5.4.1.

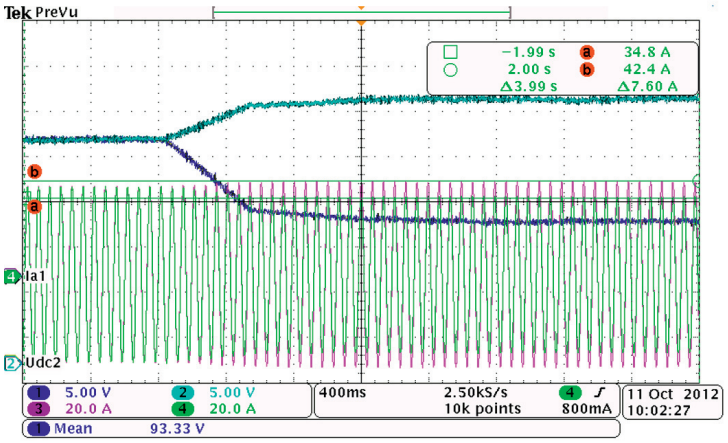

(a)

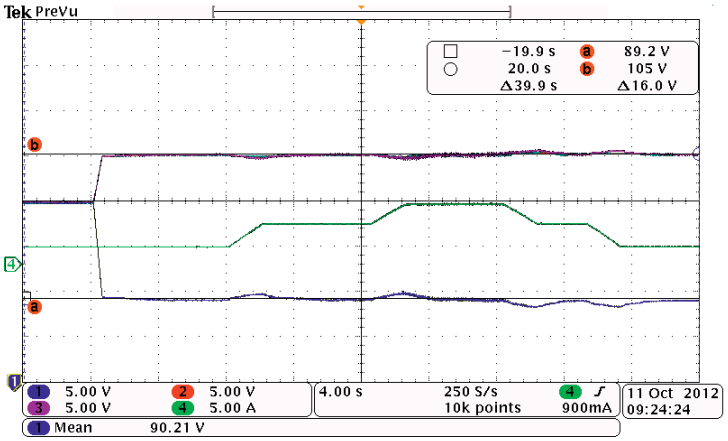

(b)

Figure 6.14: Individual module deloading control mode. $U_{dc,1,ref}$ reduced by 10%. a) Initial response to individual deloading control, n_{mech} = 40 rpm, $m_{em,ref}$ = 0.75 pu current (Ch.1: $U_{dc,1}$, Ch.2: $U_{dc,2}$, Ch.3: $I_{a,3}$, Ch.4: $I_{a,1}$). b) Torque reference ramp, n_{mech}= 20 rpm (Ch.1: $U_{dc,1}$, Ch.2: $U_{dc,2}$, Ch.3: $U_{dc,3}$, Ch.4: $I_{dc,link}$).

6.4.2 Individual module deloading for overtemperature mitigation

The possibility to apply an individual deloading control to one module through DC-bus voltage reference control is investigated theoretically in Sec. 3.5.3 and by simulations in Sec. 5.4.2. The concept is verified by the experimental results presented in Fig. 6.14(b) and Fig. 6.14(a).

The voltage reference for module 1 is decreased by 10 %, and the references for

module 2 and 3 are increased by 5 % each. Fig. 6.14(a) shows the individual module deloading control effect on the stator segment currents: The phase current in segment 1 is decreased with the converter unit DC-bus voltage, while there is a slight increase in the phase current for segment 2. In Fig. 6.14(b), the individual deloading operation is activated, and the system operation is continued. The speed is 20 rpm, and a torque ramp (0.1-0.3-0.5-0.3-0.1 pu) is applied. The continued operation does not cause problems for the fault-tolerant control mode, although there is a slightly more prominent response to torque ramps in the DC-bus voltages compared to the normal, balanced case, Fig. 6.12(a).

6.5 Summary laboratory verification

This chapter has presented the experimental results from the laboratory verification of the modular series connected converter. The results are used for a proof-of-concept verification of operation and control of the generator/converter system. Good correspondence between the experimental and simulation results is obtained.

The experimental verification is divided into several steps: First, the basic system properties, magnetic decoupling and modular control approach are verified. The impact of a DC-bus voltage control with and without the proposed droop control is demonstrated. Both step responses and variable load profiles are investigated.

Second, the system operation is verified based on variable load cases, torque-step response and overmodulation. The step in torque reference also verifieds that an asynchronous master/slave communication is feasible.

Third, the fault-tolerant control modes is verified. The fail-to-safe response to a converter unit trip is demonstrated, and it is shown that the system is capable of operating with one module disconnected. In addition, the individual module deloading control strategy is verified.

7 Conclusions and Recommendations for Further Work

7.1 Summary and concluding remarks

A modular series connected converter suitable for a transformerless offshore wind turbine is analyzed in this thesis. The main objective, which is to verify that the proposed converter system can be designed to provide a suitable interface between a modular axial flux ironless stator permanent magnet synchronous generator and a high voltage DC link is fulfilled.

The modular converter topology consists of N 3-phase voltage source converter units. Each unit is connected to an independent 3-phase winding output from the modular generator. The high output voltage is obtained by connecting the converter unit DC buses in series. This converter topology provides the necessary interface to a high voltage grid for a generator-insulation system which makes a compact, high voltage machine feasible.

A simplified model is developed for the modular generator. The model describes the ironless machine as a set of N 3-phase machine models, one for each stator segment. This simplification is possible due to weak magnetic coupling between the stator segments.

The physical properties of the modular generator/converter system are analyzed theoretically. An expression is developed, that relates converter unit DC-bus-voltage deviation between the modules and module-parameter variations. Since equal module voltages is beneficial for both converter unit stress and the machine-insulation system benefits from equal module voltages, these deviations introduce the demand for DC-bus voltage control. It is demonstrated theoretically, and by

simulations that this DC-bus voltage control may lead to derating of the turbine power capacity. This is because the compensation of differences in output power requires additional current loading in some modules. In order to avoid overloading these modules, the resulting torque, and hence power, of the turbine will have to be constrained. This derating will depend on the difference between the parameters of the weakest module and the average of all modules.

Additionally, a small-signal analysis of the DC-bus voltage stability in current-control mode revealed that the internal DC voltages of the converter chain is instable in motor mode. This instability is independent of the stability of the externally controlled DC voltage. Hence, the module DC-bus voltage control is required for stability reasons as well as for the bus-voltage control. For the generator mode, the system is self-stabilizing.

The synthesis of a modular converter control system is presented, and the validity of this approach is verified by simulations and experimental results. The core of the module controller is a standard vector current control. A DC-bus voltage control is included to provide the required control and stabilization of the internal voltage distribution between the modules. It is demonstrated, that it is possible to obtain a controller tuning which is sufficiently robust with respect to both operating conditions and parameter variations. This makes it possible to implement different control strategies without changing the internal structure of the module control units. These different control strategies can be implemented via manipulation of the DC-voltage- and turbine-torque references.

An analysis of the DC-bus voltage control system demonstrates the necessity of introducing a torque-based DC-voltage droop, since there are $N-1$ degrees of freedom and N PI controllers, and hence overdetermined. It is demonstrated by simulations, that without the droop control, the module DC-bus voltage balance control system may cause the total turbine torque to differ from the reference torque in steady state. The introduction of the DC-voltage droop removes this interference with the turbine total torque. The intention of the DC-voltage control system is to only affect the converter unit DC-bus voltages. Hence, the DC-voltage droop control is a necessary part of the modular control system. A frequency-response analysis of the droop parameters is presented, for the selection of controller parameters.

Two possibilities to implement fault tolerance for the series connected converter system are identified and analyzed. The fault-tolerant modes are 1) fail-to-safe transition for a converter unit trip followed by redundant operation, and 2) individual deloading of a single module. Assuming the DC-link voltage is being controlled externally, an analysis of the converter unit trip (fault type 1) identified the necessity of overrating the blocking voltage of the semiconductors for

$N-1$ operation, since the functioning modules will have to compensate for the voltage drop across the faulted converter unit. The introduction of redundant modules requires additional voltage overrating. The transition to the redundant mode is possible to perform without stopping the turbine. The same holds for reconnection of a falsely tripped converter unit. Individual module deloading (2) is possible to implement by active control of the DC-bus voltage deviation between modules. The concept allows for minimal turbine derating if one module experiences overloading due to local cooling system problems. Both redundancy and individual deloading control can be implemented via DC-voltage reference modification, without changing the module controllers.

The concept is verified experimentally based on a 45 kW prototype of the axial flux ironless stator permanent magnet synchronous generator with three stator segments connected to three converter units. Implementation of the control system is done in accordance with the presented, modular control synthesis. The modular control system is implemented as an embedded control, using one FPGA/processor-based control card for each module. This allowed optimal division of the control tasks between the high speed FPGA and low-speed processor. A robust, asynchronous communication is developed for the communication between the cards. The feasibility of the system, theoretical models, modular control synthesis approach for the series connected converter and the DC-droop control functionality are all verified by the experimental results. The simulation model is also validated. Finally, the fault-tolerant modes of operation, redundancy and single module deloading control are verified. The results from the experimental verification can be extrapolated to also cover the operation and control for a modular series connected converter in a 10 MW wind turbine consisting of N modules.

7.2 Recommendations for further research

The special machine-insulation technology of the 10 MW high voltage generator is a vital part in the design of a lightweight, transformerless offshore wind turbine based on the system analyzed in this thesis. This insulation system has not been analyzed in depth nor verified experimentally, and requires research. This investigation of the insulation needs to take into account the converter topology and switching frequency. Furthermore, the mechanical challenges related to such a large diameter, rim generator requires thorough analysis. The issues related to the special generator have not been addressed in this thesis, which has focused on the power electronic converter solution. It is therefore important to address these topics in further research.

The number of modules (N=9) and voltage levels (100 kV) used as exemplary numerical values in this thesis are chosen somewhat arbitrarily, to demonstrate the potential of the idea. However, as is briefly discussed in Sec. 3.2.3, these are probably not optimal. Therefore it is recommended that further research addresses the system assembly in light of the constraints of the available technologies. Such an analysis is recommend to reconsider the number of modules in relation to the generator weight and system-voltage levels. Additionally, the rated voltage- and power for the converter units need be taken into consideration, including the semiconductor blocking voltages, topology/complexity and reliability for the converter units.

In Sec. 5.3, it is demonstrated that the combination of module parameter variations and choice of control strategy is important for the actual power capacity of the turbine. A full system energy yield analysis, including the transmission losses would therefore be of interest. A comparison with more conventional turbine technologies should be part of this analysis, in order to evaluate the most suitable technology. Additionally, the control strategy will influence the loading of each converter. Hence, a complete converter loss analysis, which takes into account the control strategies for the DC-bus voltage control and variable module parameters is considered to be important for understanding the stress and cooling requirements for the converter units.

The purpose of the proposed control system is to demonstrate the feasibility of implementing a modular control system. There may be other, more optimal ways of controlling the modular converter, and it is recommended to address the control-synthesis and -structure in further research. Additionally, the effect of different modulation schemes should be investigated.

In this thesis, the analyses stopped at the DC rails of the converter, and did not consider output-filter design. Such a filter will be important for both grid integration, fault handling and control system. The DC-grid filter will be a topic of interest for both the transformerless technology presented here, and other DC-grid connected wind turbines. It is further recommended that the investigation on DC filters include modeling of DC-grid cables - to identify a suitable model that provides a sufficiently accurate response for high frequency phenomena.

An assumption for the thesis is that the turbine output-voltage is controlled elsewhere in the grid, by a central converter unit. This may not necessarily be the best solution for operation of a wind farm. Control of the DC voltage locally, on each turbine, may be a more beneficial solution in certain situations. Since this results in multiple turbines interacting via the same voltage, load-sharing control by a DC-link voltage droop is required. Different turbine control strategies should be evaluated with respect to voltage stability robustness, grid integration issues

and wind farm power capture.

The benefit of introducing phase shifts between modules for harmonic cancellation is of interest. This phase shift may be utilized for elimination of harmonic components in the torque, and in the resulting DC-output from the turbine. This may be of special importance in the case of medium voltage converters with low switching frequencies. The benefit of this phase shift should be evaluated against the possibly more complex machine and control structure.

Finally, the DC-grid fault handling is important for the modular series connected converter, which has the capacitor banks directly exposed to the grid. Some different alternatives were identified in Sec. 3.5, but not pursued further. An efficient protection, developed for the power levels relevant for a wind turbine, towards short circuits is imperative if the transformerless turbine technology addressed in this thesis is to be implemented.

References

[1] Intergovernmental Panel on Climate Change (IPCC), *Climate Change 2007 The Physical Science Basis*. Cambridge University Press 32 Avenue of the Americas, New York, NY 10013-2473, USA, 20007.

[2] International Energy Agency (IEA), "www.iea.org/publications/ scenariosandprojections." -accssed May 28, 2013.

[3] International Energy Agency (IEA), "World Energy Outlook 2011," tech. rep., Available at www.iea.org, 2011.

[4] International Energy Agency (IEA), "Energy Markets by Technology," tech. rep., Available at www.iea.org, 2011.

[5] www.newscientist.com, "Wind power is now cheaper than coal in some countries." www.newscientist.com/article/dn23159-wind-power-is-now-cheaper-than-coal-in-some-countries.html, Accessed Feb. 2013.

[6] A. Henderson, C. Morgan, B. Smith, H. Sorensen, R. Barthelmie, and B. Boesmans, "Offshore Wind Energy in Europe A Review of the State-of-the-Art," *Wind Energy*, vol. 6, no. 1, pp. 35–52, 2003.

[7] M. Kuhn, W. Bierbooms, G. van Bussel, M. Ferguson, B. Goransson, T. Cockerill, R. Harrison, and W. R. Harland, L. Vugts JH, "Opti-OWECS; Structural and Economic Optimisation of Bottom Mounted Offshore Wind Energy Convertors. JOULE III Project, Vol.0," tech. rep., Delt University of Technology, Delft, 1998.

[8] P. Jamieson, *Innovation in Wind Turbine Design*, ch. Upscaling of Wind Turbine Systems, pp. 75–104. John Wiley & Sons, Ltd, 2011.

[9] O. Dalhaug, P. Berthelsen, T. Kvamsdal, L. Froyd, S. Gjerde, Z. Zhang, K. Cox, E. Van Buren, and D. Zwick, "Specification of the NOWITECH 10 MW Reference Wind Turbine," tech. rep., Norwegian Research Centre for Offshore Wind Technology, NOWITECH, Trondheim, Norway, 2012.

[10] K. Ma, F. Blaabjerg, and M. Liserre, "Thermal analysis of multilevel grid side converters for 10 MW wind turbines under Low Voltage Ride Through," in *Energy Conversion Congress and Exposition (ECCE), 2011 IEEE*, pp. 2117–2124, 2011.

[11] J. Wang, R. Qu, and Y. Liu, "Comparison Study of Superconducting Generators With Multiphase Armature Windings for Large-Scale Direct-Drive Wind Turbines," *Applied Superconductivity, IEEE Transactions on*, vol. 23, no. 3, pp. 5201005–5201005, 2013.

[12] Siemens, "Press release: Siemens starts operating its first 6 megawatt wind turbine." www.siemens.co.uk, Accessed Sept. 2011.

[13] Vestas, "Press release: A new era for offshore wind power Presenting Vestas V164 7.0 MW Turbine for Offshore Power Plants." www.vestas.com, Accessed Mar. 2011.

[14] Enercon, "ENERCON news: ENERCON installs world's most powerful wind energy converter E-126/7.5 MW." www.enercon.de, Accsessed Jan. 2011.

[15] EWEA, "Oceans of Opportunity - Harnessing Europe's largest domestic energy resource." Available at www.ewea.org, Sept. 2009.

[16] Z. Zhang, A. Matveev, S. Ovrebo, R. Nilssen, and A. Nysveen, "State of the art in generator technology for offshore wind energy conversion systems," in *Electric Machines Drives Conference (IEMDC), 2011 IEEE International*, pp. 1131 –1136, May 2011.

[17] A. Faulstich, J. Stinke, and F. Wittwer, "Medium voltage converter for permanent magnet wind power generators up to 5 MW," in *Power Electronics and Applications, 2005 European Conference on*, pp. 9 pp.–p.9, 2005.

[18] E. Borgen, "Introduction of the Sway Turbine ST10," in *IQPC 3rd International Conference on Drivetrain Concepts for Wind Turbines*, 2012.

[19] Garrad Hassan & Partners United Kingdom, Tractebel Energy Engineering Belgium, Riso National Laboratory Denmark, Kvaerner Oil & Gas United Kingdom, Energi & Miljoe Undersoegelser (EMU) Denmark, "Offshore Wind Energy Ready to Power a Sustainable Europe," tech. rep., Delft University Wind Energy Research Institute (Duwind), 2001.

[20] B. Hahn, M. Durstewitz, and K. Rohrig, "Reliability of wind turbines," *Wind Energy*, pp. 329–332, 2007.

[21] M. Boettcher and F. Fuchs, "Power electronic converters in wind energy systems - Considerations of reliability and strategies for increasing avail-

ability," in *Power Electronics and Applications (EPE 2011), Proceedings of the 2011-14th European Conference on*, pp. 1 –10, Sept. 2011.

[22] G. van Bussel, "Offshore Wind Energy, the Reliability Dilemma," in *Proceedings of the International Conference, Berlin, Germany*, Jul. 2012.

[23] H. Polinder, H. Lendenmann, R. Chin, and W. Arshad, "Fault tolerant generator systems for wind turbines," in *Electric Machines and Drives Conference, 2009. IEMDC '09. IEEE International*, pp. 675 –681, May 2009.

[24] T. Halkosaari, "Speed Sensorless Vector Control of a Redundant Permanent Magnet Wind Power Generator," in *Industrial Electronics, 2007. ISIE 2007. IEEE International Symposium on*, pp. 2595 –2600, June 2007.

[25] N. B. Negra, J. Todorovic, and T. Ackermann, "Loss evaluation of HVAC and HVDC transmission solutions for large offshore wind farms," *Electric Power Systems Research*, vol. 76, no. 11, pp. 916 – 927, 2006.

[26] C. Meyer, *Key Components for Future Offshore DC Grids*. PhD thesis, Rheinisch-Westfalische Technische Hochschule Aachen, RWTH Aachen University, 2007.

[27] C. Meyer, M. Hoing, A. Peterson, and R. De Doncker, "Control and Design of DC Grids for Offshore Wind Farms," *Industry Applications, IEEE Transactions on*, vol. 43, pp. 1475 –1482, Nov.-Dec. 2007.

[28] W. Tang and R. Lasseter, "An LVDC industrial power distribution system without central control unit," in *Power Electronics Specialists Conference, 2000. PESC 00. 2000 IEEE 31st Annual*, vol. 2, pp. 979 –984 vol.2, 2000.

[29] P. Karlsson and J. Svensson, "DC bus voltage control for a distributed power system," *Power Electronics, IEEE Transactions on*, vol. 18, pp. 1405 – 1412, Nov. 2003.

[30] L. Max, *Energy Evaluation for DC/DC Converters in DC-Based Wind Farms*. PhD thesis, Thesis for the Degree of Licentiate of Engineering, Chalmers University of Technology, 2007.

[31] W. Chen, A. Q. Huang, C. Li, G. Wang, and W. Gu, "Analysis and Comparison of Medium Voltage High Power DC/DC Converters for Offshore Wind Energy Systems," *Power Electronics, IEEE Transactions on*, vol. 28, pp. 2014 –2023, April 2013.

[32] J. Robinson, D. Jovcic, and G. Jooos, "Analysis and Design of an Offshore Wind Farm Using a MV DC Grid," *Power Delivery, IEEE Transactions on*, vol. 25, pp. 2164 –2173, Oct. 2010.

[33] A. Prasai, J.-S. Yim, D. Divan, A. Bendre, and S.-K. Sul, "A New Architecture for Offshore Wind Farms," *Power Electronics, IEEE Transactions on*, vol. 23, pp. 1198 –1204, May 2008.

[34] A. Garces and M. Molinas, "High Frequency Wind Energy Conversion from the Ocean," in *Power Electronics Conference (IPEC), 2010 International*, pp. 2056 –2061, June 2010.

[35] A. Mogstad, M. Molinas, P. Olsen, and R. Nilsen, "A Power Conversion System for Offshore Wind Parks," in *Industrial Electronics, 2008. IECON 2008. 34th Annual Conference of IEEE*, pp. 2106 –2112, Nov. 2008.

[36] M. Carmeli, F. Castelli-Dezza, G. Marchegiani, M. Mauri, and D. Rosati, "Design and analysis of a Medium Voltage DC wind farm with a transformerless wind turbine generator," in *Electrical Machines (ICEM), 2010 XIX International Conference on*, pp. 1 –6, Sept. 2010.

[37] Z. Chen, J. Guerrero, and F. Blaabjerg, "A Review of the State of the Art of Power Electronics for Wind Turbines," *Power Electronics, IEEE Transactions on*, vol. 24, pp. 1859 –1875, Aug. 2009.

[38] R. Pena, J. Clare, and G. Asher, "Doubly fed induction generator using back-to-back PWM converters and its application to variable-speed wind-energy generation," *Electric Power Applications, IEE Proceedings* -, vol. 143, pp. 231 –241, May 1996.

[39] Y. Tang and L. Xu, "Stator field oriented control of doubly-excited induction machine in wind power generating system," in *Circuits and Systems, 1992., Proceedings of the 35th Midwest Symposium on*, pp. 1446 –1449 vol.2, Aug. 1992.

[40] S. Muller, M. Deicke, and R. De Doncker, "Doubly fed induction generator systems for wind turbines," *Industry Applications Magazine, IEEE*, vol. 8, pp. 26 –33, May/June 2002.

[41] S. Seman, J. Niiranen, and A. Arkkio, "Ride-Through Analysis of Doubly Fed Induction Wind-Power Generator Under Unsymmetrical Network Disturbance," *Power Systems, IEEE Transactions on*, vol. 21, pp. 1782 –1789, Nov. 2006.

[42] J. Morren and S. de Haan, "Ridethrough of wind turbines with doubly-fed induction generator during a voltage dip," *Energy Conversion, IEEE Transactions on*, vol. 20, pp. 435 – 441, June 2005.

[43] C. Feltes, H. Wrede, F. Koch, and I. Erlich, "Enhanced Fault Ride-Through Method for Wind Farms Connected to the Grid Through VSC-Based HVDC

Transmission," *Power Systems, IEEE Transactions on*, vol. 24, pp. 1537 – 1546, Aug. 2009.

[44] S. Engelhardt, I. Erlich, C. Feltes, J. Kretschmann, and F. Shewarega, "Reactive power capability of wind turbines based on doubly fed induction generators," *Energy Conversion, IEEE Transactions on*, vol. 26, pp. 364 –372, march 2011.

[45] R. Cotrell, "A preliminary evaluation of a multiple-generator drivetrain configuration for wind turbines," in *Proc. 16th Annu. IEEE APEC Conf.,2001, vol.1, pp.628-634*, 2001.

[46] H. Polinder, F. van der Pijl, G.-J. de Vilder, and P. Tavner, "Comparison of direct-drive and geared generator concepts for wind turbines," *Energy Conversion, IEEE Transactions on*, vol. 21, pp. 725 –733, sept. 2006.

[47] W. Li, C. Abbey, and G. Joos, "Control and performance of wind turbine generators based on permanent magnet synchronous machines feeding a diode rectifier," in *Power Electronics Specialists Conference, 2006. PESC '06. 37th IEEE*, pp. 1 –6, june 2006.

[48] H. Geng and D. Xu, "Stability analysis and improvements for variable-speed multipole permanent magnet synchronous generator-based wind energy conversion system," *Sustainable Energy, IEEE Transactions on*, vol. 2, pp. 459 –467, oct. 2011.

[49] A. Hansen and G. Michalke, "Multi-pole permanent magnet synchronous generator wind turbines' grid support capability in uninterrupted operation during grid faults," *Renewable Power Generation, IET*, vol. 3, pp. 333 –348, sept. 2009.

[50] K.-H. Kim, Y.-C. Jeung, D.-C. Lee, and H.-G. Kim, "LVRT Scheme of PMSG Wind Power Systems Based on Feedback Linearization," *Power Electronics, IEEE Transactions on*, vol. 27, pp. 2376 –2384, may 2012.

[51] E. Spooner and A. Williamson, "Direct coupled, permanent magnet generators for wind turbine applications," *Electric Power Applications, IEE Proceedings* -, vol. 143, pp. 1 –8, jan 1996.

[52] M. Chinchilla, S. Arnaltes, and J. Burgos, "Control of permanent-magnet generators applied to variable-speed wind-energy systems connected to the grid," *Energy Conversion, IEEE Transactions on*, vol. 21, pp. 130 – 135, march 2006.

[53] S. Siegfriedsen and G. Bohmeke, "Multibrid technology - a significant step to multi-megawatt wind turbines," *Wind Energy*, vol. 1, issue 2, pp. 89–100, 1998.

[54] ArevaWind, "Offshore Windpower M5000." Datasheet available at www.arewa-wind.com, May 2011.

[55] H. Li, Z. Chen, and H. Polinder, "Optimization of multibrid permanent-magnet wind generator systems," *Energy Conversion, IEEE Transactions on*, vol. 24, pp. 82 –92, march 2009.

[56] Z. Xu, R. Li, H. Zhu, D. Xu, and C. Zhang, "Control of Parallel Multiple Converters for Direct-Drive Permanent-Magnet Wind Power Generation Systems," *Power Electronics, IEEE Transactions on*, vol. 27, pp. 1259 –1270, march 2012.

[57] G. Raina and O. P. Malik, "Variable Speed Wind Energy Conversion Using Synchronous Machine," *Aerospace and Electronic Systems, IEEE Transactions on*, vol. AES-21, no. 1, pp. 100–105, 1985.

[58] A. Ragheb and M. Ragheb, "Wind turbine gearbox technologies," in *Nuclear Renewable Energy Conference (INREC), 2010 1st International*, pp. 1 –8, march 2010.

[59] A. McDonald, M. Mueller, and H. Polinder, "Structural mass in direct-drive permanent magnet electrical generators," *Renewable Power Generation, IET*, vol. 2, pp. 3 –15, march 2008.

[60] F. Idland, R. Haug, and S. Overbo, "Electrical Machine and Method for the Manufacturing of Stator Sections Therefor," 2010.

[61] P. Olsen, S. Gjerde, R. Nilssen, J. Hoelto, and S. Hvidsten, "A Transformerless Generator-Converter Concept making feasible a 100 kV Light Weight Offshore Wind Turbine: Part I - The Generator," in *Energy Conversion Congress and Exposition (ECCE), 2012 IEEE*, pp. 247 –252, Sept. 2012.

[62] M. Parker, C. Ng, and L. Ran, "Fault-tolerant control for a modular generator - converter scheme for direct-drive wind turbines," *Industrial Electronics, IEEE Transactions on*, vol. 58, no. 1, pp. 305–315, 2011.

[63] C. Ng, M. Parker, L. Ran, P. Tavner, J. Bumby, and E. Spooner, "A multilevel modular converter for a large, light weight wind turbine generator," *Power Electronics, IEEE Transactions on*, vol. 23, pp. 1062 –1074, May 2008.

[64] E. Spooner, P. Gordon, J. Bumby, and C. French, "Lightweight ironless-stator pm generators for direct-drive wind turbines," *Electric Power Applications, IEE Proceedings* -, vol. 152, no. 1, pp. 17–26, 2005.

[65] M. Parker, C. Ng, L. Ran, P. Tavner, and E. Spooner, "Power Control of Direct Drive Wind Turbine with Simplified Conversion Stage Transformerless Grid Interface," in *Universities Power Engineering Conference, 2006. UPEC '06. Proceedings of the 41st International*, vol. 1, pp. 65 –68, sept. 2006.

[66] M. Parker, L. Ran, and S. Finney, "Distributed control of a fault-tolerant modular multilevel inverter for direct-drive wind turbine grid interfacing," *Industrial Electronics, IEEE Transactions on*, vol. 60, no. 2, pp. 509–522, 2013.

[67] X. Yuan, Y. Li, J. Chai, and M. Ma, "A Modular Direct-Drive Permanent Magnet Wind Generator System eliminating the Grid-side Transformer," in *Power Electronics and Applications, 2009. EPE '09. 13th European Conference on*, pp. 1 –7, Sept. 2009.

[68] X. Yuan, Y. Li, and J. Chai, "A transformerless modular permanent magnet wind generator system with minimum generator coils," in *Applied Power Electronics Conference and Exposition (APEC), 2010 Twenty-Fifth Annual IEEE*, pp. 2104 –2110, feb. 2010.

[69] X. Yuan, J. Chai, and Y. Li, "A Transformer-Less High-Power Converter for Large Permanent Magnet Wind Generator Systems," *Sustainable Energy, IEEE Transactions on*, vol. 3, pp. 318 –329, july 2012.

[70] F. Deng and Z. Chen, "A New Structure Based on Cascaded Multilevel Converter for Variable Speed Wind Turbine," in *IECON 2010 - 36th Annual Conference on IEEE Industrial Electronics Society*, pp. 3167 –3172, nov. 2010.

[71] P. Maibach, M. Eichler, and P. Steimer, "Energy System, US2009/0212568 A1," 2009.

[72] M. Dahgren, H. Frank, M. Leijon, F. Owman, and L. Walfridsson, "$Windformer^{TM}$: Wind power goes large-scale," in *ABB Review, No.3*, 2000.

[73] ABB Power Technologies, "HVDC Light -The worlds first HVDC Light offshore converter." www.abb.com, 2004.

[74] R. O'Donnell, N. Schofield, A. Smith, and J. Cullen, "Design Concepts for High-Voltage Variable-Capacitance DC Generators," *Industry Applications, IEEE Transactions on*, vol. 45, pp. 1778 –1784, sept.-oct. 2009.

[75] M. S. Carmeli, F. Castelli-Dezza, D. Rosati, G. Marchegiani, and M. Mauri, "MVDC connection of offshore wind farms to the transmission system," in *Power Electronics Electrical Drives Automation and Motion (SPEEDAM), 2010 International Symposium on*, pp. 1201–1206, 2010.

[76] F. Caricchi, F. Crescimbini, O. Honorzti, G. Lo Bianco, and E. Santini, "Performance of coreless-winding axial-flux permanent-magnet generator with power output at 400 Hz-3000 rev/min," in *Industry Applications Conference, 1997. Thirty-Second IAS Annual Meeting, IAS '97., Conference Record of the 1997 IEEE*, vol. 1, pp. 61–66 vol.1, 1997.

[77] J. Bumby and R. Martin, "Axial-flux permanent-magnet air-cored generator for small-scale wind turbines," *Electric Power Applications, IEE Proceedings*, vol. 152, no. 5, pp. 1065–1075, Sept.

[78] P. Olsen and SmartMotor AS, "Energiomformingssystem, pub. no: No 2011/0018, intl pat pending," 2011.

[79] H. Buhler, *Reglage de Systemes d'Electronique de Puissance*. Presses Polytechniques et Universitaires de Lausanne, 1997.

[80] M. Chinchilla, S. Arnalte, J. Burgos, and J. Rodriguez, "Power limits of grid connected modern wind energy systems," *Renewable Energy*, vol. 31, no. 9, pp. 1455 – 1470, 2006.

[81] Sihler, C. and General Electric, "Modular Stacked Power Converter Vessel US 2011/049060," 2012.

[82] B. Backlund, M. Rahimo, S. Klaka, and J. Siefken, "Topologies, voltage ratings and state of the art high power semiconductor devices for medium voltage wind energy conversion," in *Power Electronics and Machines in Wind Applications, 2009. PEMWA 2009. IEEE*, pp. 1 –6, June 2009.

[83] T. Iversen, S. Gjerde, and T. Undeland, "Multilevel Converters for a 10 MW, 100 kV Transformer-less Offshore Wind Generator system," in *EPE Joint Wind Energy and T&D Chapters Seminar*, 2012.

[84] A. Lesnicar and R. Marquardt, "An innovative modular multilevel converter topology suitable for a wide power range," in *Power Tech Conference Proceedings, 2003 IEEE Bologna*, vol. 3, p. 6 pp. Vol.3, June 2003.

[85] B. Jacobson, P. Karlsson, G. Asplund, L. Harnefors, and T. Jonsson, "VSC-HVDC Transmission with Cascaded Two-Level Converters," in *CIGRE SC B4 Session*, 2010.

[86] N. Mohan, T. Undeland, and W. Robbins, *Power Electronics - Converters, Applications, and Design Third Edition*. John Wiley & Sons, Inc., 2003.

[87] D. Gritter, S. Kalsi, and N. Henderson, "Variable speed electric drive options for electric ships," in *Electric Ship Technologies Symposium, 2005 IEEE*, pp. 347–354, 2005.

[88] R. Teichmann, M. Malinowski, and S. Bernet, "Evaluation of three-level rectifiers for low-voltage utility applications," *Industrial Electronics, IEEE Transactions on*, vol. 52, no. 2, pp. 471–481, 2005.

[89] D. Krug, M. Malinowski, and S. Bernet, "Design and comparison of medium voltage multi-level converters for industry applications," in *Industry Applications Conference, 2004. 39th IAS Annual Meeting. Conference Record of the 2004 IEEE*, vol. 2, pp. 781–790 vol.2, 2004.

[90] J. Rodriguez, B. Wu, S. Bernet, N. Zargari, J. Rebolledo, J. Pontt, and P. Steimer, "Design and Evaluation Criteria for High Power Drives," in *Industry Applications Society Annual Meeting, 2008. IAS '08. IEEE*, pp. 1–9, 2008.

[91] J. C. G. Wheeler, "Effects of converter pulses on the electrical insulation in low and medium voltage motors," *Electrical Insulation Magazine, IEEE*, vol. 21, no. 2, pp. 22–29, 2005.

[92] J. Sayago, T. Bruckner, and S. Bernet, "How to Select the System Voltage of MV Drives - A Comparison of Semiconductor Expenses," *Industrial Electronics, IEEE Transactions on*, vol. 55, no. 9, pp. 3381–3390, 2008.

[93] H. Mirzaee, A. De, A. Tripathi, and S. Bhattacharya, "Design comparison of high power medium-voltage converters based on 6.5kV Si-IGBT/Si-PiN diode, 6.5kV Si-IGBT/SiC-JBS diode, and 10kV SiC MOSFET/SiC-JBS diode," in *Energy Conversion Congress and Exposition (ECCE), 2011 IEEE*, pp. 2421–2428, 2011.

[94] I. Abuishmais, *SiC Power Diodes and Juntion Field-Effect Transistors*. PhD thesis, Norwegian University of Science and Technology, NTNU, 2012.

[95] N. Bianchi, S. Bolognani, and M. Zigliotto, "Analysis of PM synchronous motor drive failures during flux weakening operation," in *Power Electronics Specialists Conference, 1996. PESC '96 Record., 27th Annual IEEE*, vol. 2, pp. 1542 –1548 vol.2, June 1996.

[96] B. Welchko, T. Jahns, and S. Hiti, "IPM synchronous machine drive response to a single-phase open circuit fault," *Power Electronics, IEEE Transactions on*, vol. 17, pp. 764 – 771, Sept. 2002.

[97] B. Welchko, T. Jahns, W. Soong, and J. Nagashima, "IPM synchronous machine drive response to symmetrical and asymmetrical short circuit faults," *Energy Conversion, IEEE Transactions on*, vol. 18, pp. 291 – 298, June 2003.

[98] B. Welchko, T. Jahns, and T. Lipo, "Short-circuit fault mitigation methods for interior PM synchronous machine drives using six-leg inverters," in *Power Electronics Specialists Conference, 2004. PESC 04. 2004 IEEE 35th Annual*, vol. 3, pp. 2133 – 2139 Vol.3, June 2004.

[99] B. Welchko, J. Wai, T. Jahns, and T. Lipo, "Magnet-flux-nulling control of interior PM Machine drives for improved steady-state response to short-circuit faults," *Industry Applications, IEEE Transactions on*, vol. 42, pp. 113 – 120, Jan.-Feb. 2006.

[100] National Grid Electricity Transmission, UK, "THE GRID CODE - Issue 5, Revision 1," tech. rep., Available at: http://www.nationalgrid.com/uk/Electricity/Codes/, 2012.

[101] O. Giddani, G. Adam, O. Anaya-Lara, G. Burt, and K. Lo, "Control strategies of VSC-HVDC transmission system for wind power integration to meet GB grid code requirements," in *Power Electronics Electrical Drives Automation and Motion (SPEEDAM), 2010 International Symposium on*, pp. 385 –390, June 2010.

[102] J. Yang, J. Fletcher, and J. O'Reilly, "Multi-terminal DC wind farm collection and transmission system internal fault analysis," in *Industrial Electronics (ISIE), 2010 IEEE International Symposium on*, pp. 2437 –2442, July 2010.

[103] J. Yang, J. Fletcher, and J. O'Reilly, "Short-Circuit and Ground Fault Analyses and Location in VSC-Based DC Network Cables," *Industrial Electronics, IEEE Transactions on*, vol. 59, pp. 3827 –3837, Oct. 2012.

[104] C. Meyer, S. Schroder, and R. De Doncker, "Solid-state circuit breakers and current limiters for medium-voltage systems having distributed power systems," *Power Electronics, IEEE Transactions on*, vol. 19, pp. 1333 – 1340, Sept. 2004.

[105] C. Franck, "HVDC Circuit Breakers: A Review Identifying Future Research Needs," *Power Delivery, IEEE Transactions on*, vol. 26, pp. 998 –1007, April 2011.

[106] Z. Xu, B. Zhang, S. Sirisukprasert, X. Zhou, and A. Huang, "The emitter turn-off thyristor-based DC circuit breaker," in *Power Engineering Society Winter Meeting, 2002. IEEE*, vol. 1, pp. 288 – 293 vol.1, 2002.

[107] Q. Chen, K. Tan, and A. Huang, "Self-power emitter turn-off thyristor (SPETO) based circuit breaker for power distribution system," in *Energy Conversion Congress and Exposition (ECCE), 2012 IEEE*, pp. 2017 –2021, Sept. 2012.

[108] M. Callavik, A. Blomberg, J. Hafner, and B. Jacobson, "The Hybrid HVDC Breaker An innovation breakthrough enabling reliable HVDC grids." ABB White Paper. Available at: www.new.abb.com, October 2012.

[109] F. Deng and Z. Chen, "Design of Protective Inductors for HVDC Transmission Line Within DC Grid Offshore Wind Farms," *Power Delivery, IEEE Transactions on*, vol. 28, pp. 75 –83, Jan. 2013.

[110] A. Emadi, A. Khaligh, C. Rivetta, and G. Williamson, "Constant Power Loads and Negative Impedance Instability in Automotive Systems: Definition, Modeling, Stability, and Control of Power Electronic Converters and Motor Drives," *Vehicular Technology, IEEE Transactions on*, vol. 55, pp. 1112 –1125, July 2006.

[111] T. M. Jahns, "Flux-Weakening Regime Operation of an Interior Permanent-Magnet Synchronous Motor Drive," *Industry Applications, IEEE Transactions on*, vol. IA-23, pp. 681 –689, July 1987.

[112] J.-J. Chen and K.-P. Chin, "Minimum copper loss flux-weakening control of surface mounted permanent magnet synchronous motors," *Power Electronics, IEEE Transactions on*, vol. 18, pp. 929 – 936, July 2003.

[113] D. Maric, S. Hiti, C. Stancu, J. Nagashima, and D. Rutledge, "Two flux weakening schemes for surface-mounted permanent-magnet synchronous drives. design and transient response considerations," in *Industrial Electronics, 1999. ISIE '99. Proceedings of the IEEE International Symposium on*, vol. 2, pp. 673 –678 vol.2, 1999.

[114] A. Miller, E. Muljadi, and D. Zinger, "A variable speed wind turbine power control," *Energy Conversion, IEEE Transactions on*, vol. 12, pp. 181 –186, June 1997.

[115] T. Thiringer and J. Linders, "Control by variable rotor speed of a fixed-pitch wind turbine operating in a wide speed range," *Energy Conversion, IEEE Transactions on*, vol. 8, pp. 520 –526, Sept. 1993.

[116] G. Abad, J. Lopez, M. Rodriguez, L. Marroyo, and G. Iwanski, *Doubly Fed Induction Machine: Modeling and Control for Wind Energy Generation Applications* . Wiley-IEEE Press, 2011.

[117] L.-R. Chang-Chien and Y.-C. Yin, "Strategies for operating wind power in a similar manner of conventional power plant," *Energy Conversion, IEEE Transactions on*, vol. 24, pp. 926 –934, Dec. 2009.

[118] J. Kristoffersen, "The horns rev wind farm and the operational experience with the wind farm main controller," in *Copenhagen Offshore Wind 26-28 October 2005*, 2005.

[119] P. Kundur, *Power System Stability and Control*. McGraw-Hill,inc, 1993.

[120] L. Xu, B. Williams, and L. Yao, "Multi-terminal DC transmission systems for connecting large offshore wind farms," in *Power and Energy Society General Meeting - Conversion and Delivery of Electrical Energy in the 21st Century, 2008 IEEE*, pp. 1 –7, July 2008.

[121] T. Haileselassie and K. Uhlen, "Precise control of power flow in multiterminal VSC-HVDCs using DC voltage droop control," in *Power and Energy Society General Meeting, 2012 IEEE*, pp. 1–9, 2012.

[122] G. Holmes and T. Lipo, *Pulse Width Modulation for Power Converters - Principle and Practice*. Wiley John & Sons INC. Publication, 2003.

[123] R. Burgos, P. Kshirsagar, A. Lidozzi, F. Wang, and D. Boroyevich, "Mathematical Model and Control Design for Sensorless Vector Control of Permanent Magnet Synchronous Machines," in *Computers in Power Electronics, 2006. COMPEL '06. IEEE Workshops on*, pp. 76 –82, July 2006.

[124] Manitoba Research Centre, "PSCAD Manual." www.pscad.com.

[125] P. Anderson and A. Bose, "Stability Simulation Of Wind Turbine Systems," *Power Apparatus and Systems, IEEE Transactions on*, vol. PAS-102, pp. 3791 –3795, Dec. 1983.

[126] A. Murdoch, J. Winkelman, S. Javid, and R. Barton, "Control Design and Performance Analysis of a 6 MW Wind Turbine-Generator," *Power Apparatus and Systems, IEEE Transactions on*, vol. PAS-102, pp. 1340 –1347, May 1983.

[127] SmartMotor, *www.smartmotor.no*.

[128] H. Kolstad and K. Ljokelsoy, "SINTEF report An 01.12.12: 20 kW IGBT omformer. Beskrivelse. 3.utgave (Norwegian)," tech. rep., Sintef Energy, 2002.

[129] Semikron, "SKM 400 GB 125D. 400 A 1200 V fast IGBT." Datasheet available at: www.semikron.com, 2007.

[130] K. Ljokelsoy, "FPGA based processor board for control of power electronics converters," tech. rep., SINTEF Energy Research, 2008.

[131] Xilinx, "Virtex-5 FX30T PowerPC 440," tech. rep., Datasheet available at www.xilinx.com, 2009.

[132] Xilinx, "UG011: PowerPC Processor Reference Guide." Datasheet available at www.xilinx.com, 2010.

[133] DRIVECOM Nutzergruppe e.V., "Profile 22: Drive Engineering/Servo," tech. rep., Documentation available at www.drivecom.org, 1994.

[134] Xilinx, "XPS External Peripheral Controller (EPC) v1.02a." Datasheet available at www.xilinx.com.

[135] J. Suul, K. Ljokelsoy, and T. Undeland, "Design, Tuning and Testing of a Flexible PLL for Grid Synchronization of Three-Phase Power Converters," in *Power Electronics and Applications, 2009. EPE '09. 13th European Conference on*, pp. 1 –10, Sept. 2009.

[136] LEM Current Sensor, "LF 205-S (Series: LF)." Datasheet available at: www.lem.com.

[137] LEM Voltage Transducer, "LV 25-600/SP2 (Series: LV 25-Voltage)." Datasheet available at: www.lem.com.

[138] Analog Devices, "AD9222 8x 40 MSPS 12 bit pipeline AD-Converter." Datasheet available at: www.analog.com.

[139] S. Gjerde, P. Olsen, K. Ljokelsoy, and T. Undeland, "Control and Fault Handling in a Modular Series Connected Converter for a Transformerless 100 kV Low Weight Offshore Wind Turbine," *Industry Applications, IEEE Transactions on*, vol. PP, no. 99, pp. 1–1, 2013.

[140] O. Mo, M. Hernes, and K. Ljokelsoy, "Active damping of oscillations in LC-filter for line connected, current controlled, PWM voltage source converters," in *EPE 2003, Barcelona:*, 2003.

[141] T. Haileselassie, *Control, Dynamics and Operation of Multi-terminal VSC-HVDC Transmission Systems*. PhD thesis, Norwegian University of Science and Technology, NTNU, 2012.

[142] G. Ramtharan, A. Arulampalam, J. Ekanayake, F. Hughes, and N. Jenkins, "Fault ride through of fully rated converter wind turbines with AC and DC

transmission," *Renewable Power Generation, IET*, vol. 3, pp. 426 –438, Dec. 2009.

A SI- and Per Unit Definitions

A.1 Base values

All AC quantities are defined with reference to the nominal power of one module, i.e. one per unit is the output of one module. The apparent power is defined for the entire system.

Base value, AC-side voltage (U_n is the nominal line-line voltage):

$$U_{base} = \frac{\sqrt{2}}{\sqrt{3}} U_n \tag{A.1}$$

Base value, AC-side current (I_n is the nominal current):

$$I_{base} = \sqrt{2} I_n \tag{A.2}$$

Base value, impedance:

$$Z_{ac,base} = \frac{U_{base}}{I_{base}} = \frac{U_n}{\sqrt{3} I_n} \tag{A.3}$$

Base value, DC-side voltage:

$$U_{dc,base} = 2U_{base} = \frac{2\sqrt{2}}{\sqrt{3}} U_n \tag{A.4}$$

Base value, DC current:

$$I_{dc,base} = \frac{3 I_{n,base}}{4} \tag{A.5}$$

Base power:

$$S_{base} = S_{dc,base} = N S_{base,3phase} = N \frac{3}{2} U_{base} I_{base} \tag{A.6}$$

Base value, DC-capacitor time constant (from [141]):

$$C_{dc,base} = \frac{2 \cdot P_{dc,base} \cdot 1s}{U_{dc,base}^2} \tag{A.7}$$

A.2 Per unit values

Per unit values are defined as:

$$x_{pu} = \frac{X_{real}}{X_{base}} \tag{A.8}$$

A.3 SI-equations for theoretical developments

The following equations are basic equations expressed in SI. These are the bases for the analyses in Chapter 3, which are presented entirely in per unit.

Diode bridge DC-bus voltage for normal 120° conduction mode, Eq. A.9:

$$U_{dc,i} = \frac{3}{\pi}\left(\sqrt{2}U_{ll,rms} - \omega_e L_s I_{dc,link}\right) \tag{A.9}$$

Six-step operation of VSC, heavy loaded diode bridge, Eq. A.10:

$$U_{dc,i} = \frac{\pi}{\sqrt{6}}U_{ll,rms} \tag{A.10}$$

No-load operation of diode bridge, Eq. A.11:

$$U_{dc,i} = \sqrt{2} \cdot U_{ll,rms} \tag{A.11}$$

DC-link current with one converter unit tripped, Eq. A.12

$$\begin{gathered} I_{dc,link} = \frac{P_{dc,h}}{U_{dc,h}} = \frac{P_{dc,h}}{U_{dc,tot} - U_{dc,f}}(N-1), \\ U_{dc,tot} = NU_{dc,n} = 100\,kV \end{gathered} \tag{A.12}$$

B Control Tuning Details

B.1 Current control tuning

The vector current control system design for a converter unit control starts from the dynamic equation describing a generator segment in the dq-plane:

$$\begin{aligned} u_{d,i} &= -(r_s i_{d,i} + l_s \cdot \frac{di_{d,i}}{dt}) + n_{mech} x_s i_{q,i} \\ u_{q,i} &= -(r_s i_{q,i} + l_s \cdot \frac{di_{q,i}}{dt}) - n_{mech}(x_s i_{d,i} - \psi_i) \end{aligned} \tag{B.1}$$

The subscript i is omitted in the following. The s-domain representation of Eq. 4.1 is (given by Eq. B.2):

$$\begin{aligned} u_d(s) &= -(r_s + s l_s) i_d, + n_{mech} x_s i_q \\ u_q(s) &= -(r_s + s l_s) i_q - n_{mech}(x_s i_d - \psi) \end{aligned} \tag{B.2}$$

According to [79], a PWM-controlled power electronic converter can be approximated as a pure time delay for each axis:

$$H_{pwm}(s) = \frac{1}{sT_{cm} + 1} \tag{B.3}$$

The time constant T_{cm} is defined as $T_{pwm}/2$. A PI controller is introduced for each of the two axis currents, and assuming perfect elimination of the cross coupling terms, the open loop current response for one axis (here given by the q-axis) is (Eq. B.4):

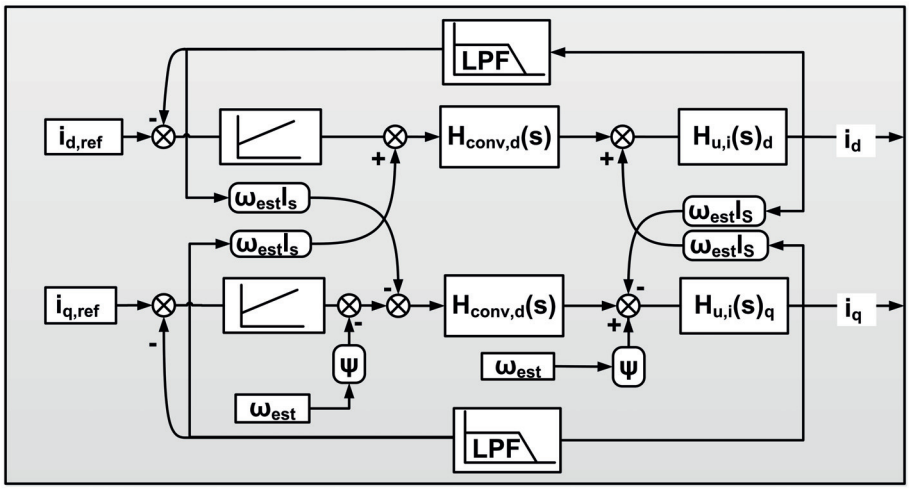

Figure B.1: DQ-current control loop with the stator armature reaction ($H_{u,i}(s)$) and the transfer function of the PWM-controlled converter ($H_{conv}(s)$).

$$i_q = \frac{1}{(1 + l_s/r_s s)} \frac{1}{(1 + sT_{cm})} \frac{1}{(1 + sT_{filt})} K_p \frac{(1 + T_i s)}{T_i s} \cdot i_{q,ref} \tag{B.4}$$

The current-control loop block diagram is given in Fig. B.1.

The modulus optimum criterion [79] is applied for tuning of the PI control parameters: The time constant of the integrator, T_i, is selected equal to the electric time constant of the stator segment for pole cancellation. The proportional gain is chosen according to Eq. B.5

$$K_p = K_{cm} \cdot l_s / T_{pe} \tag{B.5}$$

In Eq. B.5, l_s is the synchronous inductance in per unit, and T_{pe} is the sum of the time delays in the control loop, K_{cm} is voltage gain for the converter unit.

Re-arranging and simplifying Eq. B.4 yields Eq. B.6.

$$i_q = \frac{K_p}{(sT_{pe} + 1) \cdot T_i s} \cdot i_{q,ref} \tag{B.6}$$

Finally, the feedback is introduced, and the closed loop transfer function is obtained:

$$\frac{i_q}{i_{q,ref}} = \frac{K_p / r_s}{s^2 (T_i T_{pe}) + s T_i + K_p / r_s} \tag{B.7}$$

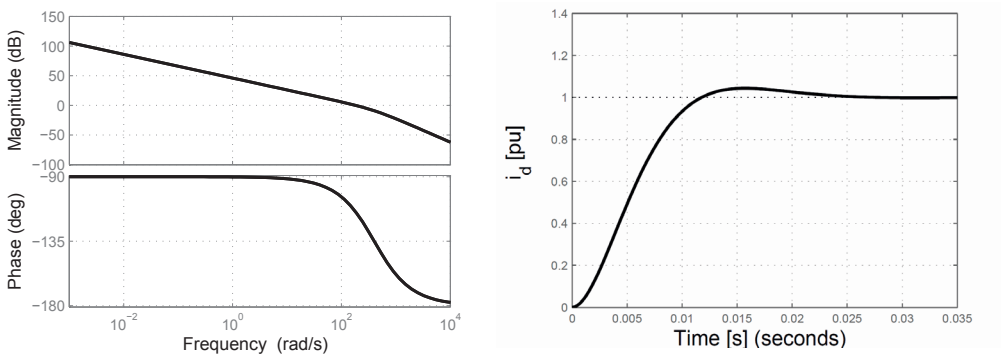

(a) (b)

Figure B.2: a) Open loop frequency response for the current control b) Step response for the current control, calculated from the transfer function

Table B.1: Parameters for tuning of the control system

Parameter	*Value*
x_s	0.33 pu
r_s	0.02 pu
f_{sw}	1 kHz
T_{filt}	2 ms
K_p	0.335 pu
T_i	89 ms

The parameters in Table B.1 are used as basis for the tuning. The current filter time constant is chosen to give damping factor of 10 at the switching frequency of the converter. In Fig. B.2(a), the open-loop bode plot of the current control is presented. The phase margin is approximately 60°. The ideal, theoretical step response of the D-axis current control is presented in Fig. B.2(b). The d-axis is chosen as reference, since this is not related to the torque of the machine, and hence also suitable for response test in the experimental work.

B.2 Flux weakening control tuning

The flux weakening control block transfer function for tuning is developed in [113]. A brief summary is presented here, together with the choice of parameters.

The transfer function from the d-axis current $i_{d,ref}$ to the corresponding depth of modulation, $u_{cmd,d}(s)$, is given by Eq. B.8:

$$G_v(s) = \frac{u_{cmd,d}}{i_{d,ref}} = \frac{K_m \cdot (1 + \frac{s}{T_n})}{1 + \frac{s}{\omega_c}} \tag{B.8}$$

Where T_n is the stator electric time constant,ω_c the closed loop current control cross over frequency, K_m a gain, defined in the next paragraph.

Linearizing $u_{cmd,d}$ around the midpoint results in Eq. B.9.

$$|u_{cmd,d0}| = |u_{cmd,q0}| = \frac{u_{cmd,n}}{\sqrt{2}} \tag{B.9}$$

The open loop transfer function from $i_{q,ref}$ to $i_{d,ref}$, G_{fwO} is expressed as:

$$G_{fwO}(s) = K_0 K_m K_{i,fw} \cdot \frac{1 + sT_n}{1 + \frac{s}{\omega_c}} \cdot \frac{1 + \frac{s}{K_{i,fw}/K_{p,fw}}}{s} \tag{B.10}$$

$K_{i,fw}$ is flux weakening control integral gain, and $K_{p,fw}$ is flux weakening proportional gain. The constant gains of Eq. B.10 are defined as follows:

- $K_0 = |u_{cmd,d0}|$
- $K_m = r_s$
- $K_{i,fw}/K_{p,fw} = \omega_c$
- $K_{fw} = K_0\ K_m\ K_{i,fw}$

Where $K_{i,fw}$ is used to tune the frequency response of the control.

The open loop transfer function can be simplified to Eq. B.11, (including a low pass feedback filter with time constant T_f):

$$G_{fw0} = K_{fw} \cdot \frac{1 + sT_n}{s} \cdot \frac{1}{1 + sT_f} \tag{B.11}$$

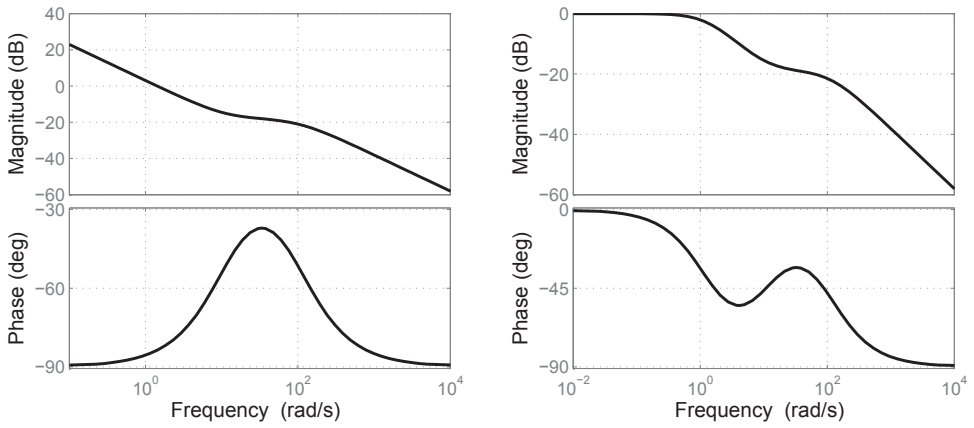

(a) (b)

Figure B.3: Flux weakening control linearized frequency response a) Open loop b) Closed loop

The open loop control and closed loop control frequency responses are presented in Fig. B.3(a) and Fig. B.3(a) respectively. The control parameters are given in Table B.2.

Table B.2: Flux weakening control parameters

Parameter	*Value*
K_p	0.53 pu
T_i	5.3 ms

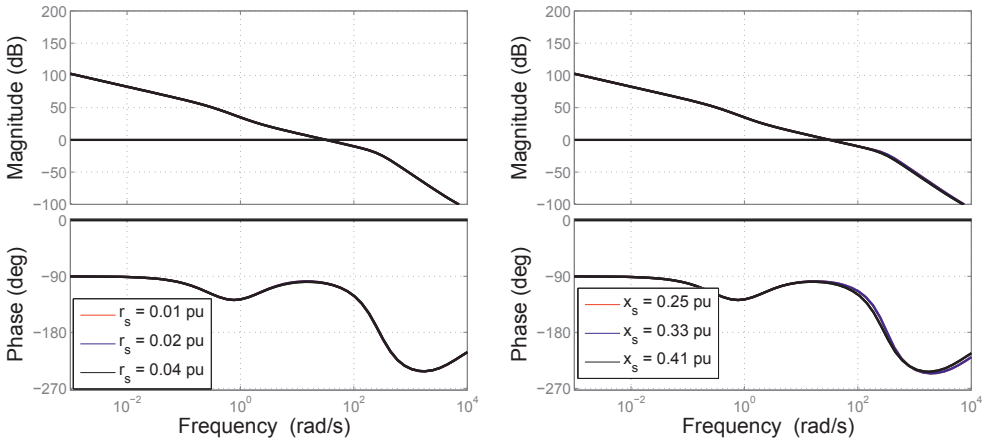

(a) (b)

Figure B.4: Frequency response of open loop control for different stator parameters at n_{mech}=0.3 a) Stator resistance. b) Stator reactance.

B.3 DC-voltage control - additional robustness analysis

The impact of stator resistance- and reactance variations on the DC-voltage control stability margins is analyzed based on the frequency response of the control loop. The results are presented in the following.

Stator resistance: There is, according to the frequency response, no measurable impact on the DC-bus voltage control stability margins within a large variation of the stator resistance, r_s, Fig. B.4(a).

Stator reactance: The frequency response as a function of varying stator reactance is given in Fig. B.4(b). From the results, it can be concluded that within reasonable variations, the effect on the stability margins is negligible.

B.4 Tuning of the maximum power point tracker

The tuning of the ISC-MPPT is conducted according to [116]. The optimal torque is obtained by selecting the gain, k_{opt}, as defined by Eq. B.12.

$$k_{opt} = \frac{1}{2}\rho\pi R^3 \frac{R^2 C_{p,max}}{\lambda_{opt}^3} = 0.159 \tag{B.12}$$

The C_p-curve for the PSCAD-wind turbine model can be described by Eq. B.13 according to [126].

$$C_p = 0.5 \cdot (TSR - 5.6 - \frac{\beta^2}{45}) \cdot e^{-TSR/6} \tag{B.13}$$

The tip speed ration,TSR, is defined as $\frac{2.237 V_w}{\Omega_{mech}}$

β is the blade pitch angle in degrees, V_w is the wind speed and Ω_{mech} the turbine mechanical speed. The turbine parameters are defined in Table B.3.

Table B.3: Wind turbine model data

Parameter	*Value*
P_{rated}	10 MW
R_{blade}	75.05 m
Rotor swept area	17639 m^2
$C_{p,max}$	0.434
λ_{opt}	14.47
ω_{opt}	2.507 [rad/s]

The maximum power point tracker is demonstrated by simulation results, using an average model, and balanced modules. The results are compared to the theoretical results obtained by calculating the power as function of wind speed for the PSCAD-turbine model, Fig. B.5.

The simulations are for a series spanning from $V_{wind} \in$ [5 m/s 7 m/s 9 m/s 11 m/s 13 m/s].

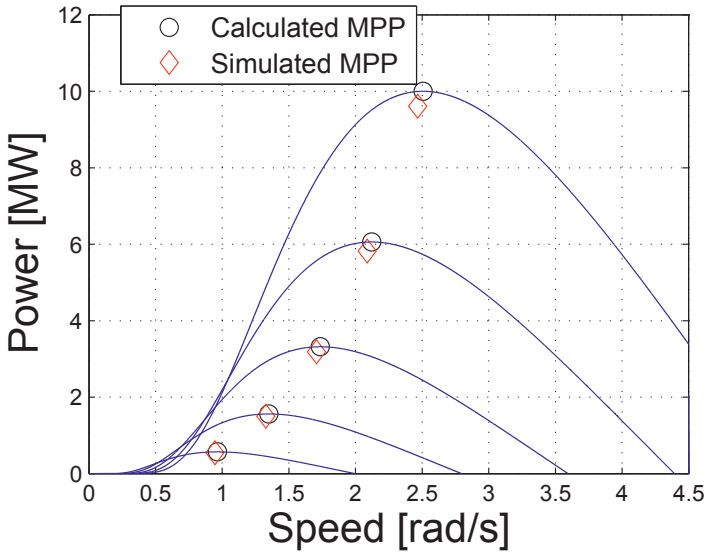

Figure B.5: Power curves for the turbine model, with theoretical MPP highlighted.

C Theory Background

C.1 Droop control functionality transient analysis

By rearranging Eq. 4.27, the droop term can be expressed by Eq. C.1:

$$k_\delta \cdot \left(\sum_{i=1}^{N} i_{q,bal,i} \right) = u_{dc,ref0} - u_{dc,ref} \tag{C.1}$$

The DC-bus voltage control output, $i_{q,bal,i}$, is given by:

$$\begin{aligned} i_{q,bal,i} &= H_{pi,dc}(s) \cdot (u_{dc,ref} - u_{dc,i}) \\ \Rightarrow k_\delta &\cdot \left(\sum_{i=1}^{N} H_{pi,dc}(s) \cdot (u_{dc,ref} - u_{dc,i}) \right) = u_{dc,ref0} - u_{dc,ref} \end{aligned} \tag{C.2}$$

The transfer function of the PI controller is $H_{pi,dc}(s)$, Eq. C.3:

$$H_{pi,dc}(s) = \frac{K_p(1 + sT_i)}{sT_i} \tag{C.3}$$

Introducing equal voltage references for all modules and isolating the droop constant on the left-hand side allows for rewriting Eq. C.2 into Eq. C.4:

$$\begin{aligned} N k_\delta H_{pi,dc}(s) u_{dc,ref} = \\ k_\delta H_{pi,dc}(s) \sum_{i=1}^{N} u_{dc,i} + \left(\frac{1}{N(1 + sT_{filt,0})} \sum_{i=1}^{N} u_{dc,i} \right) - u_{dc,ref} \end{aligned} \tag{C.4}$$

Where Eq. C.5 is introduced for the reference.

$$u_{dc,ref0} = \frac{1}{N}\frac{1}{(1+sT_{filt,0})}\sum_{i=1}^{N} u_{dc,i} \tag{C.5}$$

Finally, re-arranging Eq. C.4 results in Eq. C.6:

$$\begin{aligned} u_{dc,ref} &= \frac{1}{N}\cdot\frac{(sT_i)+NK_\delta K_p(1+sT_i)(1+sT_{filt,0})}{(sT_i)+NK_\delta K_p(1+sT_i)}\sum_{i=1}^{N} u_{dc,i} \\ &= \frac{1}{N}H_\delta(s)\sum_{i=1}^{N} u_{dc,i} \end{aligned} \tag{C.6}$$

The steady-state value of $u_{dc,ref}$ is obtained by evaluating Eq. C.6 for s→0:

$$\lim_{s\to 0} u_{dc,ref} \Rightarrow \frac{1}{N}H_\delta(s)\sum_{i=1}^{N} u_{dc,i} = \frac{1}{N}\sum_{i=1}^{N} u_{dc,i} \tag{C.7}$$

The torque-based DC-voltage droop results in the voltage reference approaching the set point voltage in steady state. According to Eq. 4.27, $u_{dc,ref}$ can only equal $u_{dc,ref0}$ if the sum of current contributions is zero (or k_δ=0). It can therefore be concluded that the droop control presented here will lead to a zero net contribution from the DC-bus control to the torque control in steady state.

C.2 Short circuit of stator-segment coil

The short circuit (partial or complete) of a stator coil requires special attention in the series connected converter. Fault mitigation through flux weakening schemes has been proposed for VSC controlled machines [98, 99]. The method is based on reducing the torque-current i_q to zero, and feed in $i_{d,ref}$ to fulfil Eq. C.8.

$$i_d = \frac{\psi}{x_s} \tag{C.8}$$

If the right term of Eq. C.8 is less than $i_{s,n}$, flux weakening would result in a parallel connected modular system being able to continue operation at partial load. However, in the series connected case, each module is required to transfer power to the DC-link to support the DC voltage. With $i_{qf} = 0$ the power output of a module is:

$$\begin{aligned} p_{ac,f} &= u_{q,f} i_{q,f} \\ \Rightarrow p_{ac,i} &\simeq 0 \\ \Rightarrow u_{dc,i} = \frac{p_{dc,f}}{i_{dc,link}} &\simeq \frac{p_{ac,f}}{i_{dc,link}} \end{aligned} \tag{C.9}$$

The only condition which can fulfil Eq. C.9 is $u_{dc,i} = 0$, which is not possible due to the freewheeling diodes of the VSC. A short circuit in a stator coil will therefore result in a shut down of the entire turbine.

D Simulation Background

D.1 Converter unit simulation model

Each of the converter unit simulation models are implemented by using switches to model the IGBTs and diodes. The PSCAD-switches are close to ideal, but for numerical stability, the on-state resistance is given a value in the range of 1 mΩ. In off-state, the switches are modeled by a very large resistance, in the range of MΩ.

An issue that was discovered in PSCAD is simulation of a generator with stator segments on a floating voltage potential. In the place of true, open circuit, a large resistance is inserted between the machine model neutral point and ground to emulate isolated star-connection. This improves normally the numerical stability of the simulations. However, this resistance results in small currents flowing from the high voltage DC-link side, via the converter, machine and neutral resistance to ground. This small current will, in the case of machine modules floating on different potentials, causes a numerical instability, and the consequence is that the capacitor voltages on the DC side are drifting, at what should be zero current.

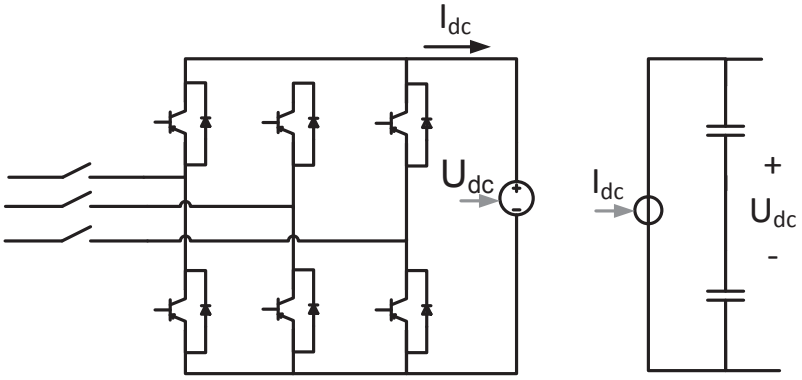

Figure D.1: Converter model split into low voltage and high voltage sides

To eliminate this issue, the converter unit model is split in a low voltage side and high voltage side as shown in Fig. D.1. The current is measured on the switch side of the bus capacitor, I_{dc}, and used as input to the controlled current source on the high voltage side. Equally, the DC-bus voltage, U_{dc} is measured across the bus capacitor, and input to the controlled voltage source on the low voltage side. This splitting in low/high voltage eliminates the drift in the voltages, and does not affect the simulations in this thesis. However, a brief test indicated that there may be problems for DC-short circuit simulations. Since this is not included in the thesis, the issue was not pursued further.

D.2 Additional simulation parameters

Simulation input for realistic wind data, Tab, D.1.

Table D.1: Simulation parameters for emulation of realistic wind speed

Parameter	*Value*
Gust Peak Velocity	8 m/s
Gust Period	0.5 s
Ramp Max. Velocity	1 m/s
Ramp Period	1 s
Number of Noise Comp.	50
Noise Amplitude Param.	1 rad/s
Surface Drag Coefficient	0.0192
Turbulence Scale	600 m

Simulation model DC-link R/L-parameters, Table D.2:

Table D.2: Cable parameters

Parameter	*Value*
Cable cross section, A	100 mm^2
Cable resistivity, ρ	$1.68{\cdot}10^{-8}$
Cable Length	20 km
Inductance per km, R_t	0.168 Ω/km
Inductance per km, L_t	0.577 mH/km

E Background Results for Transient Analysis

E.1 Step response of current control

The synthesis of the current control is based on the assumption that the response in each module current control is equal to that of a standard, 3-phase system. This assumption is valid if the response of the current controls in converter series connection (Fig. E.1(b)) is comparable to that of single-module system (Fig. E.1(a)). By comparing the results in the two figures, it can be concluded that the responses of the controllers for the three series connected modules are exact the same as for the standard 3-phase system. Consequently, the response of one converter unit do not have an effect on the other converter units in the chain. Hence, the assumption of equal response is valid for the series connected converter units.

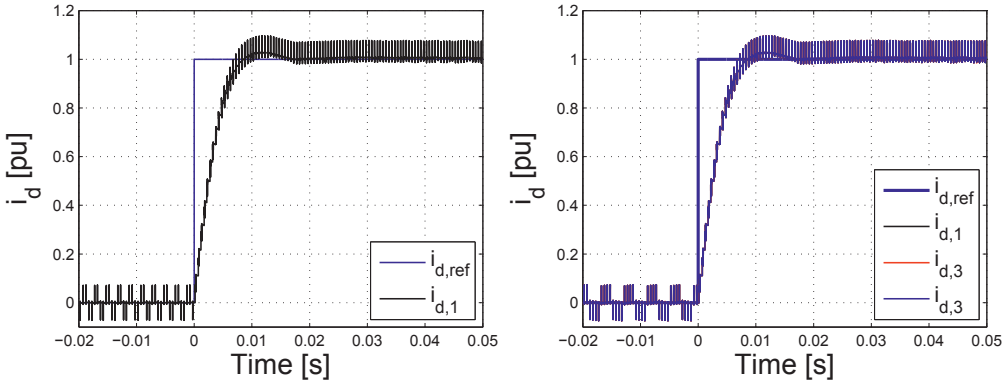

(a) (b)

Figure E.1: a) Unit step response in the d-axis current with the generator at standstill for single module and b) Modular converter with 3 converters .

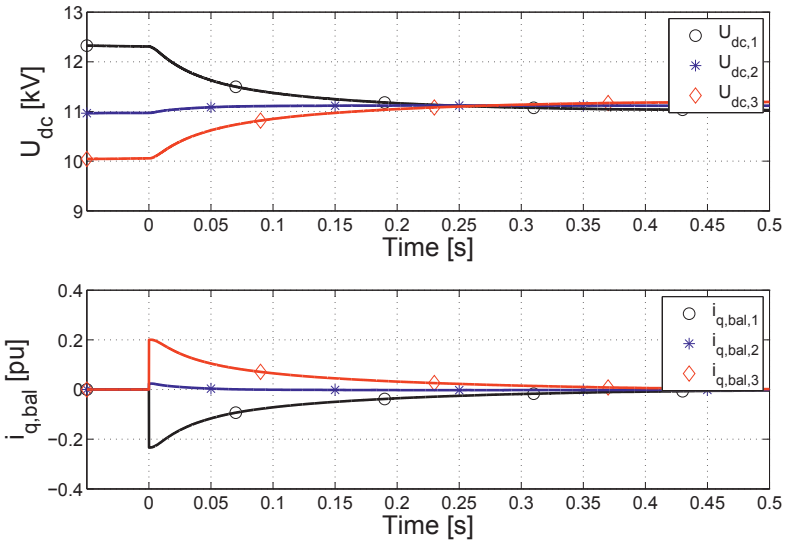

Figure E.2: DC-bus voltage control step response, at n_{mech}=0.3 pu and $m_{em,ref}$=0.0 pu. Time to achieve balance (less than 1 %) deviation is 200 ms. Upper figure: DC-bus voltage. Lower: Bus voltage controller output.

E.2 DC-bus voltage control transient response with deviating stator segment flux linkage

The DC-bus voltage control system robustness against variations in bus capacitances is analyzed based by the simulation results presented in Fig. E.2. The bus capacitances of the three modules are set to different values (C_1=80 %, C_2=100 % C_3=120 %), which creates an initial DC-bus voltage imbalance. Then, the DC-bus voltage-control system is activated at t=0.0 s. The difference between the measured DC-bus voltages and the reference creates a step response. The operating point is n_{mech} =0.3 pu and $m_{em,ref}$=0.0 pu. Before the control is activated, the losses in the switches of the converter units have removed some of the imbalance. At t=0.2 s, the imbalance is practically eliminated, with approximately 1 % deviation remaining. Due to the different time constants of the DC buses (different capacitors), there is a minor overshoot in the response. This is insignificant, approximately 0.5 %, and as can be seen from the DC-voltage controller output, it does not cause an oscillatory response. Hence, the control system performs satisfactory with respect to overshoot and different converter unit DC-bus time constants.

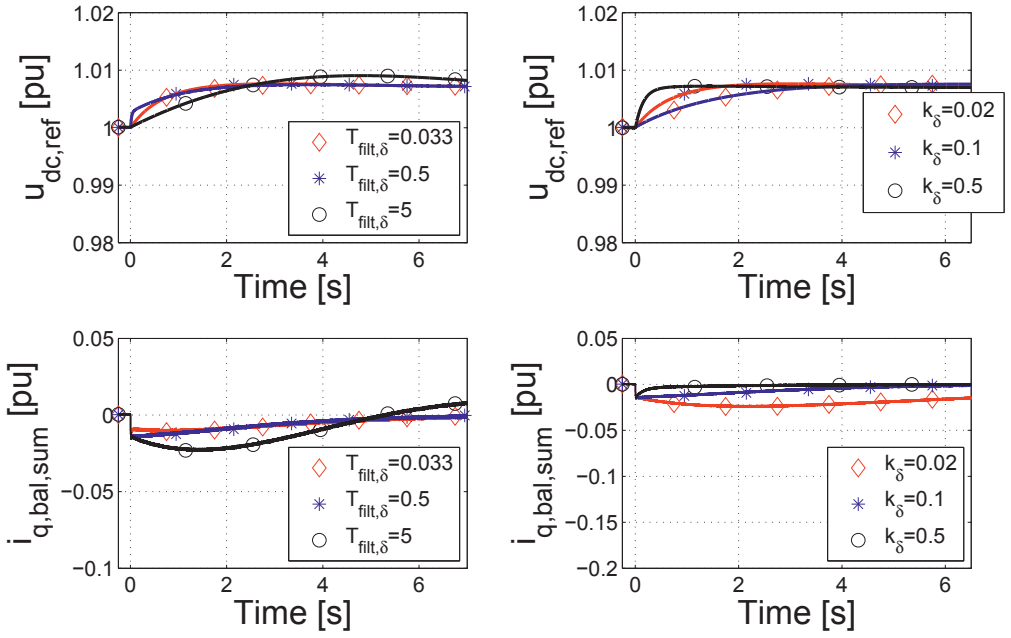

(a) (b)

Figure E.3: Droop control response. n_{mech}=0.9. a) Different filter constants and k_δ=0.1. b) Different gains and $T_{filt,\delta}$ = 0.5 s. (Top to bottom: DC-voltage reference response. DC-voltage control output sum).

E.3 Evaluation of transient response of different droop control parameters

In Sec. 4.3.3, the effect of different parameters in the droop feedback (filter time constant and droop gain) are analyzed by investigating the frequency response of the control loop. In this paragraph, the droop control parameter's impact on the dynamic response is analyzed based on the simulation results presented in Fig. E.3(a) (filter) and Fig, E.3(b) (droop gain). At t=0 s, a step is introduced to $m_{em,ref}$, from 0 pu to 0.75 pu. Consequently, the DC-link voltage is increased quickly, resulting in a response in the DC-voltage average reference.

The impact of three different filter time constants is shown in Fig. E.3(a). For the 5 s filter time constant, the response in $i_{q,bal,sum}$ and DC-voltage reference is overshooting, which is predicted based on the frequency response analysis, Sec. 4.3.3. For the medium- and short-time constants, the response is quick and without overshoot.

In Fig. E.3(b), the simulation results for different droop gains are shown. The

impact of variations in droop gains are in accordance with the frequency response analysis in Sec. 4.3.3: A large gain results in a fast recovery, to zero net torque contribution from the DC-bus voltage control system. A small droop gain gives almost no droop effect at all.

E.4 Open cable faults evaluation

If the case of a complete, sudden loss of grid, the excess energy captured by the turbine will have to be absorbed locally. In the basic converter configuration for the series connected converter, there are mainly two possibilities for absorbing energy: 1) The rotational mass of the turbine. 2) The capacitive energy storages of the converter units. Neither of these will accept large energy quantities: Decreasing the torque and allow the rotor to spin up will result in high mechanical stresses on the structure. The power capture of the turbine will decrease as the speed increases, since the turbine exits the maximum power point. However, this reduction is not sufficient for protecting the turbine. Constraining the turbine speed through torque control will quickly result in overvoltages on the bus-capacitors. Consequently, additional protection measures are necessary.

A DC-bus chopper circuit is the most common overvoltage protection for a VSC. In the series connected converter, the chopper can be either a single, high voltage unit, or one chopper in each module. The advantage of the single chopper is the minimization of component count. The modular version offers a continuation of the modular system design approach, and improved individual module-protection. The two options are compared in the following, with control-based protection as reference case.

- Case 1: Limit through torque control [142] and DC-bus voltage control system.
- Case 2: Central chopper.
- Case 3: Chopper in each module.

All cases have a voltage limit set to 1.1 pu. An emergency pitch action, providing a pitching of 6°/s is activated after the DC voltage reaches the maximum level.

The simulation results are presented in Fig. E.4 and Fig. E.5, and key numerical values in Table E.1.

As expected, the reference case does not limit the system in a satisfactory manner. The turbine speed increases to 20 % above rated and the DC voltage increases to 15 %, for an overvoltage limit of 10 %. The torque oscillations are due to the interaction between the DC-bus voltage control system and the torque limiter.

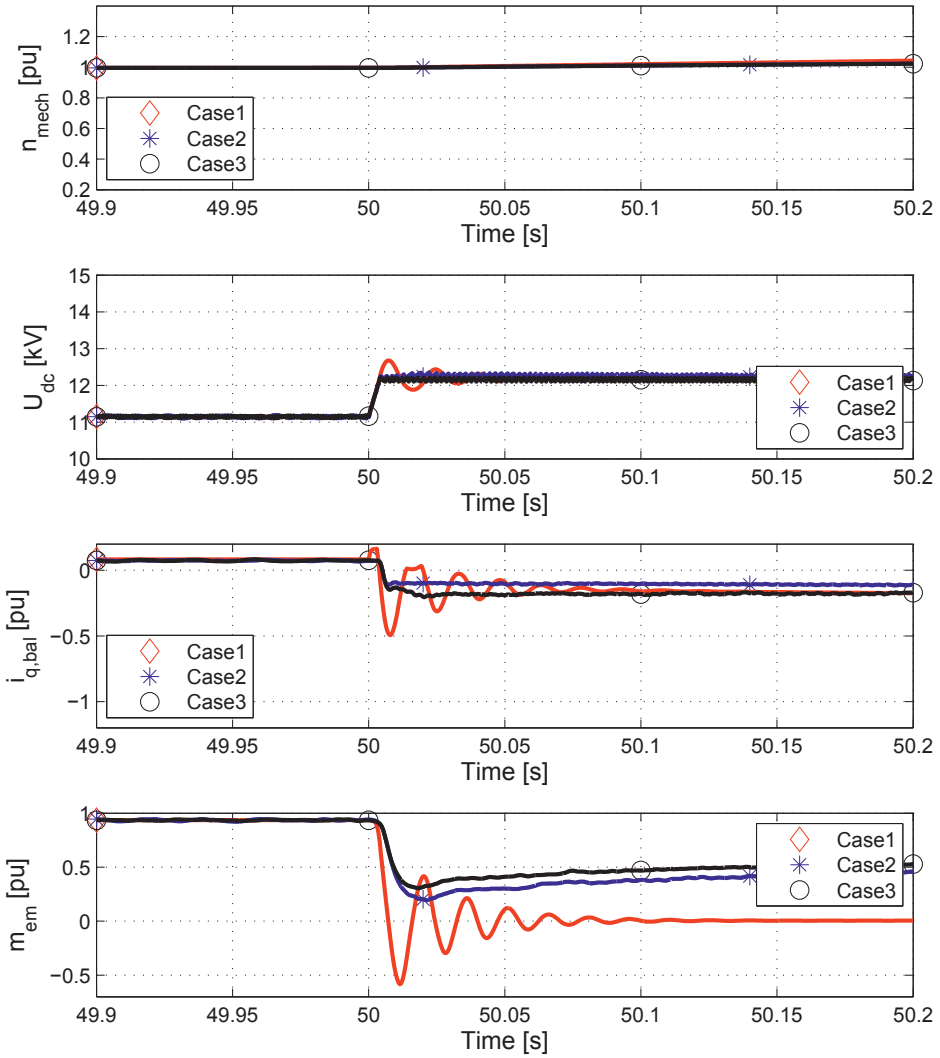

Figure E.4: Response to a sudden loss of grid for different protection strategies. From top to bottom: Turbine speed. DC-bus voltage. DC-bus voltage control output. Stator segment electromagnetic torque.

Both cases with chopper circuits are capable of limiting the voltage according to the defined limit and the turbine speed is restricted to less than 10 % overspeed.

The energy dissipation difference is significant when comparing case 2 and 3, Table E.1. With modular choppers, the required energy cpacaity is 12.2 % more than for the single chopper. The reason is that the DC-bus voltages are maintained at the same level, while in the central chopper, the module bus voltages are allowed to vary slightly. The energy dissipation on module level is listed in Table E.2.

Table E.1: Dissipated energy in the different cases

System config.	*Energy dissipated*	*Max overspeed*	*Max voltage*
Case 1	-	20 %	12.8 kV
Case 2	5.49 MJ	7 %	12.36 kV
Case 3	6.16 MJ	6 %	12.23 kV

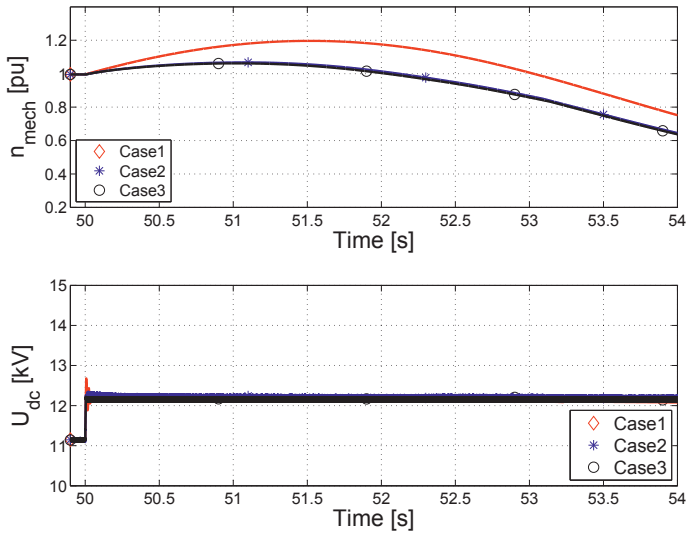

Figure E.5: Loss of grid. Top to bottom: Turbine speed. DC-bus voltages, Output from DC-bus voltage controllers, Electromagnetic torque.

If the design should be based on the maximum module energy dissipation demand, it would be 7.32 MJ in case 3, which require an overrating of 33 %.

The simulation results presented in Fig. E.5 are used to calculate energy dissipation in the chopper circuits, and maximum turbine speed after a loss of grid.

Table E.2: Energy dissipation per module

Module 1	*Module 2*	*Module 3*
2.44 MJ	1.86 MJ	1.86 MJ

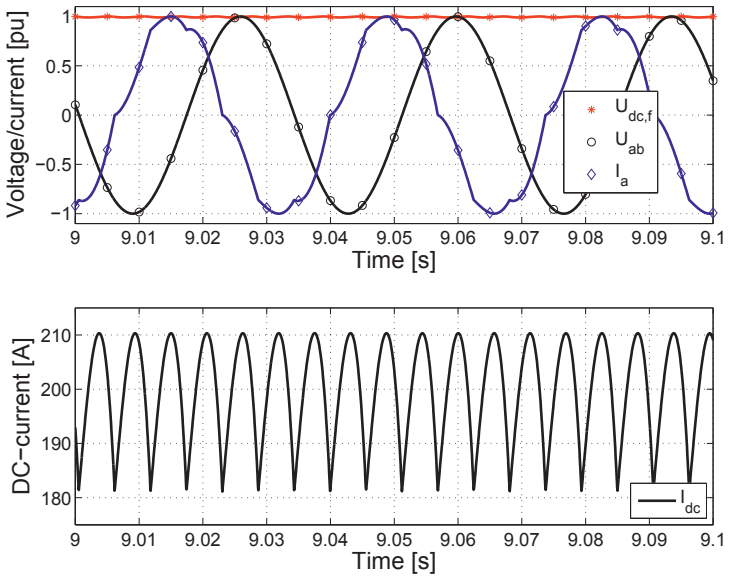

Figure E.6: The current wave forms and corresponding voltages for borderline continuous conduction mode of the diode rectifier.

E.5 Continuous conduction mode of tripped converter unit

The following simulation results demonstrates the limit between 120° conduction mode and continuous conduction mode for one of the modules, Fig. E.6.

E.6 Simulation results illustrating the limit for bypass and redundant operation

The absolute demand for the continued operation due to a converter unit trip is $i_{dc,link} \geq 0$ (transition from generator to motor mode). If the DC current has opposite direction (system in motor mode), the capacitor of the tripped module will be charged instead of discharged. Motor mode introduces therefore a serious threat to the components in the case of a module trip. The issue is illustrated by the simulation results in Fig. E.7: An unprotected system will experience overvoltage in the tripped converter unit. Hence, protection measures for each converter unit are required.

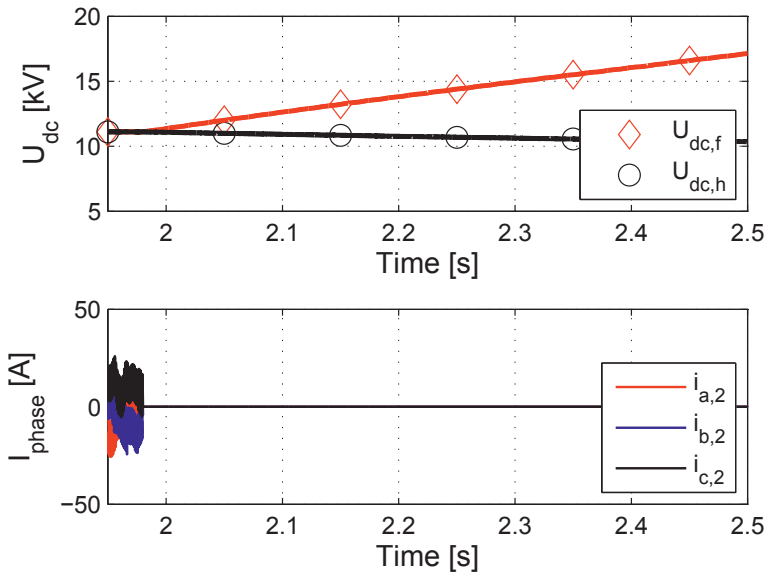

Figure E.7: Converter unit (2) trip, in motor mode. Upper: DC-bus voltages for module 1 and 2. Lower: Stator currents in segment 2.

E.7 Feasibility and requirements for black start of the turbine

Black start capability in the turbine is normally considered necessary for the system operation. The main benefits of black start are:

1. Possibility to use the turbines to charge the DC-link cables in the rare case of a completely black grid.
2. Make a soft connection of the turbine to the grid feasible without application of large, auxiliary circuitry for damping of inrush currents.

The second point is demonstrated in this section. The sequence of a black start for the modular, series connected converter is:

1. Close AC breakers, turn on the converter units with $i_{q,ref,i} = i_{d,ref,i} = 0$.
2. Activate the DC-bus control, with $u_{dc,ref} = u_{dc,avg}$. The droop control is not activated at this point.
3. Pitch the blade of the turbine slightly into the wind, allowing the turbine to produce a small torque which accelerates the turbine up to n_{mech}=n_{start}
4. Ramp up the DC voltage to the nominal value for all modules.
5. At $u_{dc,tot} = u_{dc,link}$, close the main turbine connector.
6. Activate the droop control to eliminate steady state contribution from the

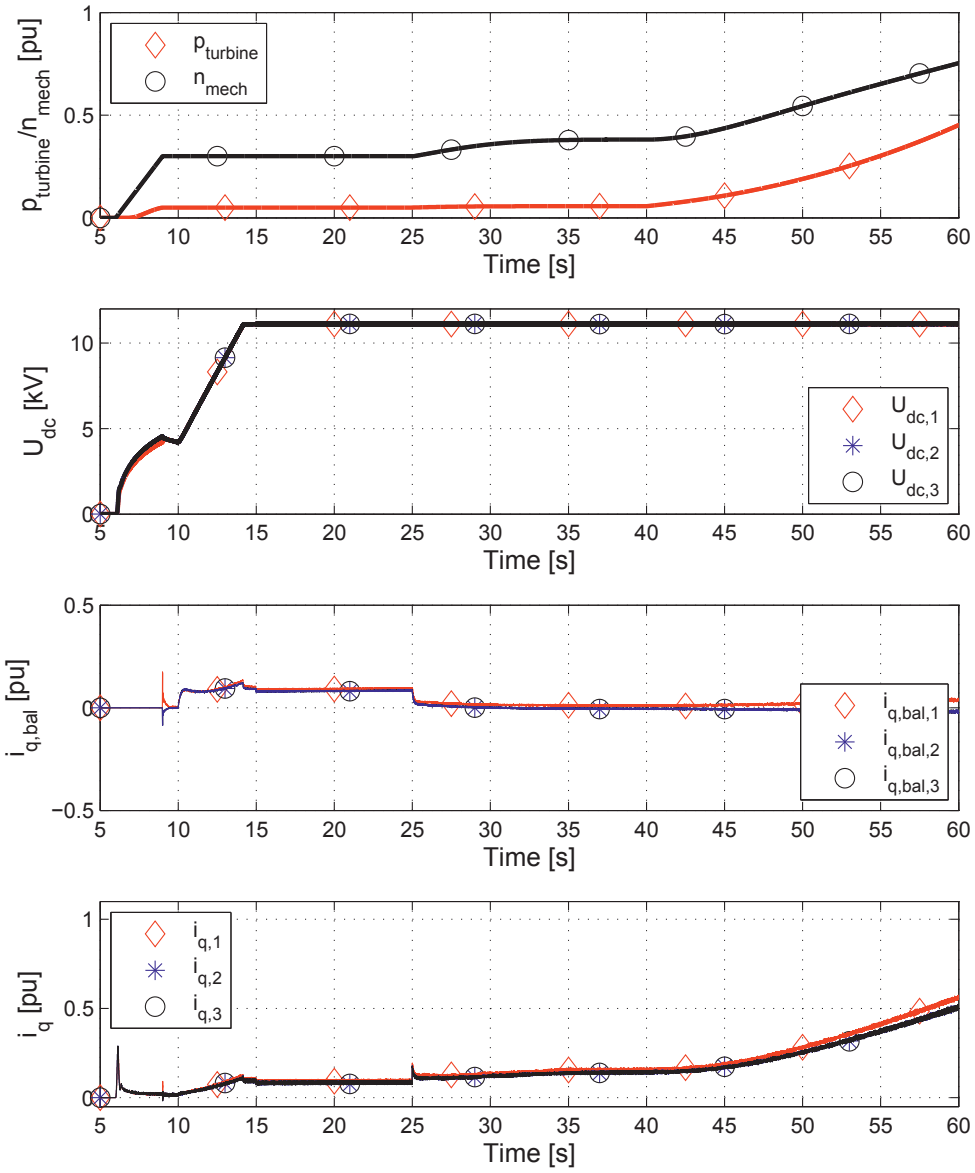

Figure E.8: Black start procedure for the modular, series connected converter tied to an HVDC grid. Top to bottom: Turbine speed and power. DC-bus voltages. DC-bus voltage control output. Stator segment q-axis currents.

DC-voltage controls.

7. Switch to normal operation of pitch control and ISC.

The black start sequence simulation results are given in Fig. E.8. The process is initiated at t=5 seconds, when the current controllers are activated. At t=6 s, the blades are pitched into the wind, and the turbine accelerates. This results in an induced voltage, and hence a current flowing into the DC buses, charging the bus capacitors. Then, at t=9 s, the DC-voltage balance control is activated, with a ramp reference as input, from the present to nominal voltage. This results in a positive charging current contribution from the DC-bus voltage control system. At nominal voltage, the grid connector is closed (t=14.97). The DC-voltage control is switched to normal mode, and the droop control activated. Finally, the turbine control goes from start-up mode to normal mode, and the MPPT-tracking is initiated.

F Additional Documentation of the Laboratory Setup

F.1 Verification of current control

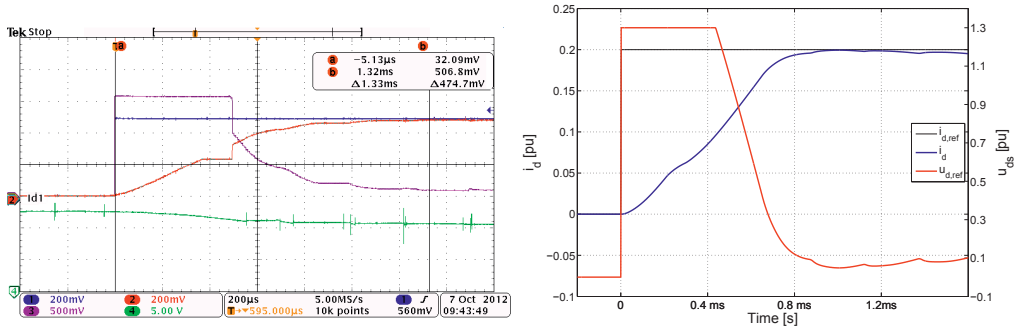

(a) (b)

Figure F.1: Step response of the d-axis current, for converter unit 1. The step is from $i_{d,ref}$ =0.0 to $i_{d,ref}$ =0.2 pu at nominal DC-bus voltage. a) Experimental waveform. (Ch.1: $i_{d,ref}$, Ch.2: i_d, Ch.3: u_{ds}, Ch.4: $u_{dc,1}$). b) Corresponding simulation

The experimental results for the current control step response are obtained by applying a step to the d-axis of module 1, Fig. F.1(a). The current response measurements are first processed through the dq-transform in the FPGA, and then output via the DA-converter to the oscilloscope. A simulation of the same test is presented in Fig. F.1(b). The transient duration of the response is approximately 1.2 ms, which is 9.8 % shorter than obtain experimentally.

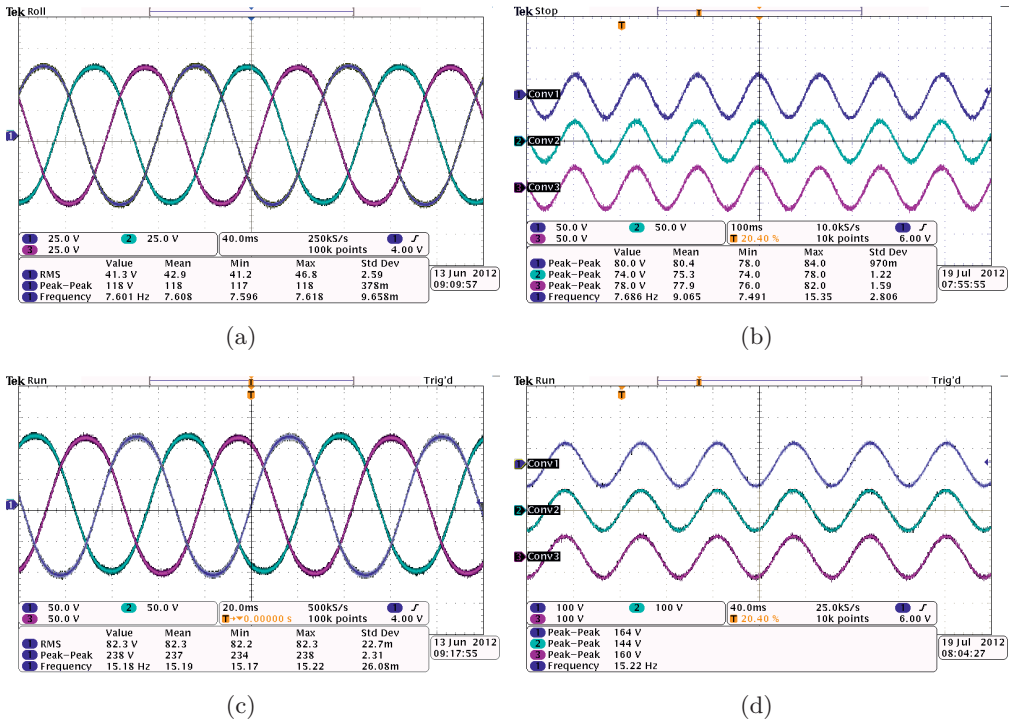

Figure F.2: No load voltages a) Phase voltages, 20 rpm, standard 3-phase winding configuration b) Line voltage, U_{ab} at 20 rpm, 3 stator segments c) Phase voltages, 40 rpm, standard 3-phase winding configuration d) Line voltage, U_{ab} at 40 rpm, 3 stator segments. (Ch.1-3: Generator voltage)

F.2 Comparison of 3-phase and three stator segment voltages in no-load

The no-load test, Fig. F.2(a)-Fig. F.2(d) demonstrates the relation between voltages of the 3-phase- and three-segment configurations[1]. In Fig. F.2(a), the 3-phase winding output is shown for 20 rpm. Fig. F.2(b) shows corresponding results for the segmented generator configuration. The frequency is the same in the two cases, while the voltages are in principle reduced to one third. There is a difference in induced voltages between the stator segments. At 20 rpm, the maximum measured difference is 7.3 %. At 40 rpm, it is 13.9 %. The cause of this is rotor and stator imperfectness.

[1]The 3-phase voltages are measured as phase voltages, and three-segment voltages as line voltages. This was because of practicalities in the measurement arrangement.

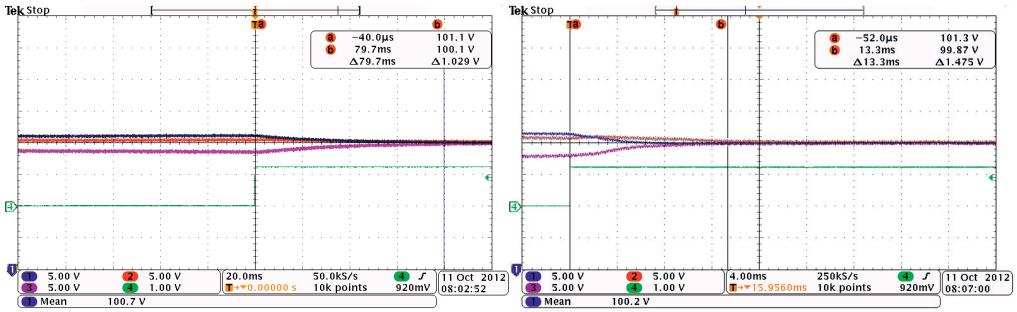

(a) (b)

Figure F.3: DC-bus voltage control response for balanced bus voltages. $m_{em,ref}$=0.01. a) Generator speed of 5 rpm. b) Generator speed of 40 rpm. (Ch.1: $U_{dc,1}$, Ch.2: $U_{dc,2}$), Ch.3: $U_{dc,3}$, Ch.4: Trigger)

.

F.3 DC-bus control turn on response with controlled DC-link voltage

The relation between generator speed and DC-bus voltage response is demonstrated in Sec. 6.2.3 and repeated for a fixed DC voltage in Fig. F.3(a)-F.3(b) (low speed (5 rpm) and high speed (40 rpm) respectively): Both cases are with a torque reference of 0.01 pu. The relation between the two response times should be proportional to the machine speed. There is a deviation in the measured response times. This is ascribed saturation of the current control output and manual estimations of the response time from the oscilloscope measurements which results in low measurement accuracy.

F.4 Definition of load cases

The two variable load profiles which are used throughout the laboratory tests are defined as:

- Case 1: Generator speed of 20 rpm, load staircase according to Fig. F.4(a).
- Case 2: $m_{em,ref} = 0.1$ pu. Speed staircase according to Fig. F.4(b)

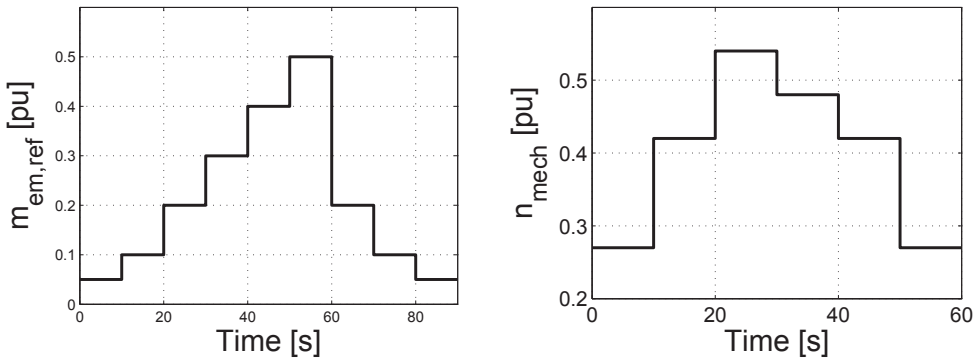

(a) (b)

Figure F.4: Definition of load profiles. a) Case 1: Fixed speed, variable torque. b) Case 2: Fixed torque, variable speed

F.5 Equipment lists

In the following tables, the equipment used for the experimental work are listed.

Table F.1: Digital control system components

Component	*Description*	*Producer*
Xilinx FPGA Virtex 5	Custom made board	Sintef Energy
Platform cable USB II	JTAG	Xilinx
BF-810	USB to serial adapter,	Bafo
LEM LA 205-S	Current transducers for feedback signals	LEM
LEM LV25ps	Voltage feedback sensors	LEM
ActiveDSP v.1.507	Operation, debugging and sampling interface for communication between control card and computer	CrossHair Embedded

Table F.2: Power circuit components

Component	*Rated value*	*Producer*
Three 3-phase VSC converters	20 kW, 400 V DC	NTNU/Sintef (Semikron SKM400GB125D 2x 400A 1200V IGBT)
DC-capacitor bank	3300 μF	RIFA PEH
9 Filter inductances	1.75 mH, I_n 55 A (RMS)	Sintef
Diode bridge	$I_n = 35$ A	NTNU

Table F.3: Manual measurement equipment

Component	*Description*	*Producer*
Fluke 80i-110 s	AC/DC Current probe	Fluke
MSO 3014	Mixed signal (Digital/analogue) oscilloscope	TexTronix
P6139B	Voltage probes	TexTronix
PM6306 Programmable automatic RCL-meter	Measuring machine inductance	Fluke
GOM-802 DC-milli-ohm-meter	Measuring winding resistance of machine and inductances	GW Instek

Table F.4: Generator phase inductance/resistance, 50 Hz

Module number	*Phase A*	*Phase B*	*Phase B*
Segment 1 (master)	343 μH/48 mΩ	337 μH/49 mΩ	339 μH/49 mΩ
Segment 2 (slave 1)	338 μH /51 mΩ	338 μH /51 mΩ	341 μH /51 mΩ
Segment 3 (slave 2)	338 μH /49 mΩ	342 μH /49 mΩ	345 μH /50 mΩ

Nomenclature

K_p	Proportional gain of a controller
k_δ	Droop control proportional constant
K_{cm}	Voltage ratio between input and output of converter.
T_i	Integrator time constant for a PI controller.
T_{pe}	Sum of all estimated time delays in a control loop
x_r	Internal state variable for a PI control
N	Number of modules in the system
$\Delta i_{q,f,udc0}$	Q-axis current reduction from the nominal value at minimum DC-voltage limit in a module
$\Delta i_{q,f}$	Required current reduction for individual module deloading
$i_{c,i}$	DC-capacitor current in module
$i_{d,i}$	Direct axis current of module i
$i_{dc,i}$	DC-current of module i
$i_{dc,link}$	DC-link current
$i_{dq,i}$	DQ-current for module i
i_{max}	Maximum, total module AC current
I_n	Stator segment nominal current
$i_{q,bal,i}$	Balance current, output of the DC-bus voltage control for module i
$i_{q,i}$	Q-axis current in module i
$i_{q,ref,i}$	Q-axis current reference for a module
i_q	Q-axis current

$i_{s,i}$	Total module AC current
$I_{x,i}$	Phase current x (a,b,c) of stator segment i
ω_{est}	Estimated generator speed.
τ_{mech}	Mechanical time constant, in seconds
C_p	Turbine aerodynamic power-coefficient curve, characteristic as function of wind speed, rotor speed and pitch angle
$m_{em,i}$	Electromagnetic torque for stator segment i in per unit
$m_{turbine}$	Turbine mechanical torque
n_{mech}	Turbine speed
η_i	Converter unit efficiency
ψ_i	Stator flux linkage in segment i
θ_i	Rotor position relative to stator segment i
c_i	Bus capacitance
$E_{x,i}$	Induced voltage in stator phase x in modul i
f_n	Generator, nominal electric frequency
f_{sw}	Switching frequency
L	Stator segment self inductance
$M_{xi,yj}$	Mutual inductance between two phases x,y =(a,b,c) and modules i,j
$p_{ac,i}$	AC power in module i
$p_{dc,h}$	Power measured on DC rails of a healthy (full functioning) module
$p_{dc,tot}$	Turbine total output power measured on the converter chain DC side
p_{tot}	Total turbine output power
$r_{s,i}$	Stator segment i winding resistance
x_d	Direct-axis reactance
x_q	Quadrature-axis reactances
$x_{s,i}$	Synchronous reactance in stator segment i
y	Safety factor for overrating of switch blocking voltage
z	Number of redundant modules in the series connection

avg	Subscript avg refers to the average value of a variable
f	Subscript for denoting a variable associated with a fault
i	subscript i is referring to an arbitrary module
n	subscript n refers to nominal values
$\Delta u_{dc,ref,f}$	Reduction in DC-bus voltage reference in a faulty module
$u_{dc,f}$	DC-bus voltage of a faulty module
$u_{dc,i}$	DC-bus voltage in module
$u_{dc,min}$	Lower DC-voltage limit due to freewheeling diodes
$u_{dc,n}$	Nominal DC-bus voltage
$u_{dc,ref,h}$	DC-bus voltage reference for a healthy module
$u_{dc,ref0}$	DC-bus voltage reference based on the average measured module voltages
$u_{dc,ref}$	DC-bus voltage controller reference
$U_{dc,screen,i}$	Common mode voltage between stator segment electric screen and ground
$u_{dq,i}$	dq-voltage for stator segment i
U_{DR}	Peak repetitive voltage rating for power electronic switch
$u_{ll,rms}$	Stator segment i line voltage
U_n	Stator segment nominal voltage
$U_{x,i}$	Phase voltage x (a,b,c) of stator segment i